

APPLICATIONS OF SCANNING PROBE  
MICROSCOPY TO DATA STORAGE  
AND RAMAN SPECTROSCOPY

by

Yanming Zhao

---

Copyright © Yanming Zhao 2004

A Dissertation Submitted to the Faculty of the  
COMMITTEE ON OPTICAL SCIENCES (GRADUATE)

In Partial Fulfillment of the Requirements  
For the Degree of

DOCTOR OF PHILOSOPHY

In the Graduate College

THE UNIVERSITY OF ARIZONA

2004

UMI Number: 3145150

Copyright 2004 by  
Zhao, Yanming

All rights reserved.

### INFORMATION TO USERS

The quality of this reproduction is dependent upon the quality of the copy submitted. Broken or indistinct print, colored or poor quality illustrations and photographs, print bleed-through, substandard margins, and improper alignment can adversely affect reproduction.

In the unlikely event that the author did not send a complete manuscript and there are missing pages, these will be noted. Also, if unauthorized copyright material had to be removed, a note will indicate the deletion.

**UMI**<sup>®</sup>

---

UMI Microform 3145150

Copyright 2004 by ProQuest Information and Learning Company.

All rights reserved. This microform edition is protected against unauthorized copying under Title 17, United States Code.

ProQuest Information and Learning Company  
300 North Zeeb Road  
P.O. Box 1346  
Ann Arbor, MI 48106-1346

The University of Arizona ®  
Graduate College


As members of the Final Examination Committee, we certify that we have read the

dissertation prepared by Yanming Zhao

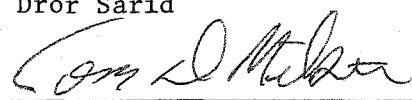
entitled Applications of Scanning Probe Microscopy to Data Storage and  
Raman Spectroscopy

and recommend that it be accepted as fulfilling the dissertation requirement for the

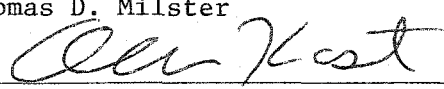
Degree of Doctor of Philosophy

  
\_\_\_\_\_  
Dror Sarid

7-15-04  
\_\_\_\_\_  
date

  
\_\_\_\_\_  
Thomas D. Milster

7/15/04  
\_\_\_\_\_  
date

  
\_\_\_\_\_  
Alan Kost

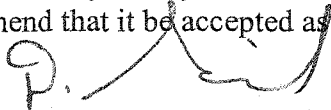
JUL. 15, 04  
\_\_\_\_\_  
date

\_\_\_\_\_  
\_\_\_\_\_  
date

\_\_\_\_\_  
\_\_\_\_\_  
date

Final approval and acceptance of this dissertation is contingent upon the candidate's submission of the final copies of the dissertation to the Graduate College.

I hereby certify that I have read this dissertation prepared under my direction and recommend that it be accepted as fulfilling the dissertation requirement.

  
\_\_\_\_\_  
Dissertation Director: Dror Sarid

7-23-04  
\_\_\_\_\_  
date

## STATEMENT BY THE AUTHOR

This dissertation has been submitted in partial fulfillment of requirements for an advanced degree at The University of Arizona and is deposited in the University Library to be made available to borrowers under rules of the Library.

Brief quotations from this dissertation are allowable without special permission, provided that accurate acknowledgment of source is made. Requests for permission for extended quotation from or reproduction of this manuscript in whole or in part may be granted by the copyright holder.

SIGNED: \_\_\_\_\_

A handwritten signature in cursive script, appearing to read "Sho Fin", written over a horizontal line.

## ACKNOWLEDGEMENTS

Naturally, I would like to acknowledge all those at the Optical Sciences Center, faculty, staff and students who enabled my experiences here to be most enjoyable and rewarding.

A special thanks goes to Professor Dror Sarid with whom I have worked since my arrival in the fall of 1999. For his students, Dror's office has always been open and he has astounded me with his patience and willingness to stop whatever he was doing to take the time to address my needs. Dror also has provided the capital equipment, ideas, valuable advice and direction, encouragement, knowledge, and arranged for all funding of this work. Thanks as well, is due to the agencies that provided the funding, namely, National Aeronautics and Space Administration (NASA), California Institute Of Technology, EMC Corporation, and Digital Instruments (Veeco).

I wish to thank Professor Thomas D. Milster, John J. Butz and Melissa Bailey for their generous aid in solving a variety of optical problems. I wish to thank Professor Alan Kost for valuable discussions about lasers and spectroscopy. I would also like to thank Professor Ghassan E. Jabbour and Konstantin Yamnitskiy for their help in providing highly relevant samples. Furthermore, I wish to recognize Professor M. Bonner Denton and Carolyn Pommier of the Chemistry Department, University of Arizona, and Mark S. Anderson of Jet Propulsion Laboratory, for very helpful discussions relating to the construction of the Raman-Atomic Force Microscope.

More personally, I wish to thank Charles Tony Peterson for his instruction of SPM techniques. I also am very grateful to Dr. Brendan McCarthy for sharing his broad scientific knowledge and expertise with me during the collaboration. The opportunity to work within a small group having diverse research activities has been especially beneficial: I have been able to proceed faster and more effectively by sharing in the problems and progress of several active projects. I wish to recognize Dr. Asa Fein for his collaboration of the data storage project, and Dr. Jianhua Gu for his collaboration of the early part of the Raman project. Ranjan Grover and Glen Jannuzzi provided additional ideas.

Finally I would like to thank my wife Cao Lei, my parents, my parents in law, and the rest of my family for their constant love and selfless generosity during these years.

# TABLE OF CONTENTS

LIST OF FIGURES .....	6
ABSTRACT .....	9
1 SCANNING PROBE MICROSCOPY .....	10
1.1 Scanning Tunneling Microscopy .....	10
1.2 Atomic Force Microscopy .....	13
2 APPLICATIONS OF SPM TO DATA STORAGE .....	18
2.1 Reversible, Nanoscale Transitions in an Organic Complex .....	18
2.2 Injected Current Pulses with Conducting-tip, Tapping-Mode AFM .....	24
2.3 All-metal tapping mode AFM probe .....	33
2.4 Conclusion .....	39
3 APPLICATIONS OF SPM TO RAMAN SPECTROSCOPY .....	40
3.1 A Brief Look at Raman Scattering Spectroscopy .....	42
3.2 Surface Enhanced Raman Scattering .....	49
3.3 Combination of AFM and Raman Scattering .....	62
3.4 Optics of Probing a Local Raman Scattering Signal .....	66
3.5 Raman AFM with Nanoscale Resolution .....	83
3.6 Thermometry using Raman Spectroscopy .....	95
3.7 Conclusion .....	102
APPENDIX .....	103
REFERENCES .....	107

## LIST OF FIGURES

Figure 1-1: A diagram of an STM system.....	11
Figure 1-2: Diagram of an AFM system .....	13
Figure 1-3: Diagram of a tapping mode AFM system.....	15
Figure 2-1: One-nm bits written, read, and erased on an organic complex by STM .....	19
Figure 2-2: Local modification of the organic film by the tip-sample electric field .....	20
Figure 2-3: <i>i-V</i> curve change associated with the local modification of the film.....	22
Figure 2-4: Calculated, scaled AFM probe motion <i>Z</i> and conductance .....	27
Figure 2-5: A typical current pulse train, and the associated AFM probe motion .....	28
Figure 2-6: Two current pulses, bias voltage pulses, and AFM probe motion.....	29
Figure 2-7: The current pulse and the ramped input bias voltage .....	30
Figure 2-8: An <i>i-V</i> curve taken with an individual ramped input voltage pulse .....	31
Figure 2-9: Top view SEM micrograph of a worn metal-coated silicon tip.....	33
Figure 2-10: Side view SEM micrograph of a worn metal-coated silicon tip.....	34
Figure 2-11: Line art diagram of the AFM probe.....	35
Figure 2-12: Tapping mode AFM image of a gold grating using the Pt/Ir probe .....	36
Figure 2-13: Oscillation amplitude with varying voltage pulse widths.....	37
Figure 2-14: Oscillation amplitude with 10ms pulses of varying voltage.....	38
Figure 3-1: Stokes, Anti-Stokes Raman scattering and Rayleigh scattering.....	42
Figure 3-2: Schematic diagram of a Raman spectroscopy system .....	47
Figure 3-3: Stokes and anti-Stokes Raman scattering spectrum of Silicon (100).....	48

## LIST OF FIGURES -- *Continued*

Figure 3-4: Metal nanosphere.....	51
Figure 3-5: Scattered electric fields $E_x$ , $E_y$ , $E_z$ and $E_t$ in a plane parallel to the aperture, at (a) $z = 1$ nm, (b) $z = 10$ nm and (c) $z = 100$ nm .....	55
Figure 3-6: Scattered electric fields $E_x$ , $E_y$ , $E_z$ and $E_t$ in a plane parallel to the Flower, at (a) $z = 1$ nm, (b) $z = 10$ nm and (c) $z = 100$ nm .....	56
Figure 3-7: Method of fabricating flower structure.....	57
Figure 3-8: An AFM topography image of flower structure .....	57
Figure 3-9: SERS effect of flowers structure .....	58
Figure 3-10: Method of coating Au particles onto a glass cover slip.....	59
Figure 3-11: An AFM topography image of monolayer of Au particles.....	60
Figure 3-12: SERS of $\beta$ -carotene sample on the Au particle monolayer .....	61
Figure 3-13: Field enhancement factor of a silver AFM tip.....	64
Figure 3-14: NRS-SERS contrast.....	66
Figure 3-15: Numerical aperture and depth of focus.....	67
Figure 3-16: Airy pattern.....	68
Figure 3-17: Gaussian beam focus .....	70
Figure 3-18: Collection efficiency of Raman photons with NA of the optics.....	73
Figure 3-19: Solid immersion lens system .....	74
Figure 3-20: Intensity distribution of the $x$ -component of the electric field at $z = 0$ .....	76
Figure 3-21: Intensity distribution of the $z$ -component of the electric field at $z = 0$ .....	77
Figure 3-22: Intensity distribution of the $y$ -component of the electric field at $z = 0$ .....	77



## LIST OF FIGURES -- *Continued*

Figure 3-23: Distribution of the optical field with radius $r$ at $z = 0, \lambda/8, \lambda/4,$ and $\lambda/2$ .....	80
Figure 3-24: Knife-edge test of the focused field profile .....	81
Figure 3-25: Schematic diagram of a Raman-AFM system .....	83
Figure 3-26: Temperature control and mode stabilization stage of the laser diode .....	84
Figure 3-27: Holographic laser bandpass filter .....	85
Figure 3-28: Spatial filtering of the laser beam .....	86
Figure 3-29: Schematic diagram of a MS257 monochromator .....	88
Figure 3-30: Schematic diagram of the inverted microscope .....	91
Figure 3-31: Tip enhanced Raman scattering of Rhodamine 6G sample .....	93
Figure 3-32: Stokes/anti-Stokes ratio with temperature for a shift of $1000\text{cm}^{-1}$ .....	96
Figure 3-33: Steady state temperature measurements using Raman spectroscopy .....	97
Figure 3-34: Temperature evolution through the film as a function of time .....	99
Figure 3-35: Transverse and lateral heat diffusion .....	100
Figure 3-36: Raman Stokes/anti-Stokes ratio against time and horizontal distance .....	100

## ABSTRACT

Scanning Probe Microscopy (SPM) has been proven to be a powerful tool for imaging and lithography with nanometer resolution. The application of SPM to data storage may produce aerial storage densities far greater than what is currently available. As an effort in this direction, the properties of reversible transitions on the molecular scale in a complex of 3-nitrobenzal malononitrile and 1,4-phenylenediamine have been studied, by application of local electric field pulses from a SPM probe. Current pulses injection during the operation of a conducting-tip tapping-mode atomic force microscope has also been developed. Combination of these two techniques should be of importance for MEMS-based data storage. Another effort of ours is to develop an experimental configuration by combining the analytical power of Raman spectroscopy with the nanometer resolution of atomic force microscopy (AFM). Here, an AFM silicon nitride probe, coated with a 40 nm silver layer, was used to significantly enhance the Raman signal by laser excitation of surface plasmons in the tip coating. Experimental results indicate a local surface enhanced Raman scattering (SERS) increase of  $10^5$ . Lateral scanning of the sample and collecting the SERS signal allows for a 2D image of the chemical identity of the probed sample simultaneous with its topography as measured by the AFM. Also, the ratio of Stokes to anti-Stokes can be used to obtain an absolute map of the local temperature across the sample.

# 1 SCANNING PROBE MICROSCOPY

Scanning Probe Microscopy (SPM) [1] consists of a family of microscopy techniques where a sharp probe is scanned across a sample surface while some probe-sample interaction or interactions are monitored. The two primary forms of SPM are Scanning Tunneling Microscopy (STM), and Atomic Force Microscopy (AFM).

STM was invented in 1982 by G. Binnig, E. Rohrer, C. Gerber and H. Weibel [2] at IBM in Zurich, Switzerland. Binnig and Rohrer won the Nobel Prize in Physics for this invention in 1986. AFM, also known as Scanning Force Microscopy (SFM), was developed by G. Binnig, C. F. Quate, and C. Gerber [3] as a collaboration between IBM and Stanford University in 1986. These two complementing technologies fulfilled such a needed technology that their understanding and use grew exponentially immediately after their invention. Nowadays, they have become powerful, established techniques for imaging and lithography with nanometer resolution.

## 1.1 Scanning Tunneling Microscopy

A schematic of the basic STM design is shown in Fig. 1-1. Conceptually, the fundamental components comprising STM are two electrodes, the tip and the sample, which are typically positioned about  $d = 1 \sim 10 \text{ \AA}$  apart. A voltage bias  $V$ , usually ranging from 20 mV for conductors to 3 V for semiconducting materials, is applied between the tip and sample to induce the tunneling of electrons through the air gap. The tunneling current,  $i$ , between the conductive tip and sample is exponentially dependent on their separation  $d$ . This can be represented by the equation,

$$i \sim V e^{-\alpha d} \quad (1.1)$$

where  $\alpha$  is a constant defined by the work functions of the two electrodes.

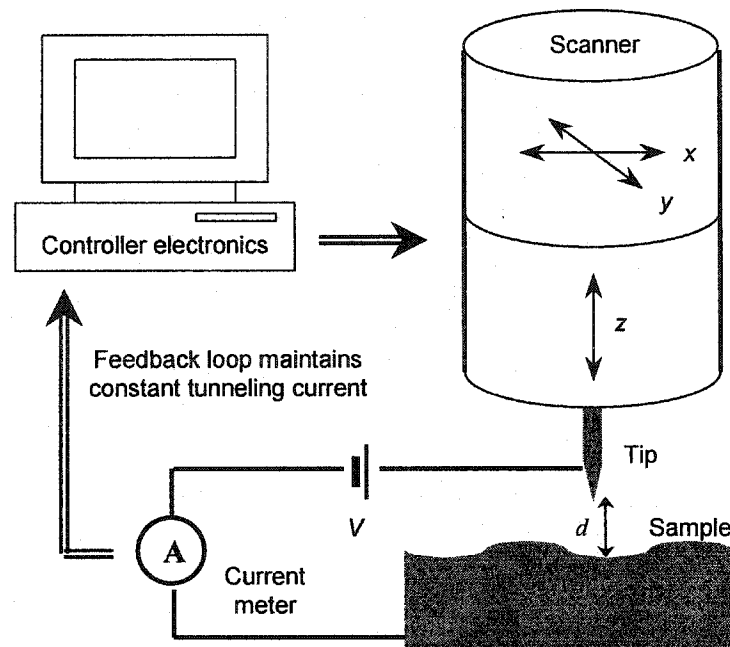


**Figure 1-1: A diagram of an STM system**

For typical the parameters, i.e., Highly Ordered Pyrolytic Graphite (HOPG), one can deduce from the tunneling equation that the tunneling current is diminished about an order of magnitude for each angstrom that the gap widens. This extreme sensitivity of the tunneling current to distance gives rise to the ability of the STM to sense extremely minute variations in the height of surface features.

The probe is usually a Pt-Ir or W wire cut or etched to a sharp point where ideally a single atom resides at the apex, since the ultimate resolution of the imaging is governed by the sharpness of the tip. A piezoelectric element raster scans the probe across the

sample surface in the  $x$  and  $y$  directions. Therefore, the STM probe encounters corrugations in the sample surface topography and local density of states, resulting in an exponential change in the tunneling current. The variation of the tunneling current is recorded and plotted by the computer to retrieve the original surface contours. This operational mode of STM, where the scanner maintains a constant vertical position while the tunneling current varies with the structure of the sample surface, is known as “current mode”. It is designed to attain atomic resolution images over small regions (1 – 40 nm) of samples with very slight corrugations.

To prevent the tip from crashing into the sample while scanning the highly corrugated sample over a broader region (50 nm – 100  $\mu\text{m}$ ), a feedback loop is employed to maintain a constant tunneling current “setpoint” by adjusting the  $z$  position of the piezo scanner at each  $(x, y)$  data point, as shown in Fig. 1-1. While maintaining a constant tunneling current, the air gap separating the tip and sample remains approximately constant. Therefore, the  $z$  positions of the piezo scanner at each  $(x, y)$  data point, which reflect the surface topography and local density of states, are stored by the computer to form the a surface image. This operational mode of STM, where the tunneling current maintains a constant value while the vertical position of the scanner varies with the height of the surface, is known as “height mode”.

The STM technique is typically limited to conducting and semiconducting surfaces. To image the topography of non-conducting surfaces with nanometer resolution, one has to employ AFM technique.

## 1.2 Atomic Force Microscopy

### 1.2.1 Contact Mode Atomic Force Microscopy

There are 3 primary operational modes of AFM: the contact mode, the tapping mode and the non-contact mode. The contact mode AFM operates by scanning a sharp tip attached to the end of a thin cantilever across a sample surface while monitoring the change in cantilever deflection, as shown in Fig. 1-2.

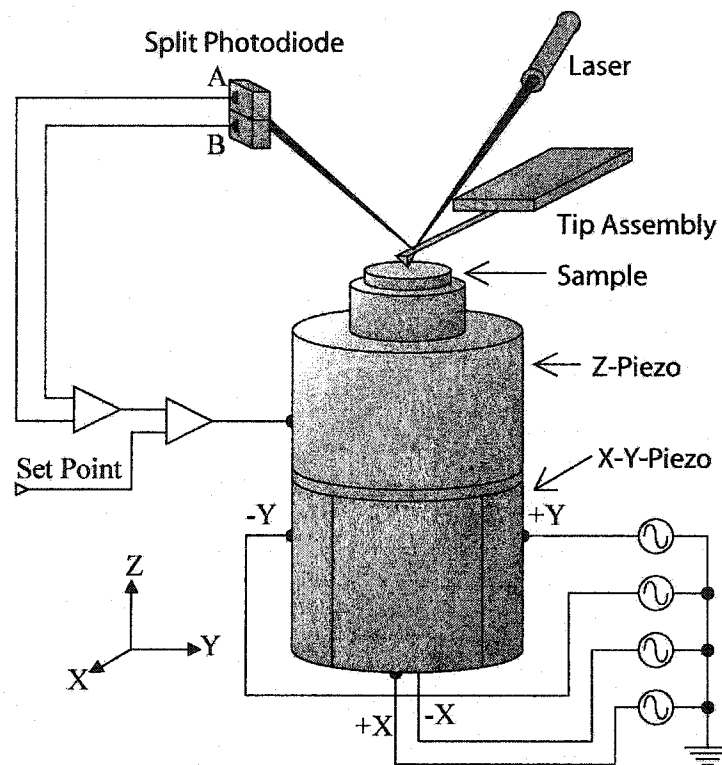


**Figure 1-2: Diagram of an AFM system**

A laser beam is reflected off the back surface of the cantilever and is incident on a split photodiode. While the cantilever is in its relaxed position with the sample far from the tip, the photodiode is aligned such that the light falls equally on each half of the

photodiode. To image with the AFM, the sample and tip are brought into contact using a stepper motor until the cantilever deflects slightly. Then, the sample is raster scanned beneath the tip by applying an appropriate sawtooth bias to the  $x$  and  $y$  piezoelectric materials, and the cantilever deflection changes according to the surface topography of the sample. The easiest method for obtaining an image is simply to note the cantilever deflection at each  $(x, y)$  data point by measuring the difference between the laser intensity signals from each half of the photodiode. This operational mode is known as "constant height mode". The scanner on which the sample is mounted maintains a constant vertical position while the tip-sample force varies with the deflection of the cantilever according to Hooke's Law,  $F = -k \cdot s$ , where  $s$  is the deflection distance and  $k$  is the spring constant of the cantilever. The spring constants usually range from 0.01 to 1.0 N/m, resulting in forces ranging from nN to  $\mu$ N, which sometimes may damage a soft sample.

A more accurate technique for imaging is called the "constant force mode". In this mode, while scanning the sample in the  $(x, y)$  directions, a feedback loop maintains a constant deflection "setpoint" between the cantilever and the sample by adjusting the bias to the  $z$ -piezoelectric and raising or lowering the scanner vertically at each  $(x, y)$  data point. While maintaining a constant cantilever deflection, the force between the tip and the sample remains constant. At each  $(x, y)$  data point, the bias applied to the  $z$ -piezoelectric is calibrated in units of vertical distance  $z$  and stored by the computer. Therefore, a 3D  $(x, y, z)$  topographic image of the sample surface can be formed.

Contact mode AFM can yield atomic resolution images on smooth surfaces. However, for soft samples, i.e., biological samples and polymers, lateral (shear) forces can distort

features in the image. The forces normal to the tip-sample interaction can be high in air due to capillary forces introduced by the adsorbed fluid layer on the sample surface. The combination of lateral forces and high normal forces can result in reduced spatial resolution on soft materials and may damage them due to friction between the tip and sample.

### 1.2.2 Tapping mode AFM and non-contact mode AFM

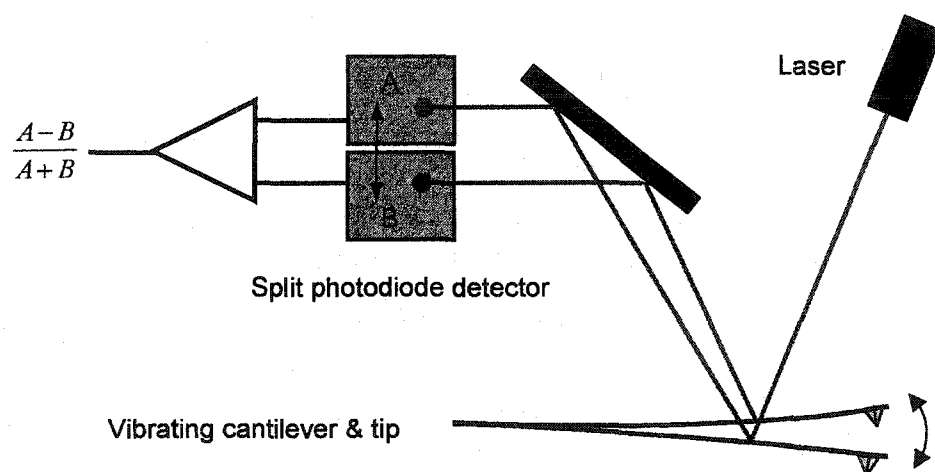


**Figure 1-3: Diagram of a tapping mode AFM system**

Tapping mode AFM and non-contact mode AFM operate by scanning a tip attached to the end of an oscillating cantilever across the sample surface while monitoring the change in the amplitude of the cantilever oscillation, as shown in Fig. 1-3.

In the case of tapping mode AFM, a piezoelectric stack (bimorph) vertically drives the cantilever's substrate at or near its resonance frequency, causing the cantilever to oscillate with an amplitude ranging typically from 20 nm to 100 nm. As the cantilever vibrates up and down, a laser beam is reflected from its top surface and directed on a split



photodiode, generating a sinusoidal electronic signal that is coupled into feedback electronics.

To image with the AFM, the sample and tip are brought into contact using a stepping motor until the cantilever oscillation amplitude decrease slightly and the tip lightly “taps” on the sample surface, contacting the surface at the bottom of its swing. Then, the sample is raster scanned by applying appropriate sawtooth bias to  $x$  and  $y$  piezoelectric materials. During the scanning, the feedback loop maintains a constant “setpoint” of the cantilever oscillation amplitude by adjusting the bias applied on the  $z$ -piezoelectric of the scanner to maintain a constant tip-sample interaction at each  $(x, y)$  data point. The distance the scanner moves vertically at each  $(x, y)$  data point is stored by the computer to form the topographic image of the sample surface.

Lateral forces are virtually eliminated in tapping mode, so there is a higher lateral resolution, lower forces and less damage to soft samples imaged in air compared to that of a contact mode AFM.

In the case of a non-contact mode AFM, the cantilever is oscillated with an amplitude of a few nanometers ( $<10$  nm) at a frequency that is slightly above the cantilever’s resonance frequency. During scanning, the tip does not contact the sample surface, but oscillates above the adsorbed fluid layer on the surface of the sample. The cantilever’s resonant frequency is decreased by the Van der Waals forces, which extend from 1 nm to 10 nm above the adsorbed fluid layer, and by other long range forces that extend above the surface. The decrease in resonant frequency causes the amplitude of oscillation to decrease. The feedback loop maintains a constant oscillation amplitude by vertically

moving the scanner at each  $(x, y)$  data point until a "setpoint" amplitude is reached. The distance the scanner moves vertically at each  $(x, y)$  data point is stored by the computer to form the topographic image of the sample surface.

While imaging with non-contact mode AFM, no force is exerted on the sample surface. Thus, there is no damage to soft samples imaged in air. The non-contact mode usually only works on extremely hydrophobic samples, where the adsorbed fluid layer is at a minimum. If the fluid layer is too thick, the tip becomes trapped in the adsorbed fluid layer causing unstable feedback and scraping of the sample. Due to these disadvantages, applications for non-contact mode AFM imaging have been limited.

## 2 APPLICATIONS OF SPM TO DATA STORAGE

The field of nanotechnology has recently been recognized as a major technological frontier that is expected to have a significant impact on virtually all aspects of human activities, spanning the whole range from research to manufacturing to consumer products. One of the holy grails of nanotechnology is the application of scanning probe microscopy (SPM) to data storage [4-6], where the combination of novel storage media and novel read/write methods present a new challenge to the performance of currently available hard drives. Such a technology may produce aerial storage densities far greater than what is currently available, with access times at least comparable to current technology, by utilizing parallel arrays of cantilevers [7].

### 2.1 Reversible, Nanoscale Transitions in an Organic Complex

Gao *et al.* published a breakthrough paper in which a storage medium consisting of conjugated organic materials that exhibited one-nm bits written, read, and erased by a STM was described [8]. The media consisted of a 1:1 mix of NBMN (3-nitrobenzal malonitrile) and pDA (1,4-phenylenediamine) whose structures are shown in Fig. 2-1 (A). The STM image in Fig. 2-1 (C) shows that the NBMN-pDA film (on HOPG substrate) used in Gao's experiment has a crystalline order.

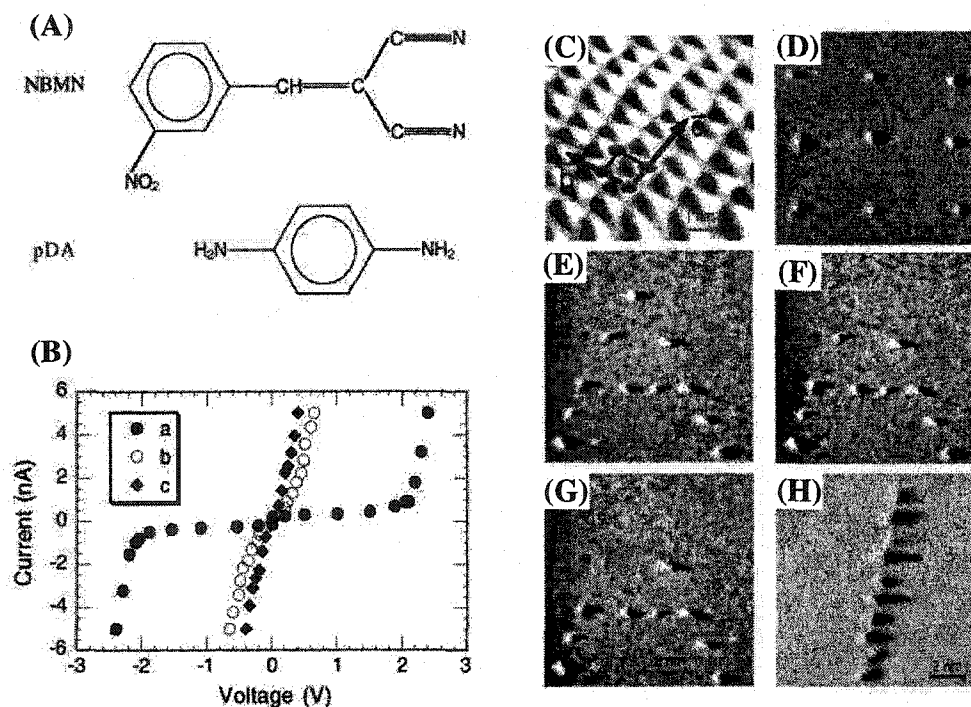


**Figure 2-1: One-nm bits written, read, and erased on an organic complex by STM**

[8]

In Gao *et al.*'s experiment, a scanning tunneling microscope (STM) was employed to write nanometer size bits on a 20-nm thick film by applying 3.5 V and 2  $\mu$ s voltage pulses. A 3 nm x 3 nm bits array was formed by this method, as shown by the STM image in Fig. 2-1 (D). Figure 2-1 (H) shows a resolution test using voltage pulses of 4.2 V and 10  $\mu$ s. The distance between neighboring marks is 1.7 nm. Figure 2-1 (E) shows an "A" pattern formed by voltage pulses of 4 V and 1  $\mu$ s. The marks would disappear after applying a reversed polarity pulse of -4.5 V and 50  $\mu$ s, as depicted by Fig. 2-1 (F) and (G). However, when the erasing pulse was applied without reversing the polarity, the bit was incompletely erased. Also reported was that all bits could be erased on heating the

sample above 423  $^{\circ}\text{K}$ . The erasing process was considered as a combined effect of the applied field and a local heating induced by the current passing through the conducting bit.

Typical  $i$ - $V$  (current-voltage) curves in Gao *et al.*'s work were measured on a bit as shown in Fig. 2-1 (B). Curve (a) is taken before the voltage pulse, indicating a low conductance. Curve (b) is taken after the voltage pulse, indicating a high conductance. Curve (c) shows the linear  $i$ - $V$  relation from the HOPG substrate. The claim in Gao *et al.*'s paper was that bias pulses in the STM experiment induced a local conductance switching across the film, similar to the conductance switching observed with a four-point probe experiment on a thicker film.

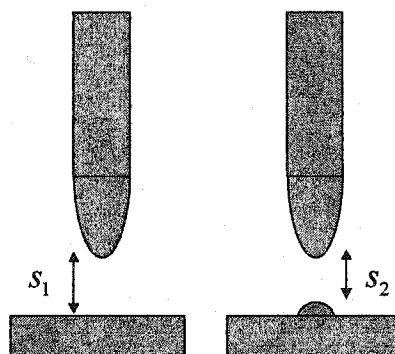


**Figure 2-2: Local modification of the organic film by the tip-sample electric field**

However, an analysis of Gao *et al.*'s STM  $i$ - $V$  curves suggests a different interpretation of the physics behind the formation and erasure of the 1-nm bits. The interpretation is that the otherwise smooth 20-nm thick organic film was locally modified by the intense tip-sample electric field ( $\sim 3$  V/nm), creating a local mound with a diameter of 1 nm and a given height  $h$ , as shown in Fig. 2-2 [10]. Similar results of a local disorder produced by

the application of a pulse to the STM tip was already reported before [9]. Since during the voltage sweep the STM tip has to be kept stationary by freezing the feedback electronics, the original tunneling gap  $s_1$  will decrease to  $s_2 = s_1 - h$ . The decreased tunneling gap  $s_2$ , on top of the mound, will give rise to a larger tunneling current, which is roughly exponential in the gap distance. Consequently, the STM  $i$ - $V$  curves before and after the application of the pulse will show different gap resistances. Also, the STM image will produce a contrast on top of the bit mound, appearing as an enhanced conductivity. To analyze the STM  $i$ - $V$  curves, a widely acceptable model [1] for the tunneling current  $i_t$  is used. The current is given by

$$i_t = \frac{A_0 \cdot e^2}{2\pi \cdot h \cdot s^2} [\phi \cdot e^{-A \cdot s \sqrt{e\phi}} - (V_t + \phi) \cdot e^{-A \cdot s \sqrt{e(V_t + \phi)}}] \quad (2.1)$$

where

$A = 4\pi\sqrt{2m_e/h^2}$  and  $\phi = \phi - V_t/2$  for  $V_t < \phi$ . For  $V_t > \phi$ , one uses  $s = s \cdot \phi/V_t$  and  $\phi = \phi/2$ . Here,  $V_t$  is the tunneling bias,  $A_0$  is the tunneling area,  $m_e$  and  $e$  are the effective electron mass and (positive) charge, and  $\phi$  and  $s$  are the apparent barrier height and tunneling gap, respectively. Obtaining the tunneling current as a function of the total voltage,  $V_t$ , applied to the STM in series with a resistor  $R$  that simulates a resistive organic film, requires a self consistent solution. The  $i$ - $V$  curves reported by Gao *et al.* could be replicated only by choosing  $\phi = 2$  eV,  $A_0 = (0.1 \text{ nm})^2$ ,  $s_1 = 0.5 \text{ nm}$  and  $s_2 = 0.3 \text{ nm}$  for the low and high apparent conductivities, respectively. These curves are shown in Fig. 2-3 (a) and (c), which were obtained by choosing  $R = 1$

$M\Omega$  for  $s_1 = 0.5 \text{ nm}$  and  $s_2 = 0.3 \text{ nm}$ . The range of parameters that can replicate Gao *et al.*'s results is quite narrow. Note that  $\phi$  is dictated by the elbow of the  $i$ - $V$  curve and  $R$  must be smaller than about  $1 \text{ M}\Omega$ . For example, curves (b) and (d) were obtained by choosing  $R = 50 \text{ M}\Omega$  for  $s_1 = 0.5 \text{ nm}$  and  $s_2 = 0.3 \text{ nm}$ .

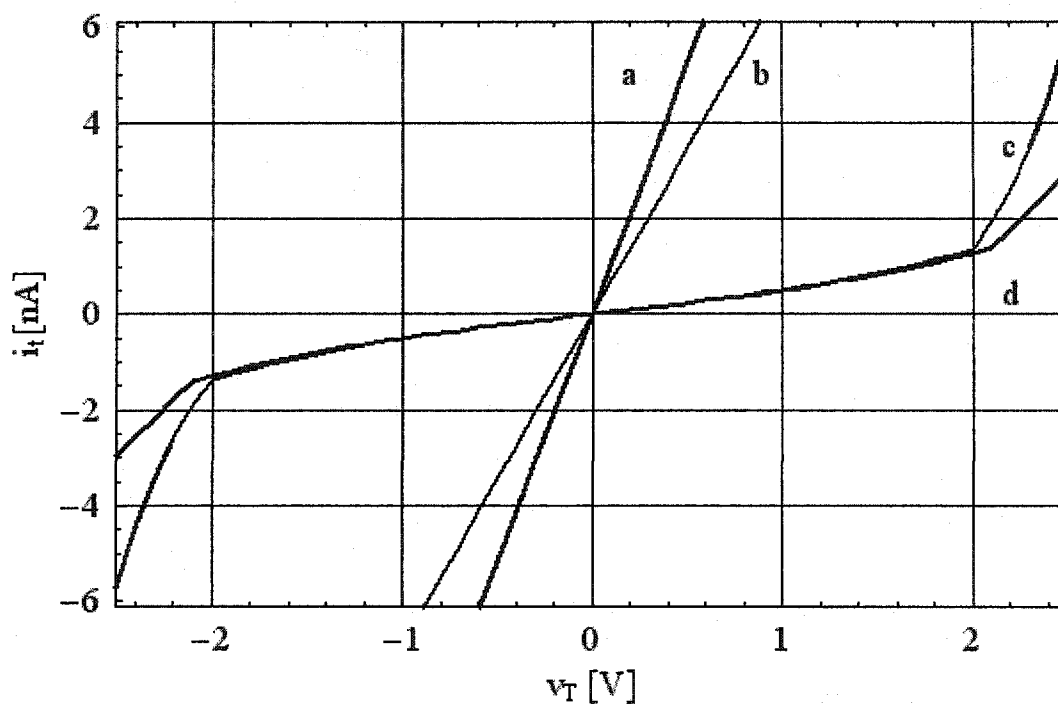


**Figure 2-3:  $i$ - $V$  curve change associated with the local modification of the film [10]**

The plausibility of the interpretation is based on the fact that since switching the 200 nm-thick-film required 3.5 V, the switching voltage for the 20-nm thick film, for the same applied field, would require only 0.35 V. Such a small value of applied gap bias would not produce a measurable tunneling current across a 20-nm thick film if it had the very high resistance reported in the paper. For example, Gao's paper quotes four-point

probe resistivity values of  $\rho = 10^{-8} \Omega \text{ cm}$  and  $\rho = 10^{-4} \Omega \text{ cm}$ . A private communication with K. Sohlberg corrected these values to  $\sigma = 10^8 \Omega^{-1} \text{ cm}^{-1}$  and  $\sigma = 10^4 \Omega^{-1} \text{ cm}^{-1}$  for the two phases. Now, since the resolution of the STM images is about 0.1 nm, the tunneling area is  $10^{-2} \text{ nm}^2$ . For a 20-nm thick film, therefore, one obtains resistances of  $2 \times 10^{18} \Omega$  and  $2 \times 10^{14} \Omega$ , respectively. Note that even resistance values several orders of magnitude smaller would not be realistic for a tunneling process.

As noted before, the maximum film resistance should be within 1 M $\Omega$ . For the 20-nm-thick film, this resistance yields a conductivity value around  $10^{-4} \Omega \text{ cm}$ . Clearly, the composition of the 20-nm-thick film differs from that of the 200-nm-thick film, an argument that supports the notion that the changes generated by applying a pulse to the STM bias does not change the resistivity of the film, but rather gives rise to a local disorder. This disorder would create a mound on the otherwise perfectly smooth area. The disordered mound could be recrystallized to form again a smooth surface by a thermal effect produced by a 50  $\mu\text{sec}$ -long tip-sample bias.



## **2.2 Injected Current Pulses with Conducting-tip, Tapping-Mode AFM**

### **2.2.1 Introduction**

Although tapping mode (intermittent mode) atomic force microscopy has been proven to be a powerful tool for imaging the topography of surfaces with high resolution [11], it is still not a fully understood phenomenon [12]. For example, averaging over several hundred taps per pixel is required in order to obtain a high quality image. This averaging is required because the interaction per tap involves a large number of parameters that are either not known or are difficult to control. Considering the fact that the tapping mode involves a driven, damped oscillator, it is apparent that the motion of the AFM probe traces a chaotic trajectory [1, 13, 14], necessitating an averaging process. For most imaging or nanofabrication purposes, such an averaging, combined with an appropriate image processing procedure, can indeed yield images with nanometer resolution.

However, data storage based on micro-electro-mechanical systems (MEMS) is expected to employ hundreds of AFM probes operating in parallel, each interacting with a media to write, read, and rewrite information at a high bit rate [15]. Clearly, if one were to adopt a tapping mode of operation, even an averaging over several taps would lower the bit rate significantly. Therefore, non-chaotic, reproducible interactions for every single tap is required while utilizing conducting-tip tapping mode AFM to inject current pulses in MEMS based data storage system.

There are two key issues regarding the requirement that each tap produces a controlled interaction. The first issue concerns the identification of conditions under which (a)

chaotic motion of the AFM probe is minimized [14], and (b) good tip-sample contact be established [16]. The second issue concerns the means by which one can observe these individual interactions. The difficulty in measuring tip-sample interactions during an individual tap stems from the fact that most of the time the tip is far away from the sample, and only during a small fraction of a cycle does it actually sense the presence of the sample. Also, it is the nature of the tapping mode of operation that the tip approaches the sample at a relatively small velocity, which is the reason why it acts as a grazing impact oscillator [17, 18]. The electrical contact between tip and sample has been chosen as the measuring tool for the reproducibility of the interaction for individual taps. This choice is clearly compatible with storage modalities in which current injection into storage media give rise to writing and reading of phase-change data [19] and of magnetic data [20].

Although a large body of literature has addressed the issue of conducting AFM probes operating in the contact mode [21], only a few theoretical and experimental results have been published for operation in the tapping mode. For example, real, tunneling, and displacement currents during the motion of the AFM probe, while applying a constant tip-sample bias, had already been addressed [22]. Experimental results where such a modality was used for nanofabrication highlighted the complexity of the tip-sample interactions and, at the same time, its usefulness as a high-resolution lithography tool [23-25]. Applications of a sinusoidal tip-sample bias, synchronous with the motion of the AFM probe, and a pulsed tip-sample bias applied during their contact, have demonstrated a substantial improvement in nanofabrication technology. These demonstrations,

however, did not consider individual tip-sample interactions, but rather an average of a large number of taps, whose interaction culminated with a fabrication process. Note, also, that in most of these experiments the tapping amplitude was small enough to sustain a constant tip-sample contact through a high resistance water neck [26]. However, for storage applications, a larger tapping amplitude is required in order to obtain a large enough impact pressure resulting in a small resistance and large current densities.

### **2.2.2 Modeling**

The tapping experiments consisted of approaching a gold sample until the amplitude of vibration decreased to 50% of its free amplitude. A well-known model for the tapping mode [1] is used to compute the motion of the AFM probe after steady-state conditions have been reached. The resultant motion of the AFM probe (solid line) for one oscillation period and the associated contact conductance (dashed line) are shown in Fig. 2-4.

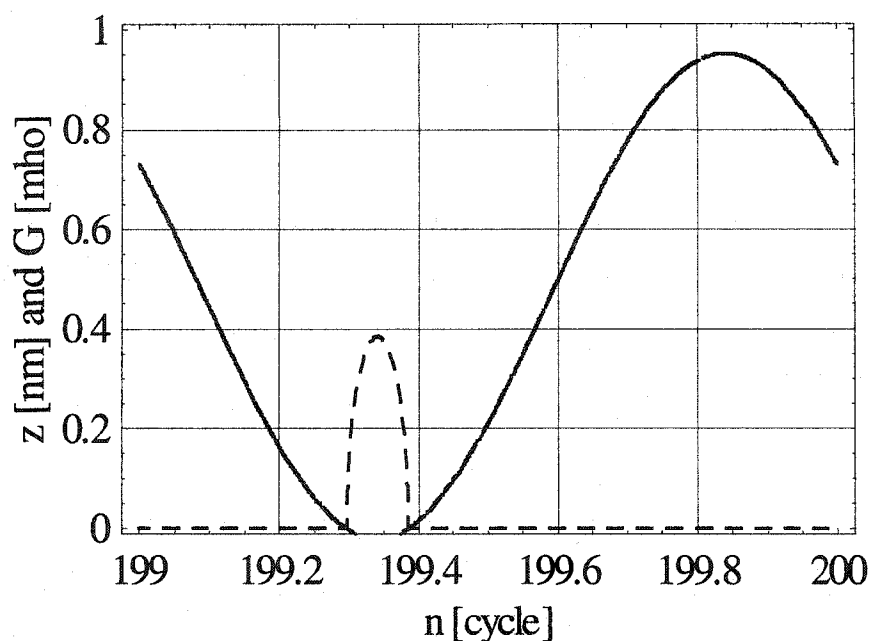


**Figure 2-4: Calculated, scaled AFM probe motion Z and conductance G [27]**

### 2.2.3 Experiment

In this section, experimental results using a tapping mode AFM [28] with an all-metal probe [29] is demonstrated. The probe was fabricated from a rectangular Pt/Ir wire whose length, width and thickness were 1,200  $\mu\text{m}$ , 100  $\mu\text{m}$ , and 50  $\mu\text{m}$ , respectively. One end of the cantilever was attached to a driving bimorph and the other end etched to produce a tip whose apex radius was estimated to be 70 nm. The spring constant, resonance frequency, amplitude of vibration, and quality factor of the probe were 300 N/m, 13 kHz, 100 nm, and 100, respectively. The bimorph drives the probe vertically at or near its resonance frequency. As the cantilever vibrates up and down, the sample and tip are brought into contact using a stepping motor until the cantilever oscillation amplitude decreases slightly and the tip lightly “taps” on the sample surface, contacting the surface at the

bottom of its swing. Current pulses were generated by applying a short voltage bias pulse during the tip-sample contact time. Each current pulse, lasting up to 20  $\mu\text{s}$ , could produce a current density of  $\sim 10 \mu\text{A}/\text{nm}^2$ . Such a current density is large enough to be applicable for phase-change and magnetic data storage.

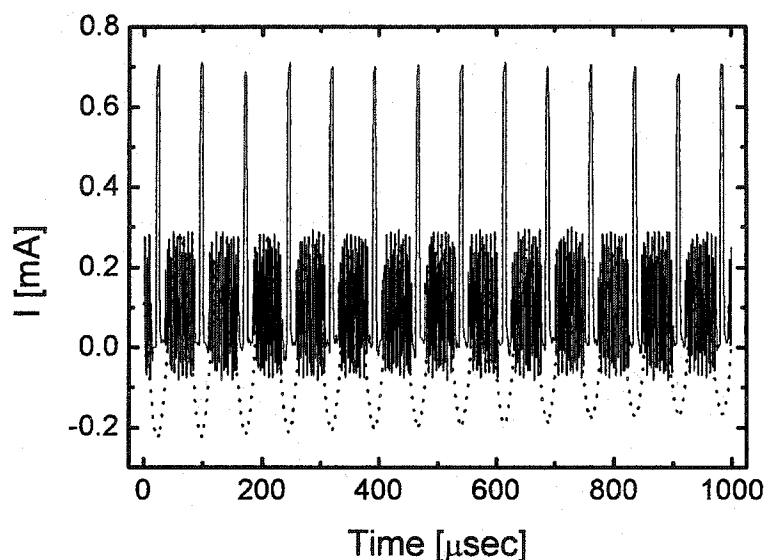


**Figure 2-5: A typical current pulse train, and the associated AFM probe motion [27]**

In the experimental procedure, long trains of individually injected current pulses were obtained while tapping at the same position. Figure 2-5 shows 14 non-averaged, experimental current pulses (solid line) and their associated AFM probe motion (dashed line) with a background of instrumental noise. The pulsed voltage bias was in phase with the AFM probe's lowest position. The current pulses demonstrate the reproducibility of the conductance established during each tap.

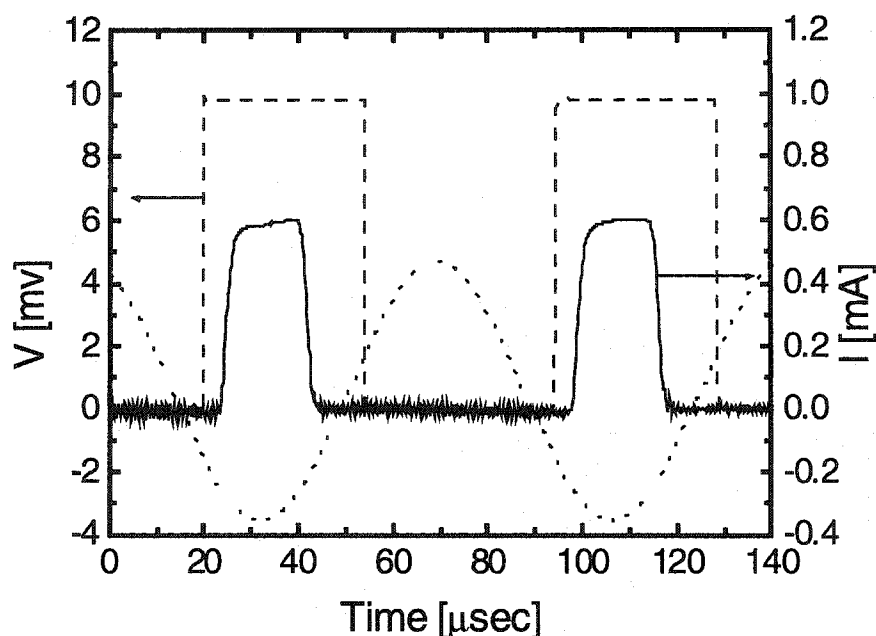


**Figure 2-6: Two current pulses, bias voltage pulses, and AFM probe motion [27]**

Figure 2-6 shows averaged current pulses (solid line) with their input bias pulses (dashed line), and the associated AFM probe motion (dotted line). Note that the tip-sample contact time is revealed by the duration of the current pulse, 16  $\mu\text{s}$ , which is shorter than the duration of the applied voltage bias pulse, 35  $\mu\text{s}$ . Here, the amplitude of the bias pulse was 10 mV, and the timing of its application relative to the motion of the AFM probe was provided by the output of the atomic force microscope photodiode.

The current pulses, with a magnitude of 0.5 mA, are much larger than the tunneling current occurring while the tip is within a fraction of a nanometer from the surface. Also, the displacement current, due to the motion of the AFM probe and the time-varying nature of the applied bias, is expected to be much smaller than the observed current

pulses. Thus, the observed current and the finite resistance ( $17 \Omega$ ) could only originate from the electrical contact between the tip and the sample. The asymmetry of the contact with respect to the AFM probe oscillation minima can be attributed to the adhesion effects between the tip and sample.

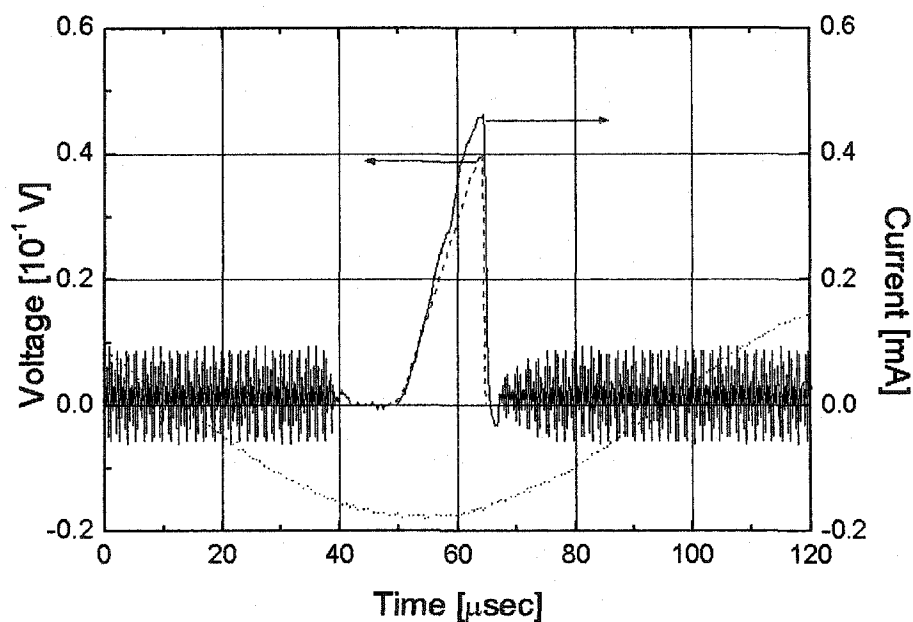


**Figure 2-7: The current pulse and the ramped input bias voltage [27]**

To further explore the electrical contact, an individual ramped bias voltage pulse was applied between the tip and the sample, and the induced current pulse was measured at the same time. Both the voltage (dashed line) and the current (solid line) are depicted in Fig. 2-7, together with the associated AFM probe motion (dotted line). The fact that the induced current also had a ramped pulse shape implies a linear relation between voltage ( $V$ ) and current ( $i$ ). This  $i$ - $V$  curve is plotted in Fig. 2-8. The good linearity demonstrates a

good ohmic contact between the tip and the sample. The curve can be used to characterize the nature of individual contacts.

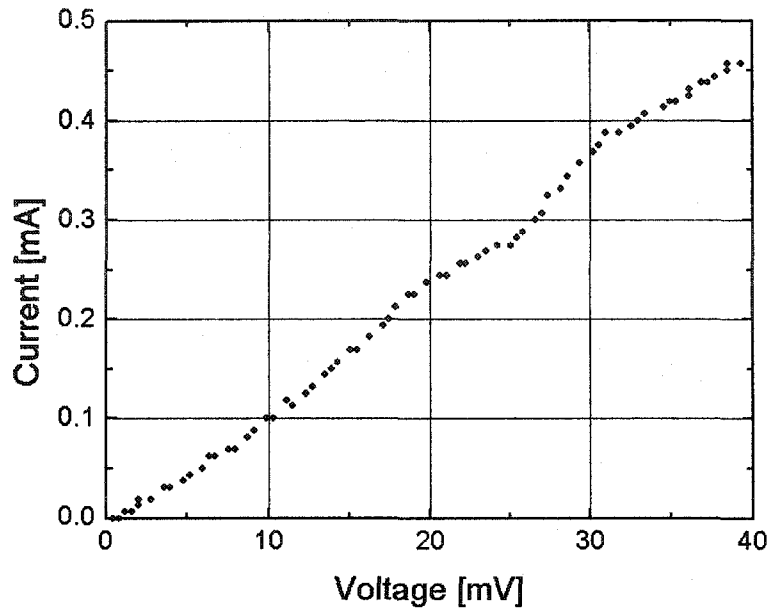


**Figure 2-8: An  $i$ - $V$  curve taken with an individual ramped input voltage pulse [27]**

Here, the operating conditions differed somewhat from those depicted in Fig. 2-5 and Fig. 2-6, producing a larger resistance ( $\sim 90 \Omega$ ).

In conclusion, Figs. 2-4 to 2-8 clearly demonstrate, both theoretically and experimentally, that it is possible to minimize the chaotic behavior of a tapping AFM probe and obtain reproducible conductance per tap. This was made possible because of the particular choice of parameters of the tapping system associated with both the dynamics of the AFM probe and the tip-sample interactions. Considering the dynamics of the tapping, one finds that the effective spring constant increases as one increases the



tapping force, resulting in an increase in the effective resonance frequency. Consequently, the chaotic behavior will be diminished, as expected for a driven, damped, non-resonant oscillating motion [17, 18]. For example, calculations yield a phase shift of 22 degrees for the gentle tapping, and 58 degrees for the hard tapping, as expected for operation off resonance. Considering now the tip-sample interaction, one can find that a tip with an apex radius of 70 nm yields a calculated force of 2.6  $\mu\text{N}$ , pressure of 7 GPa, an area of 500  $\text{nm}^2$ , and a conductance of 0.4  $\Omega^{-1}$  per tap. This conductance value compares favorably with the measured conductance, considering the fact that surface contamination, surface roughness, and adhesion forces were not taken into account. Previous work, using an analysis of force curves, has demonstrated the need to apply tip-sample forces in the  $\mu\text{N}$  range before establishing proper electric contact under ambient conditions [30].

## 2.3 All-metal tapping mode AFM probe

The key factor in making the conducting-tip tapping mode AFM a useful technique in MEMS-based data storage is that the conducting tips withstand the intense electric and mechanical stresses required, even after a large number of line scans, and so maintain their sharpness and conductivity. Commercially available conducting AFM probes are usually fabricated by coating either silicon or silicon nitride probes with thin metal films. The wear and current spikes during the scan are very easy to lead to the catastrophic failure of these coated probes. Figures 2-9 and 2-10 are two scanning electron microscope (SEM) images of the Pt/Ir-coated silicon tip, which have experienced only several  $10 \mu\text{m} \times 10 \mu\text{m}$  AFM tapping mode imaging scans. It can be observed that the tip apex had been worn down and the coating near the apex had been peeled away.

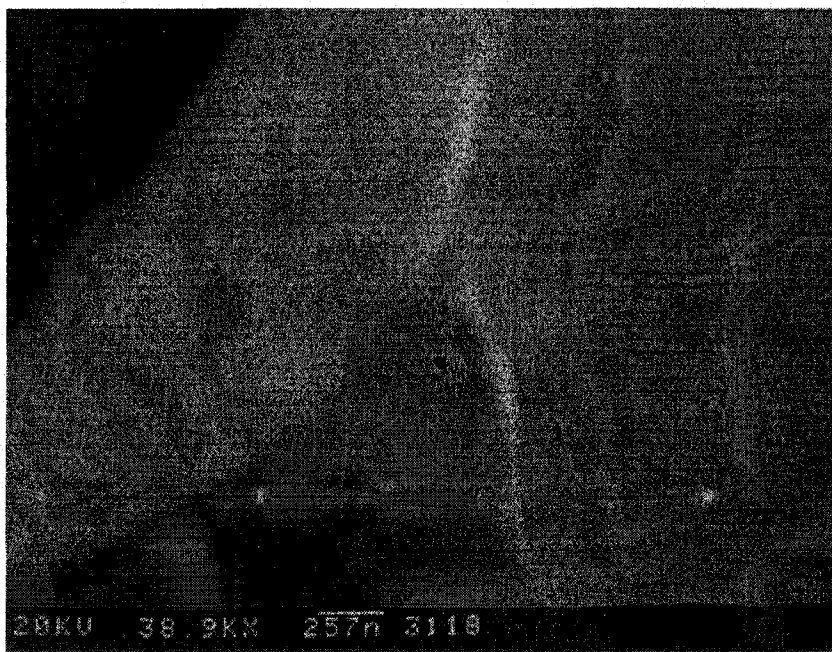
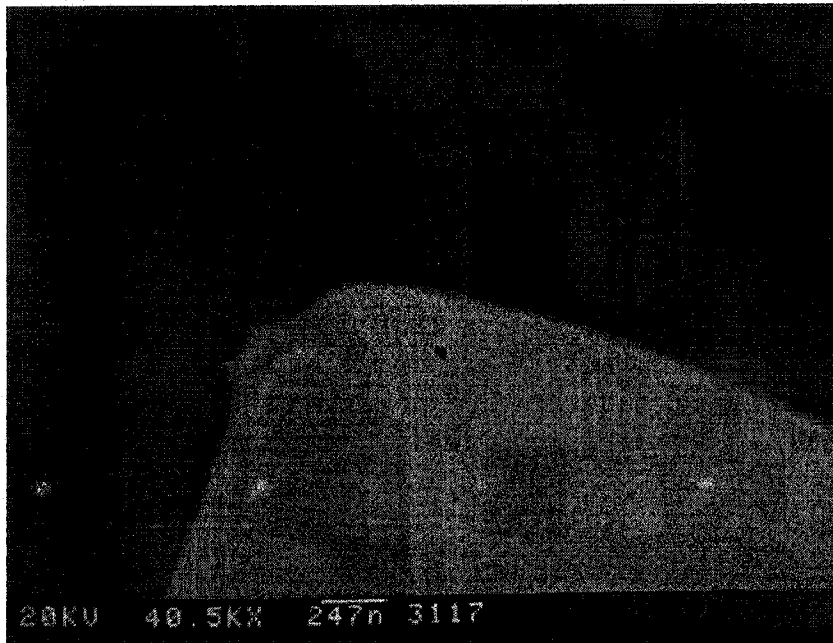


Figure 2-9: Top view SEM micrograph of a worn metal-coated silicon tip



**Figure 2-10: Side view SEM micrograph of a worn metal-coated silicon tip**

An alternative to these metal film coated probes is made possible by using home-made all-metal AFM probes that were found to be more robust. The wear and current spikes have little effect on the shape and conductivity of these novel AFM probes even after a large number of tapping mode AFM imaging scans. This section describes the fabrication and characterization of such probes.

### **2.3.1 Fabrication of the all-metal AFM probe**

To fabricate an all-metal tapping-mode AFM probe, a rectangular platinum-iridium (80%-20%) wire whose width and thickness were 100 $\mu\text{m}$  and 50 $\mu\text{m}$ , respectively, was used. The wire was soldered to a small piece of copper about the size of a commercial AFM probe substrate. This copper substrate, which served as a stable mount for the AFM probe as well as an excellent electrical contact, is then placed on the edge of an aluminum

block. The Pt/Ir soldered on the substrate is divided into two segments by the edge. The segment ( $length = 1.2\text{ mm}$ ) within the edge served as a cantilever, providing a good reflecting surface for the AFM laser. The overhanging segment of the wire is bent  $90^\circ$  with the swipe of a razor blade to form a tip. The tip is then dipped into a solution of  $2\text{M CaCl}_2$  and etched at  $10\text{V ac-voltage}$  until the reaction ceases. This electrochemical process produced a sharp tip apex whose radius was estimated to be  $70\text{ nm}$ .

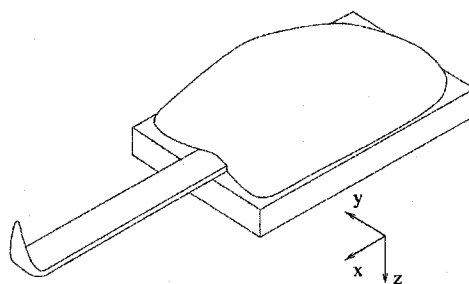


**Figure 2-11: Line art diagram of the AFM probe**

### 2.3.2 The characteristics of the all-metal AFM probe

The all-metal AFM probe, as depicted in Fig. 2-11, ensured good conductivity and could withstand a large number of tapping impacts without degrading, and a shiny surface that acted as a good mirror for the optical deflection technique. As a test of the quality of AFM images produced by metallic-wire probes, it was used to scan a gold grating with a step having a pitch of  $0.91\ \mu\text{m}$ . Its spring constant, resonance frequency, amplitude of vibration, and quality factor were measured to be  $300\text{ N/m}$ ,  $13\text{ kHz}$ ,  $100\text{ nm}$ , and  $100$ , respectively. Figure 2-12 is a tapping mode AFM image of the grating produced by a brand new metal probe.

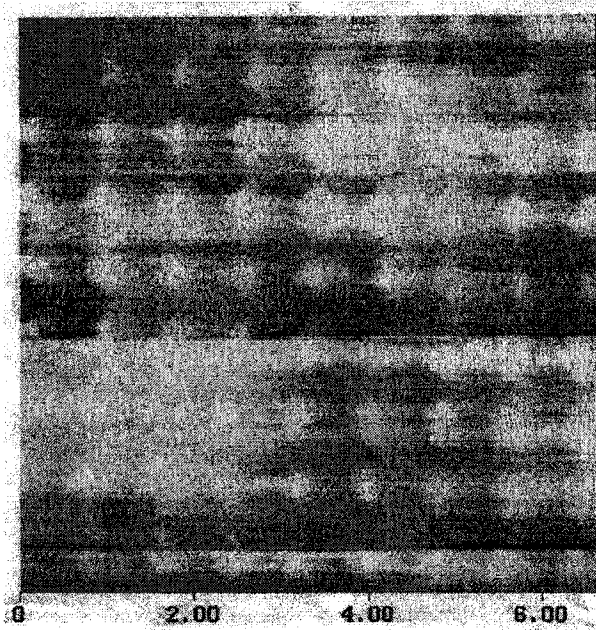


**Figure 2-12: Tapping mode AFM image of a gold grating using the Pt/Ir probe**

### **2.3.3 The effects of voltage pulse amplitude and width on the AFM probe oscillations**

During the operation of injecting current pulses in tapping mode, the metal probe and the conducting sample surface formed a capacitor. The electric energy trapped inside this capacitor is given by  $W = \frac{1}{2}C \cdot V^2$  where  $V$  is the voltage applied on the capacitor and  $C$  is the capacitance that is inversely proportional to  $d$ , the distance between the two electrodes of the capacitor (tip and sample). The electric force between the tip and sample can be represented as

$$f = -\frac{\partial W}{\partial d} = -\frac{1}{2}V^2 \frac{\partial C}{\partial d} = \frac{1}{2d}C \cdot V^2. \quad (2.2)$$

If the width and the magnitude of the voltage pulses were too large, the consequential electric force would perturb the tapping vibration of the AFM probe.

Figure 2-13 shows the relation of AFM probe oscillation amplitudes vs. distance between the tip and the sample surface. Note that the oscillation amplitude is measured by the output voltage of the photodiode detector in the AFM system. The five curves are associated with five different widths of voltage pulses applied while the tip touches the sample. The solid line, the dashed line and the dotted line in Fig. 2-13 clearly demonstrate that the AFM probe oscillation is not perturbed by the 4 V voltage pulse as far as the pulse width is shorter than 10  $\mu\text{s}$ .

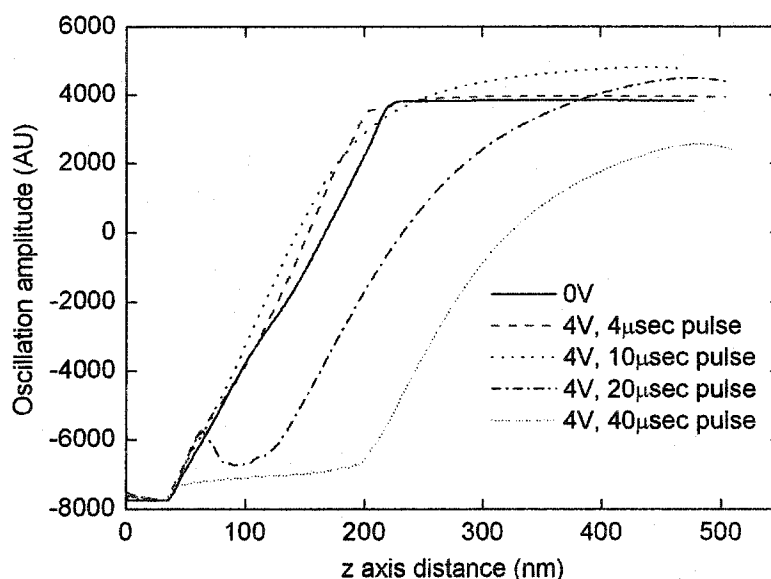


**Figure 2-13: Oscillation amplitude with varying voltage pulse widths**

The perturbation effect to the AFM probe oscillation induced by different magnitude of voltage pulses is shown in Fig. 2-14. The five curves are associated with five different

magnitudes of 10 ms voltage pulses applied while the tip touches the sample. This figure shows that 10 ms pulses do not affect oscillations for the voltage values below 2 V.

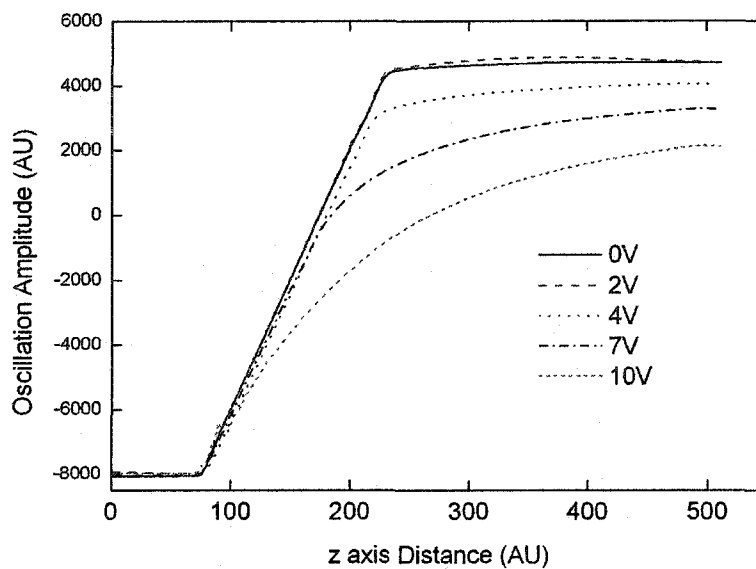


**Figure 2-14: Oscillation amplitude with 10ms pulses of varying voltage**

In the experiment, the bias pulses, applied during the tip-sample contact time, have a magnitude smaller than 100 mV and a width shorter than 100  $\mu$ s. Both values are well below the threshold of perturbing the tapping operations.

## 2.4 Conclusion

In conclusion, using a tapping mode atomic force microscope with an all-metal conducting AFM probe, reproducible tip-sample interactions have been obtained. Current density pulses, of the order of  $10 \mu\text{A}/\text{nm}^2$ , have been injected into conducting samples under a range of experimental conditions. The bias pulses, applied during the tip-sample contact time, did not perturb the tapping operations, and eliminated artifacts associated with displacement currents. The reproducible injection of current density pulses can be applied to spreading resistance measurements and to storage applications employing, for example, phase change by Joule heating and magnetic switching by spin-polarized current.

This work can be extended to commercial conducting AFM probes under controlled environmental conditions to gain a better understanding of tip-sample interactions and realize faster tapping rates [31].



### 3 APPLICATIONS OF SPM TO RAMAN SPECTROSCOPY

Raman Spectroscopy is a non-destructive characterization method that can uniquely identify the chemical and structural properties of a sample by analyzing inelastic scattering of light due to molecular thermal vibrations [32-34]. Raman spectroscopy has found applications in many fields due to the immense amount of characteristic information it can yield about a material. This technique, however, has two limitations; firstly, it is an optical spectroscopy, and therefore its spatial resolution is limited to the optical wavelength. The second limitation is that its cross-section is very small, requiring long data acquisition times and thus it is limited to the characterization of only bulk samples, in spite of the fact that characterizing local material variations is desirable in a wide variety of fields.

However, it has been known for some time [35, 36] that Raman scattering increases by many orders of magnitude in the presence of a suitably roughened metal film, the effect being known as Surface Enhanced Raman Spectroscopy (SERS). By coating the tip of an Atomic Force Microscope (AFM) with nanometer-size silver or gold granulates, the Raman signal in the vicinity of the tip is strongly enhanced and thus one can obtain a spatial resolution on the order of several tens of nm [37].

In this chapter, the potential of this technique is examined by first developing templated substrates for optimal SERS enhancement. The local distribution of electric

fields across the templated substrates has been modeled, and the resultant enhancement of the Raman signal measured, and found to be in general agreement.

Subsequently, using a suitably coated AFM tip, the SERS effect was exploited to demonstrate the use of Raman spectroscopy to gain material information on the nanoscale.

Raman spectroscopy is primarily red-shifted (Stokes shift) with respect to the excitation wavelength. There is also a blue-shifted component (the anti-Stokes shift), which can also be used as an effective measure of temperature, as the intensity of the anti-Stokes spectrum is directly related to the temperature of the material. An interesting application of this nanoscale Raman is that temperature can be directly measured with extremely high temporal and spatial resolution. It is shown that the temporal and spatial evolution of thermal pulses propagating in a thin metal film due to picosecond laser pulses can be monitored by coating the metal film with a thin organic layer and measuring the Stokes to anti-Stokes ratio. Preliminary experimental results using the Stokes to anti-Stokes ratio indicate the feasibility of this technique.

## 3.1 A Brief Look at Raman Scattering Spectroscopy

### 3.1.1 Basic concept and elementary theory

When light is scattered from a molecule, most photons are elastically scattered. The scattered photons, known as Rayleigh scattered photons, have the same wavelength as the incident photons. However, there is a small fraction of light scattered at a wavelength different from the wavelength of the incident light. This inelastic scattering phenomenon is termed the Raman effect. A quantum mechanics description of scattering is shown in Fig. 3-1 where the energy difference between the incident and scattered photons is represented by the arrows of different lengths.

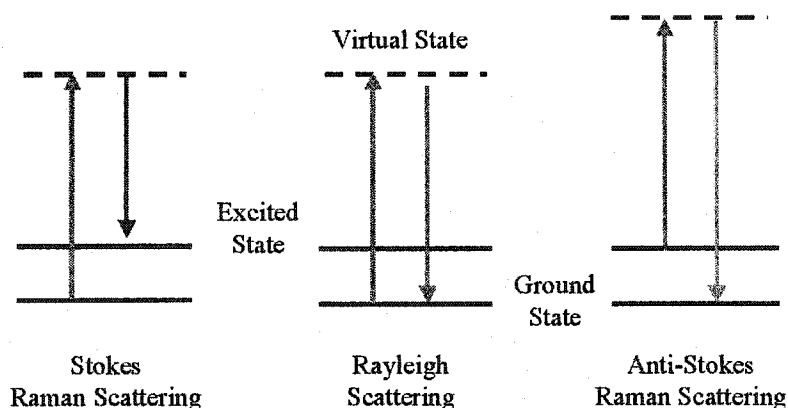


**Figure 3-1: Stokes, Anti-Stokes Raman scattering and Rayleigh scattering**

The Raman scattering arises when a molecule interacts with an incident photon and undergoes an excitation to a virtual state with nearly coincident de-excitation and a change in vibrational energy. As a result, the incident photon of energy  $h\nu_0$  is destroyed and a photon of energy  $h(\nu_0 \pm \nu_1)$  is emitted from the molecule. The photon energy gain or loss in the scattering process is taken from the vibrational energy of the molecule, and

is highly sensitive to the physical structure of the molecule. This change in energy is known either as the Stokes shift (loss of energy) or as the anti-Stokes shift (gain in energy). The scattering event occurs in  $10^{-14}$  seconds or less. The resultant spectrum of inelastically scattered light is thus highly characteristic of an individual molecule, and can be used to determine its structure with high accuracy.

Raman scattering can also be described in terms of classical physics [33]. When a molecule interacts with light, the electric field of the photons will exert forces on the electrons and the nuclei. As a result, the electrons will be displaced relative to the nuclei, and the polarized molecule will have an induced dipole moment oscillating at  $\nu_0$ , the frequency of the incident optical field. This dipole moment  $P$  is proportional to the electric field  $E$  and the polarizability  $\alpha$ ,

$$P = \alpha E \quad (3.1)$$

where

$$E = E_0 \cdot \cos(2\pi\nu_0 t). \quad (3.2)$$

The polarizability  $\alpha$  is a function of the vibrational coordinate  $Q$  of the molecule, which is oscillating at the molecular vibration frequency  $\nu_1$ ,

$$Q = Q_0 \cdot \cos(2\pi\nu_1 t). \quad (3.3)$$

Therefore, the induced dipole moment is modulated by the molecular vibrations and oscillates not only at the frequency of the incoming field ( $\nu_0$ ) but also at the sum ( $\nu_0 + \nu_1$ ) and difference ( $\nu_0 - \nu_1$ ) frequencies between the incoming light and the molecular vibrations. This results in the appearance of Stokes and anti-Stokes side bands in the re-radiated light.

The dependency of  $\alpha$  on  $Q$  can be developed in a Taylor series,

$$\alpha = \alpha_0 + \left( \frac{\partial \alpha}{\partial Q} \right) Q_0 \cdot \cos(2\pi\nu_1 t) + \dots \quad (3.4)$$

where  $\alpha_0$  is the equilibrium value of the polarizability. Thus, the induced dipole moment  $P$  can then be written as

$$P = \alpha_0 E_0 \cdot \cos(2\pi\nu_0 t) + \left( \frac{\partial \alpha}{\partial Q} \right) Q_0 \cdot \cos(2\pi\nu_1 t) E_0 \cdot \cos(2\pi\nu_0 t) + \dots \quad (3.5)$$

Using the trigonometry relation to expand the forenamed equation, one gets

$$\begin{aligned} P = & \alpha_0 E_0 \cdot \cos(2\pi\nu_0 t) + \frac{1}{2} \left( \frac{\partial \alpha}{\partial Q} \right) Q_0 E_0 \cdot \cos(2\pi(\nu_0 + \nu_1)t) \\ & + \frac{1}{2} \left( \frac{\partial \alpha}{\partial Q} \right) Q_0 E_0 \cdot \cos(2\pi(\nu_0 - \nu_1)t) + \dots \end{aligned} \quad (3.6)$$

This dipole oscillates at three frequencies, namely  $\nu_0$ ,  $\nu_0 - \nu_1$  and  $\nu_0 + \nu_1$ . The emitted optical field is given by

$$E \propto \frac{\partial^2 P}{\partial t^2}. \quad (3.7)$$

Therefore, the field  $E$  of the scattered light is

$$\begin{aligned} E \sim & \alpha_0 E_0 \nu_0^2 \cdot \cos(2\pi\nu_0 t) \\ & + \frac{1}{2} \left( \frac{\partial \alpha}{\partial Q} \right) (\nu_0 + \nu_1)^2 Q_0 E_0 \cdot \cos(2\pi(\nu_0 + \nu_1)t) \\ & + \frac{1}{2} \left( \frac{\partial \alpha}{\partial Q} \right) Q_0 E_0 (\nu_0 - \nu_1)^2 \cdot \cos(2\pi(\nu_0 - \nu_1)t) + \dots \end{aligned} \quad (3.8)$$

The  $\nu_0$  term produces an elastic scattered light unshifted in frequency, called the Rayleigh scattering. The  $\nu_0 - \nu_1$  term produces the Stokes Raman scattering, while the  $\nu_0 + \nu_1$  term produces the anti-Stokes Raman scattering.

The intensity of the emitted light is proportional to  $E^2$  yielding expressions for the Stokes and anti-Stokes Raman scattering,

$$I_{Rayleigh} \sim \nu_0^4 \alpha_0^2 I_0(\nu_0) \quad (3.9)$$

$$I_{Stokes} \sim (\nu_0 - \nu_1)^4 \left( \frac{\partial \alpha}{\partial Q} \right)^2 I_0(\nu_0) \quad (3.10)$$

and

$$I_{AntiStokes} \sim (\nu_0 + \nu_1)^4 \left( \frac{\partial \alpha}{\partial Q} \right)^2 I_0(\nu_0) e^{-\frac{h\nu_1}{kT}}. \quad (3.11)$$

The scattered power is proportional to  $\nu^4$  and to the intensity of the excitation laser. The Boltzmann factor in the anti-Stokes formula accounts for smaller anti-Stokes signal compared to the Stokes signal, since anti-Stokes starts from molecules in the excited vibrational level, which is populated according to the Boltzmann distribution.

### 3.1.2 Raman scattering is a very weak process.

In Raman scattering, the total Raman signal power  $P_R$  is the product of the Raman scattering cross-section  $\sigma_R$  (per molecule), the excitation laser intensity  $I_0(\nu_0)$ , and the number of molecules  $N$  in the probed volume,

$$P_R = N \cdot I_0(\nu_0) \cdot \sigma_R. \quad (3.12)$$

For thin film sample, the number of molecules in the probed volume is given by

$$N = n \cdot d \cdot A \quad (3.13)$$

where  $n$  is the molecule density,  $A$  is the illuminated area, and  $d$  is the thickness of the film. The excitation laser intensity  $I_0(\nu_0)$  is proportional to the incident laser power  $P_0(\nu_0)$  in case of uniform illumination,

$$I_0(\nu_0) = P_0(\nu_0) / A. \quad (3.14)$$

Thus, the total Raman scattering power can be written as

$$P_R = n \cdot d \cdot P_0(\nu_0) \cdot \sigma_R. \quad (3.15)$$

Assuming a typical sample is used in Raman scattering experiment and the properties of this sample are given by  $n = 10^{21} \text{ cm}^{-3}$ ,  $\sigma_R = 10^{-29} \text{ cm}^2$  and  $d = 100 \text{ nm}$ , the probability of Raman scattering for a single photon is

$$\text{probability} \sim P_R / P_0(\nu_0) = n \cdot d \cdot \sigma_R \sim 10^{-13}. \quad (3.16)$$

The small probability of Raman scattering for photons is because of the extremely small Raman cross-section ( $10^{-31} \text{ cm}^2 \sim 10^{-26} \text{ cm}^2$  per molecule, typically  $10^{-30} \text{ cm}^2$  for non-resonant Raman) [38-40], which is fourteen orders smaller than the cross-section of fluorescence. Thus, Raman scattering is a very weak process compared to fluorescence or IR-absorption. The challenge of the construction of “practical” Raman instruments is to enable the collection of Raman signals with acceptable signal-to-noise ratio (SNR) in reasonable data acquisition times.

### 3.1.3 An example experiment of Raman scattering

Figure 3-2 is a schematic diagram of the Raman spectrometer. This home-built system consists of a laser to illuminate the sample, a band pass filter to get rid of the unwanted-wavelength-radiations propagating together with the laser beam, an optical system to

focus the illuminating beam and collect the Raman photons, a notch filter to reject the laser line and the Rayleigh scattering, a monochromator to resolve the spectrum, and a highly sensitive optical detector (photomultiplier tube) to count Raman photons. A more detailed description of this system can be found in Section 3-5 of this dissertation.

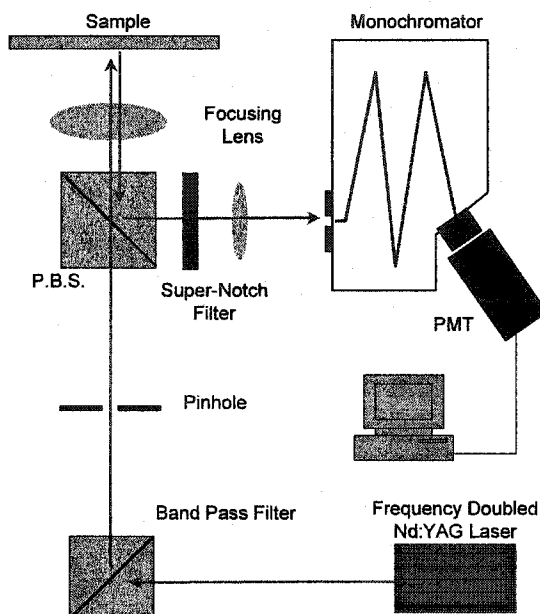


**Figure 3-2: Schematic diagram of a Raman spectroscopy system**

As a typical example, a Raman scattering spectrum of Silicon (100) was acquired using the home-built Raman spectrometer. When the wavelength of the excitation laser is 532 nm, a Stokes shifted and an anti-Stokes shifted spectrum peak are observed to be at 547 nm and 517 nm, as shown in Fig. 3-3. The anti-Stokes Raman peak is much weaker than the Stokes shifted Raman peak because the thermal population of vibrational excited state is lower than those of the ground state at room temperature. The ratio of anti-Stokes to Stokes intensity is a measure of temperature and can be used for contactless thermometry [41, 42].



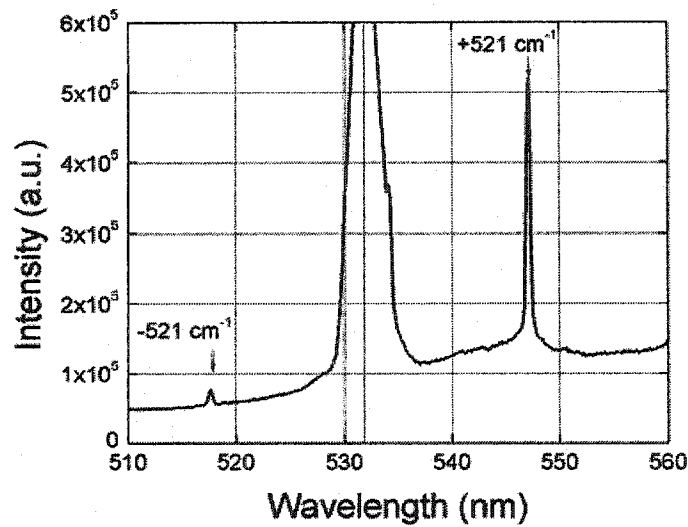


**Figure 3-3: Stokes and anti-Stokes Raman scattering spectrum of Silicon (100)**

Practically, to indicate the Raman spectrum line, the relative wavenumber ( $\text{cm}^{-1}$ ) is more frequently used than wavelength, since it is independent of the laser excitation wavelength and is determined only by the inherent property of the sample material. The definition of the relative wavenumber is given by

$$\Delta\bar{\nu} = \frac{1}{\lambda_{\text{Laser}}} - \frac{1}{\lambda_{\text{Raman}}} \quad (3.17)$$

in which  $\lambda_{\text{Laser}}$  and  $\lambda_{\text{Raman}}$  are the wavelengths of the incident and Raman scattered photons, respectively. Using this definition, the Stokes and anti-Stokes Raman shifts of Silicon (100) are calculated to be  $+521 \text{ cm}^{-1}$  and  $-521 \text{ cm}^{-1}$  respectively. Without further notice, the Raman spectrum line in the following discussion of Raman scattering will always be indicated by the relative wavenumbers.

## 3.2 Surface Enhanced Raman Scattering

### 3.2.1 Introduction to the SERS effect

The field of Surface Enhanced Raman Spectroscopy (SERS) was inaugurated [43-45] in the mid-1970s. Since then, this effect has been observed for many different molecules that have been attached to rough silver, gold or copper surfaces. Such an enhancement can also be obtained from nanometer sized metallic spheres [46] and nanoshells in a solution that contains organic material [47]. Enhancement factors were estimated to be on the order of  $10^3 \sim 10^5$  in the first reports. But later, many authors claimed much higher enhancement factors [46-48]. It is generally agreed that several mechanisms might contribute to the observed effect, including chemical enhancement and electromagnetic enhancement [38, 49, 50].

Different interpretations will now be discussed as the origin of chemical enhancement of Raman scattering. One explanation is due to a resonance Raman mechanism in which either (a) the electronic levels of the molecule are shifted and broadened by their interaction with the metal surfaces or (b) new electronic states which arise from chemisorption serve as resonant intermediate states in Raman scattering. Another interpretation of the chemical enhancement is attributed to a so-called dynamical charge transfer from the metal surfaces into an unoccupied orbital of the analyzed molecules, or from the occupied orbital of the molecule into the metallic conduction band. The magnitude of the chemical enhancement has been estimated to reach not more than factors of 10-100.

The electromagnetic enhancement, which has been treated thoroughly in the literature, arises from the enhanced local optical fields at the position of the molecule adjacent to the metal surface. A laser beam incident on a rough metal surface will introduce a collective excitation of conduction electrons in the sub-wavelength size metallic structures. In other words, localized resonant surface plasmons [35, 36] can be generated in metallic nanostructures, and therefore, the evanescent electric fields in the vicinity of these structures have an intensity that is larger than that of the incident field by several orders of magnitude. The greatest enhancements are observed with silver, gold, and copper whose grain diameter ranges between 10 and 200 nm and whose plasmon resonance energy is at visible wavelengths.

In an analogous fashion to the laser excitation field, the Raman scattered field (Stokes or anti-Stokes) will also be enhanced by the surface plasmon generating mechanism. Taking into account contributions both from the laser excitation field enhancement and from the Raman scattered field enhancement, the electromagnetic enhancement factor for the Raman scattering can be written as

$$G_{Stokes} = \frac{P_{SERS}}{P_{NRS}} = |A(\nu_0)|^2 \cdot |A(\nu_0 - \nu_1)|^2 \quad (3.18)$$

and

$$G_{anti-Stokes} = \frac{P_{SERS}}{P_{NRS}} = |A(\nu_0)|^2 \cdot |A(\nu_0 + \nu_1)|^2 \quad (3.19)$$

where  $P_{SERS}$  is the optical power of surface enhanced Raman scattering,  $P_{NRS}$  is the optical power of normal Raman scattering (without surface enhancement), and  $A(\nu)$  is the electromagnetic field enhancement factor at optical frequency  $\nu$ . These two formulas

show that the surface enhancement of Raman scattering scales as the fourth power of the local field enhancement factor of the metallic nanostructure.

For understanding the concept of electromagnetic SERS enhancement, the metallic nanostructure can be simplified [38] as a small sphere with a complex dielectric constant  $\varepsilon(\nu)$  in a surrounding medium with a dielectric constant  $\varepsilon_0$ . As shown in Fig. 3-4, the radius of the sphere  $r$  is small compared with the excitation wavelength.

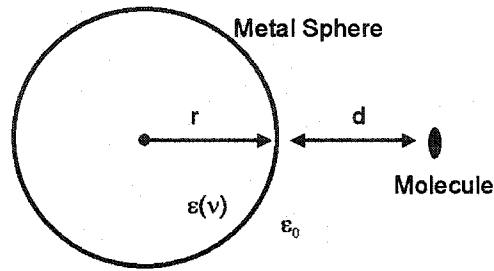


**Figure 3-4: Metal nanosphere**

A molecule at a distance  $d$  from the metal sphere surface is exposed to a field  $E_M$ , which is the superposition of the incoming field  $E_0$  and the field of a dipole  $E_{SP}$  induced in the metal sphere. The field enhancement factor  $A(\nu)$  is given by

$$A(\nu) = \frac{E_M(\nu)}{E_0(\nu)} = \frac{E_0(\nu) + E_{SP}(\nu)}{E_0(\nu)} = \frac{E_{SP}(\nu)}{E_0(\nu)} = \frac{r^3}{(r+d)^3} \cdot \frac{\varepsilon(\nu) - \varepsilon_0}{\varepsilon(\nu) + 2\varepsilon_0} \quad (3.20)$$

From Eq. 3.20, one can find that  $A(\nu)$  is particularly strong when the real part of  $\varepsilon(\nu)$  is equal to  $-2\varepsilon_0$ . Additionally, for a strong electromagnetic enhancement, the imaginary part of the dielectric constant needs to be small. These conditions describe the resonant excitation of surface plasmons of the metal sphere. When excitation and scattered fields are in resonance with the surface plasmons, the enhancement of Raman

scattering is particularly strong. This is automatically the case for low-frequency Raman modes and explains why scattering efficiencies of different Raman bands in a spectrum fall off with increasing vibrational energy.

Electromagnetic SERS enhancement does not require direct contact between a molecule and a metal. However, it will strongly decrease with the growing distance between the molecule and metal surface. This effect is due to the decay of the field of a dipole over the distance, which is described by the  $r^3/(r+d)^3$  term in the equation of field enhancement factor  $A(\nu)$ . Since the enhancement factor of the SERS effect is proportional to the fourth power of the field enhancement factor  $A(\nu)$ , its decay with the distance results in

$$G \propto \frac{r^{12}}{(r+d)^{12}}. \quad (3.21)$$

When  $d = 0.18 r$ ,  $r^{12}/(r+d)^{12} \sim 1/e^2$ . Therefore, SERS effect exist only in a short range of  $0.18 r$ .

### **3.2.2 Theoretical calculation of field enhancement by the orderly patterned aperture structure in a gold film**

An orderly patterned aperture structure in a gold film will have similar enhancement properties, where the Raman enhancement derives from the highly localized electric fields in the vicinity of each aperture [51]. The model presented here is an idealization of the fields around actual patterned apertures, in that it neglects the finite conductivity of the metal film and the cooperative nature of the localized surface plasmon excitation

among the individual apertures [52, 53]. Nevertheless, the modeling results are expected to yield field patterns similar to those of realistic metals [1].

Consider a plane-parallel,  $x$ -polarized, monochromatic optical beam with  $\lambda = 500 \text{ nm}$  propagating in the  $z$  direction. Let the beam be incident normally on a circular aperture fabricated in an infinitely thin, perfectly conducting metal film. The scattered electric and magnetic fields at a distance  $z$  away from the surface of the aperture, where  $0 < z < \lambda/10$ , were calculated by Bethe and corrected by Bouwkamp [54, 55]. Bouwkamp, in his derivation, used an oblate-spheroidal coordinate system defined by

$$x = a\sqrt{(1-u^2)(1+v^2)} \cdot \cos(\phi) \quad (3.22)$$

$$y = a\sqrt{(1-u^2)(1+v^2)} \cdot \sin(\phi) \quad (3.23)$$

and 
$$z = a \cdot u \cdot v. \quad (3.24)$$

According to Bouwkamp, the  $x$ ,  $y$ , and  $z$  components of the scattered electric fields,  $E_x$ ,  $E_y$  and  $E_z$  respectively are given by

$$E_x = k \cdot z - \frac{2}{\pi} k \cdot a \cdot u (v \cdot \tan^{-1}(v) + \frac{x^2 - y^2}{3a^2(u^2 + v^2)(v^2 + 1)^2} + \frac{1}{3(u^2 + v^2)} + 1) \quad (3.25)$$

$$E_y = -\frac{4}{3\pi} \cdot \frac{k \cdot x \cdot y \cdot u}{a(u^2 + v^2)(v^2 + 1)^2} \quad (3.26)$$

and 
$$E_z = \frac{4}{3\pi} \cdot \frac{4k \cdot x \cdot v}{(u^2 + v^2)(v^2 + 1)}. \quad (3.27)$$

The scattered electric fields, in a plane parallel to an aperture with diameter  $\lambda/5$  are shown in Fig. 3-5. Here, one observes that at close proximity,  $E_x$ ,  $E_y$  and  $E_z$  are concentrated around the aperture's circumference. Their distributions differ, however,  $E_x$

is concentrated mostly around  $y=0$ ,  $E_y$  around  $x=y$ , and  $E_z$  around  $x<0$ . Further away from the aperture, the scattered fields decrease in magnitude and grow in diameter,  $E_x$  and  $E_y$  become circular, while  $E_z$  is always anti-symmetric.

The three components of the electric fields diffracted by the aperture are combined into the total  $E_t$ ,

$$E_t = \sqrt{E_x^2 + E_y^2 + E_z^2}. \quad (3.28)$$

The total scattered electric field,  $E_t$ , in a plane parallel to the aperture is shown in the bottom row of Fig. 3-5. Here, one observes that at close proximity,  $E_t$  resembles  $E_x$ , being concentrated around the aperture circumference, and mostly on the left and right hand side. Further away from the aperture, the scattered field decreases, becomes circular and grows in diameter. To connect to a realistic model, the fact has to be recognized that the film is a perfect conductor so that there is no skin depth. Stated differently, the electric fields at the aperture plane terminate abruptly, rather than extending several tens of nanometers away from its circumference. However, at distances of several tens of nanometers away from the plane of the aperture, the electric fields do extend beyond the circumference of the aperture, and as a result represent a more realistic case where the film has a finite conductivity.

Now consider a two-dimensional array of apertures composed of six apertures surrounding a single aperture. Each aperture has a diameter of 100 nm, and the centers of all the apertures are separated by 110 nm. The respective fields scattered by a single aperture can be combined to form an overall image of the field scattered from such a

structure, dubbed a Flower. Figure 3-6 shows the scattered fields that exhibit a rich pattern both in intensity and in phase. Such a “flower structure” can serve as a useful tool to field-enhance Raman scattering from a thin organic film that is deposited on top of it.

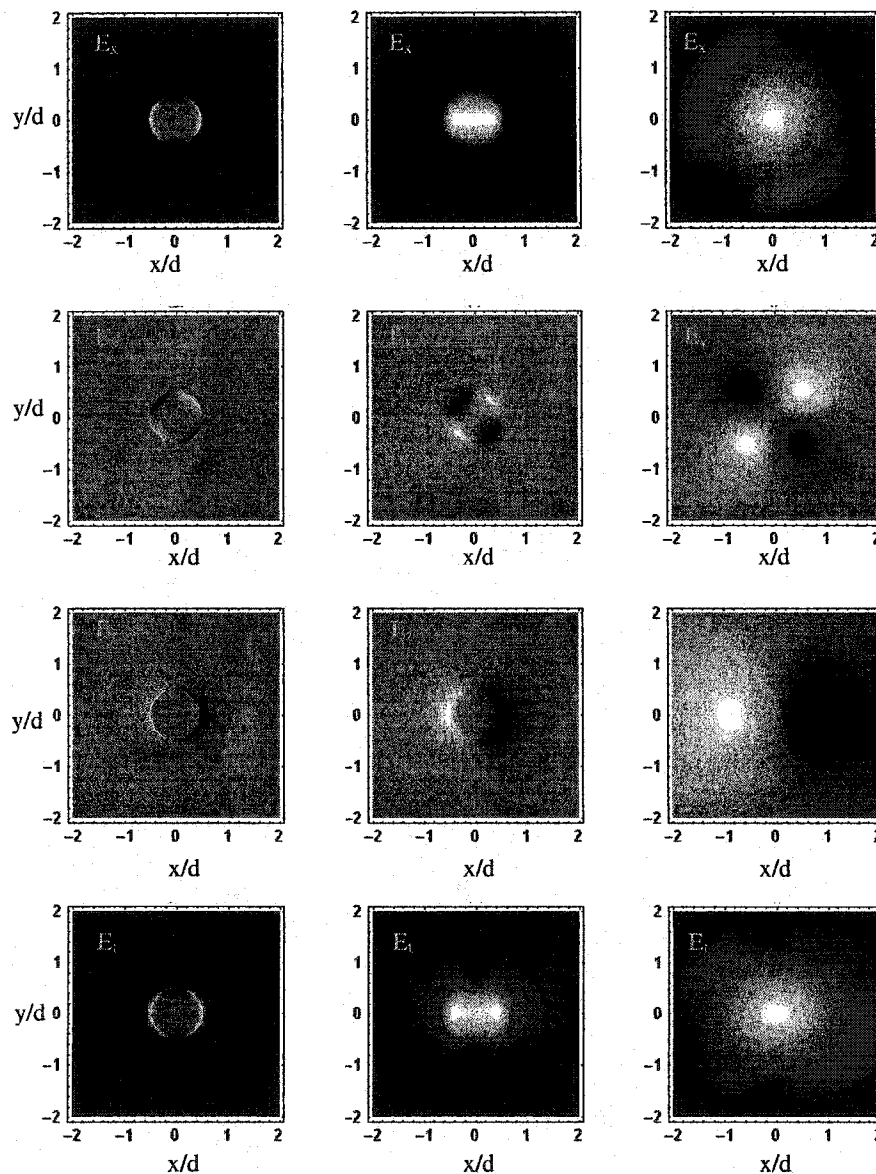


**Figure 3-5: Scattered electric fields  $E_x$ ,  $E_y$ ,  $E_z$  and  $E_t$  in a plane parallel to the aperture, at (a)  $z = 1$  nm, (b)  $z = 10$  nm and (c)  $z = 100$  nm [56]**



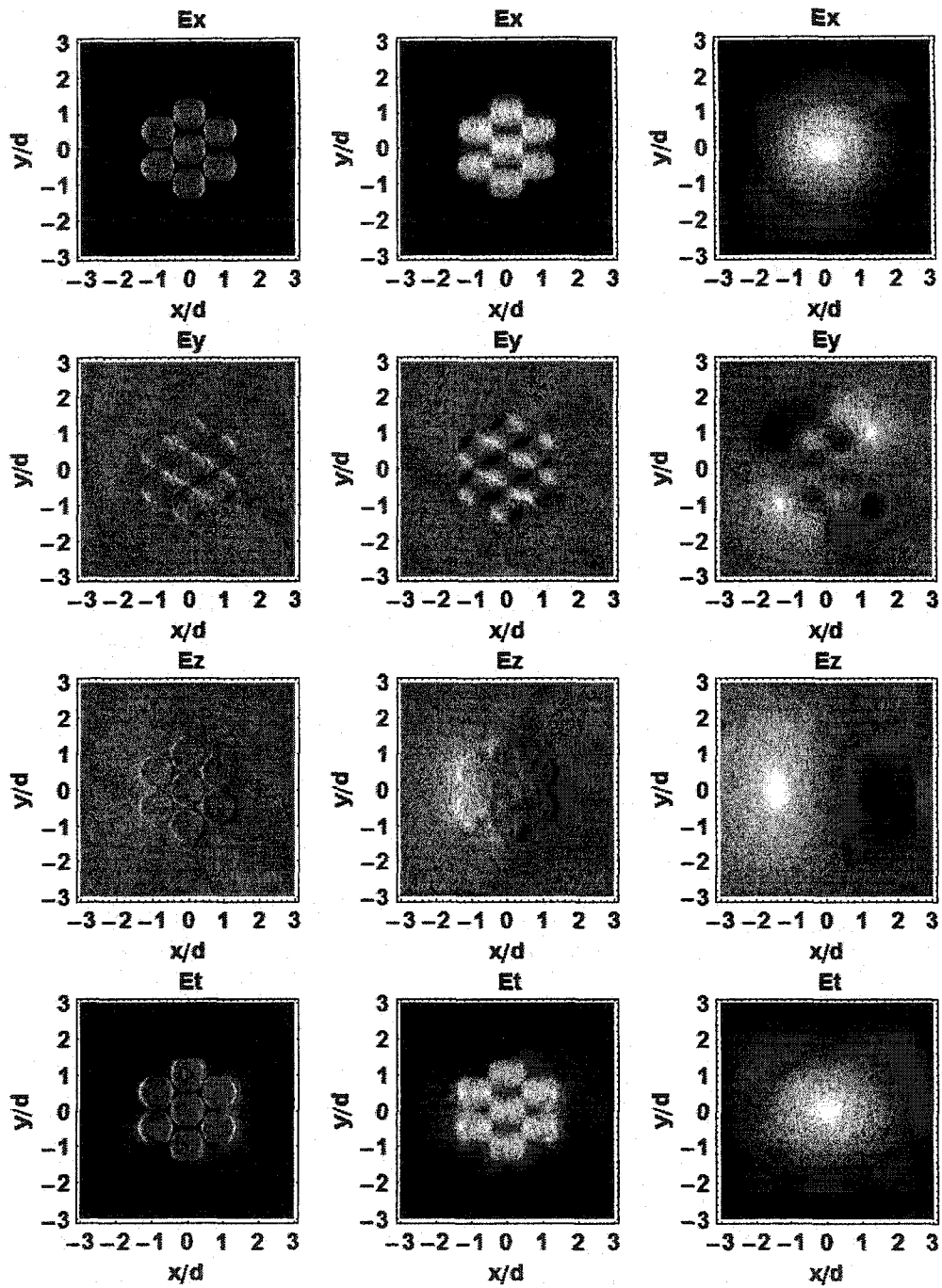
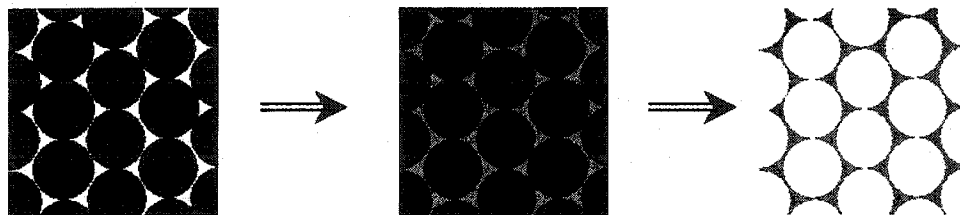


Figure 3-6: Scattered electric fields  $E_x$ ,  $E_y$ ,  $E_z$  and  $E_t$  in a plane parallel to the

Flower, at (a)  $z = 1$  nm, (b)  $z = 10$  nm and (c)  $z = 100$  nm [56]

### 3.2.3 Experiments and results on flower structure



**Figure 3-7: Method of fabricating flower structure**

Figure 3-7 describes the method of fabricating the “flower structure”. Here, a solution containing latex spheres (*diameter* ~ 500 nm, Polysciences, Inc.) was drop-cast onto a glass cover slip and allowed to dry in air. The close-packed spheres formed a shadow mask on the glass cover slip [57, 58]. Next, a thin layer of silver (40 nm) was evaporated onto the sample. Then, the latex spheres were subsequently removed by dissolving them in toluene, leaving behind a structured film. The film was then rinsed thoroughly with methanol and blown dry in nitrogen.

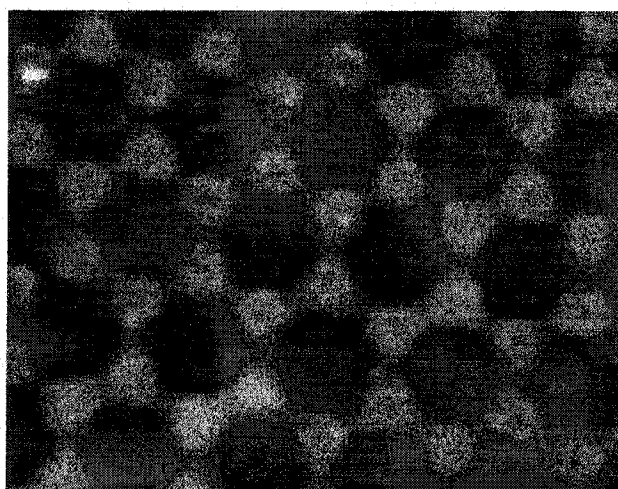


**Figure 3-8: An AFM topography image of flower structure [56]**

Figure 3-8 shows an AFM topography image of the flower structured silver film on glass cover slip. A  $\beta$ -carotene sample was spin coated on this substrate. A spectrum analysis reveals that Raman scattering is significantly enhanced by the flower structure. The enhancement effect produces a high signal-to-noise ratio spectrum as shown in Fig. 3-9. When the  $\beta$ -carotene sample was spin coated on glass cover slip, without structured silver film, the Raman scattering was undetectable using the same detector accumulation time.

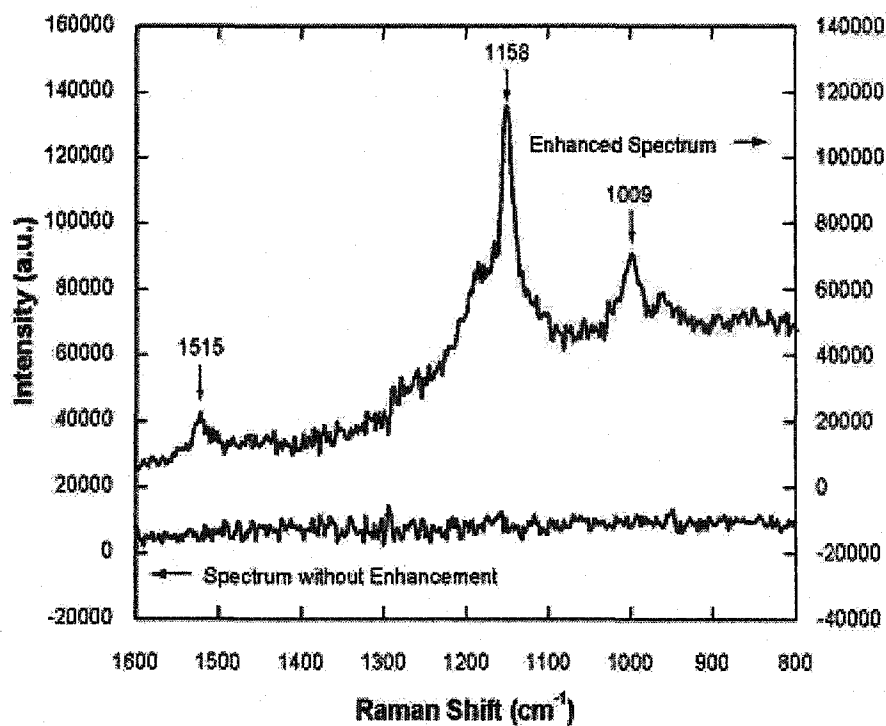
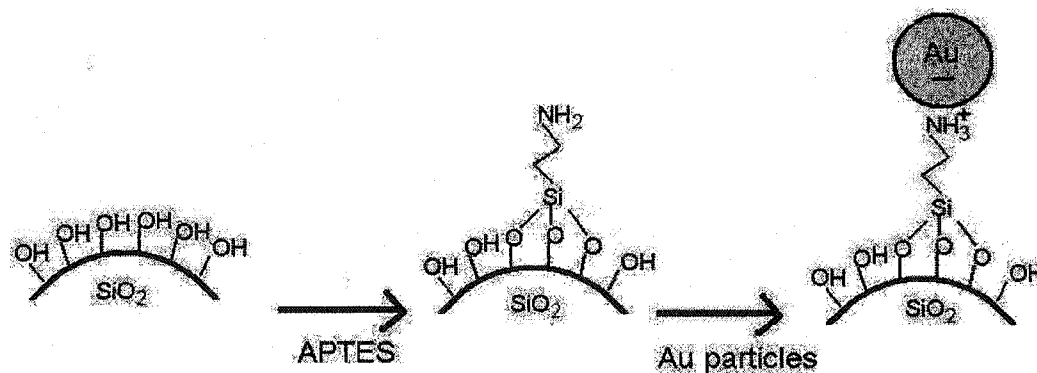


Figure 3-9: SERS effect of flowers structure [56]

### 3.2.4 Experiment and results on Au monolayer

A self-assembled monolayer of gold particles on the oxide layer of a silicon wafer can also be used as the SERS active substrate[59]. The fabrication method of this substrate is depicted in Fig. 3-10. First, the silicon substrate was immersed for 2 hours in 50 ml of 0.2% 3-Aminopropyltriethoxysilane (APTES) solution in methanol. The immersion was performed in a nitrogen atmosphere. After the deposition of the APTES monolayer, the silicon substrate was then rinsed thoroughly with methanol and blown dry in nitrogen. Subsequently, colloidal gold particles (60 nm) were deposited from their aqueous solution after which the substrate was rinsed and blown dry in nitrogen and imaged by contact mode AFM.



**Figure 3-10: Method of coating Au particles onto a glass cover slip**

Figure 3-11 shows an AFM topography image of self-assembled Au particles on the oxide layer of a silicon substrate. A  $\beta$ -carotene film was spin coated on this substrate. A spectrum analysis clearly demonstrates a SERS effect of gold particles in comparison to a conventional Raman spectrum of  $\beta$ -carotene film spin-coated on silicon, as shown in Fig. 3-12.

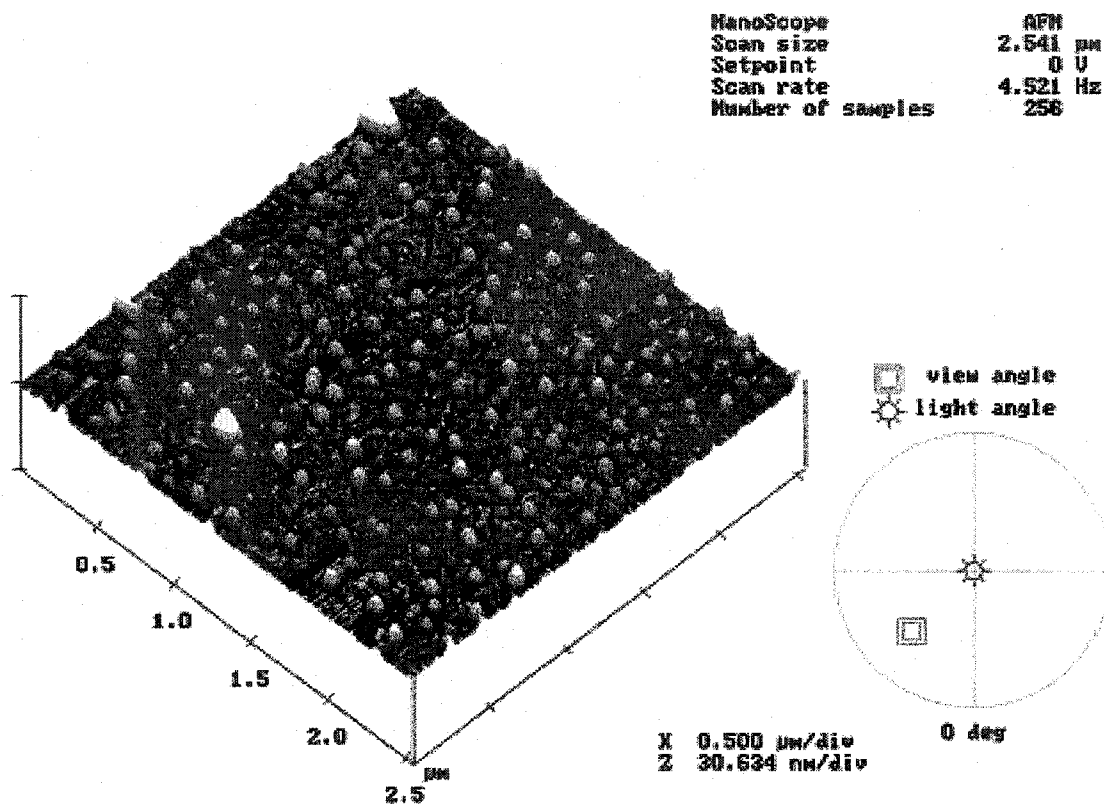
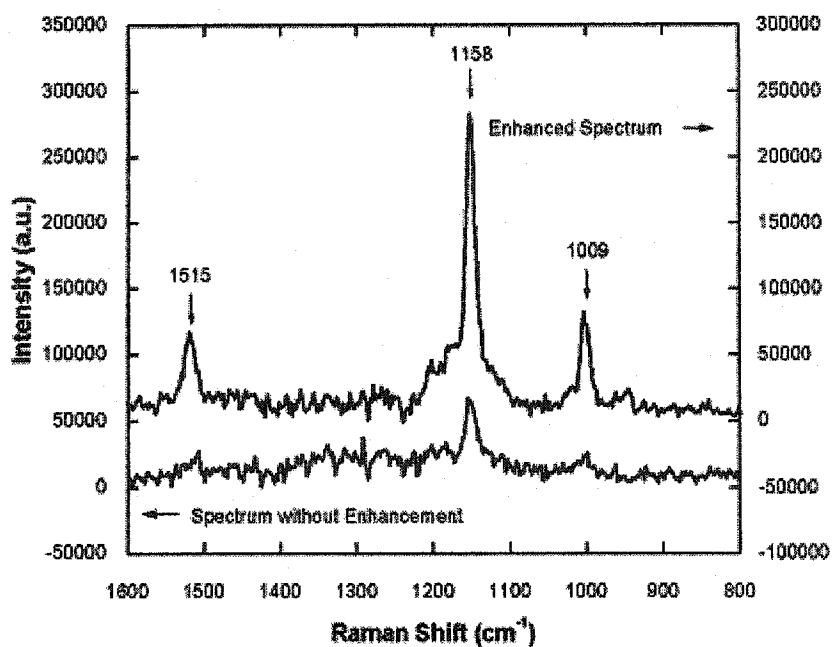


Figure 3-11: An AFM topography image of monolayer of Au particles [56]



**Figure 3-12: SERS of  $\beta$ -carotene sample on the Au particle monolayer [56]**

The previous theoretical analysis reveals that the enhancement effect only exists around the flower structure's circumference or in the vicinity of gold particles. Therefore, for both the flower structured silver film and the self-assembled Au particles, the enhancement factor can hardly be estimated because the area of the locally enhanced film is not known.

### 3.3 Combination of AFM and Raman Scattering

Ever since the invention of Scanning Probe Microscopy (SPM), there has been a considerable effort to integrate optical spectroscopy analysis into the SPM ability to image at high spatial resolution [60-66]. Among these efforts, near-field fluorescent microscopy has been thoroughly investigated as a tool to observe the molecular distribution of a sample. Fluorescent imaging of single molecules using a near-field scanning optical microscope (NSOM) was first reported by Betzig [64], and the dynamics of fluorescent molecules was studied by Xie and Dunn [65], and by Ambrose *et al.* [66].

However, The important challenge facing analytical chemistry is not only detecting trace amounts of substances, but also identifying their chemical structure. The amount of molecular structural information that can be obtained from the broad fluorescence bands is very limited, particularly at room temperature. Raman spectroscopy, in comparison, provides precise information on the vibrational modes of a molecule. But the cross-section of Raman scattering is extremely low (typically  $10^{-30}$  cm<sup>2</sup>), much lower than that of infrared absorption of molecular vibration (typically  $10^{-20}$  cm<sup>2</sup>). For a nanometer-scale size of sample, Raman shift peaks could be too small to distinguish from the broadband peak of fluorescence whose cross-section can be as large as  $10^{-16}$  cm<sup>2</sup>. As a result, it is extremely difficult to perform spatially resolved Raman scattering by NSOM, because such methods have a low throughput and need very long integration times.

The large enhancement factor [46-48] of the SERS effect showed promise in overcoming the low cross-section problems inherent in high resolution Raman microscopy, and the short range of the SERS effect provides the potential for nanometer

scale spatial resolution of Raman spectroscopy. It was recently demonstrated [37, 39, 40, 67, 68] that a conventional AFM tip, suitably coated with a rough gold or silver film, could provide spatially selective SERS. The laser photons are absorbed by the nanostructures of the rough metallic coating on the tip surface via oscillations of surface electron charge-density waves (surface plasmons). This excitation can couple with the molecules that are in close proximity to the tip, providing an efficient pathway to transfer energy to the molecular vibrational modes and so generate Raman photons. This enhancement is maximized through local concentration of the incident radiation field when (a) the excitation energy is close to the plasmon resonance of the metallic tip, (b) the metal grains are smaller than the incident laser wavelength and (c) the analyzed molecules have the appropriate Raman selection criteria to couple to the plasmon field.

It is useful to obtain a theoretical framework to predict electromagnetic field enhancements,  $E_{tip}$ , of a metallic AFM tip. For an isolated, well-shaped particle, such as a spheroid, assuming a bulk dielectric function, a simple analytical solution yields [69, 70]

$$E_{tip} = \frac{\varepsilon}{1 + (\varepsilon - 1)A} \quad (3.29)$$

where  $A = \frac{a \cdot b^2}{2} \int_0^\infty \frac{1}{(a^2 + \xi^2)^{3/2} (b^2 + \xi^2)} d\xi$ ,  $a$  and  $b$  are the long and short radius of the spheroid, respectively.

The solution has been applied to an external illumination of a probe tip by a laser, producing an intensity enhancement of five orders of magnitude in the near field underneath the tip. Figure 3-13 shows the calculated field enhancement,  $E_{tip}$ , of a silver prolate spheroid, simulating an AFM tip as a function of the illuminating light wavelength



for a spherical tip ( $b = a$ , resonant peak at 400 nm) and an elongated tip ( $b \ll a$ , resonant peak at 600 nm).

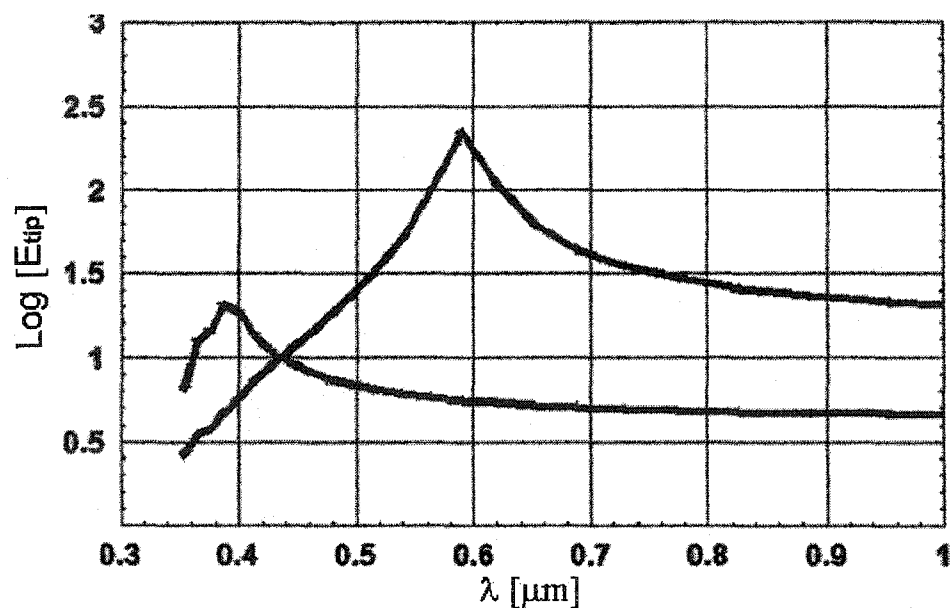


**Figure 3-13: Field enhancement factor of a silver AFM tip [56]**

Several groups are currently engaged in research of tip enhanced Raman scattering, including Mark S. Anderson [37, 67, 68] at JPL, Norihiko Hayazawa [39] at Osaka University, Linda T. Nieman at the University of Texas (Austin), and Nie Shuming [40] at Indiana University. Sputtering, deposition of colloidal particles, self-assembled particle arrays, and alloying of intermetallics have all been investigated as potential techniques for realizing the surface enhancement, and factors of  $10^3 \sim 10^5$ , and 50 nm size Raman sensing was claimed.

These feasibility studies have led us to build a Raman-AFM (RAFM) experimental configuration that can combine the analytical power of Raman spectroscopy with the nanometer resolution of atomic force microscopy (AFM). The development of the RAFM

system depends on harnessing the complex interaction between the laser beam for Raman excitation, the metallic AFM tip and the underlying sample surface. In the following sections, the combination of the optical system, the Raman spectrometer, and the AFM with metallic tip to realize tip enhanced Raman scattering will be discussed.

### 3.4 Optics of Probing a Local Raman Scattering Signal

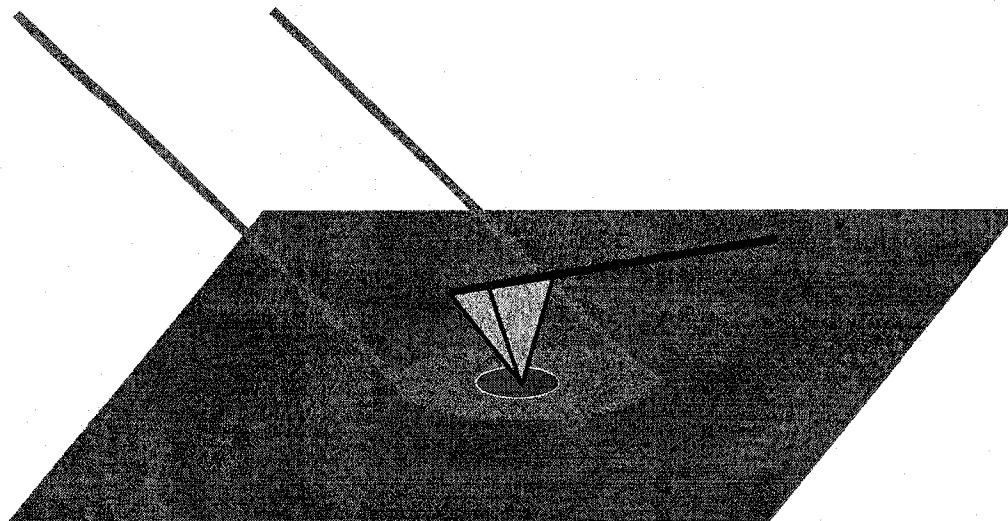


**Figure 3-14: NRS-SERS contrast**

In the RAFM system, Normal Raman Scattering (NRS) photons are generated from the whole illuminated area while focusing the laser beam on the sample, as shown in Fig. 3-14. On the other hand, Surface Enhanced Raman Scattering (SERS) photons originate only from the vicinity of the tip. Both NR photons and SERS photons contribute to the total Raman signal collected and detected by the Raman spectroscopy system, but unfortunately, only the SERS photons contain the local material information of interest. Therefore, a good contrast between SERS and NRS is required for probing local Raman signal in nanometer scale.

Given the fixed value of tip enhancement factor, the NRS-SERS contrast in the RAFM system is determined by the ratio between the tip-enhanced area and the laser-illuminated area. In conclusion, one must obtain a small illumination focus spot size while utilizing RAFM to probe local material information.

### 3.4.1 A brief look at the concept of NA and DOF

The minimum size of the focus spot that one can expect from aberration-free lenses is limited by the diffraction effect resulting from the focusing system's finite aperture. One method of defining this finite aperture is by the Numerical Aperture ( $NA$ ), which is the refraction index (of the medium in which the focus spot lies) times the sine of the half angle of the cone of illumination [71], as sketched in Fig. 3-15.

$$NA = n \cdot \sin\theta \quad (3.30)$$

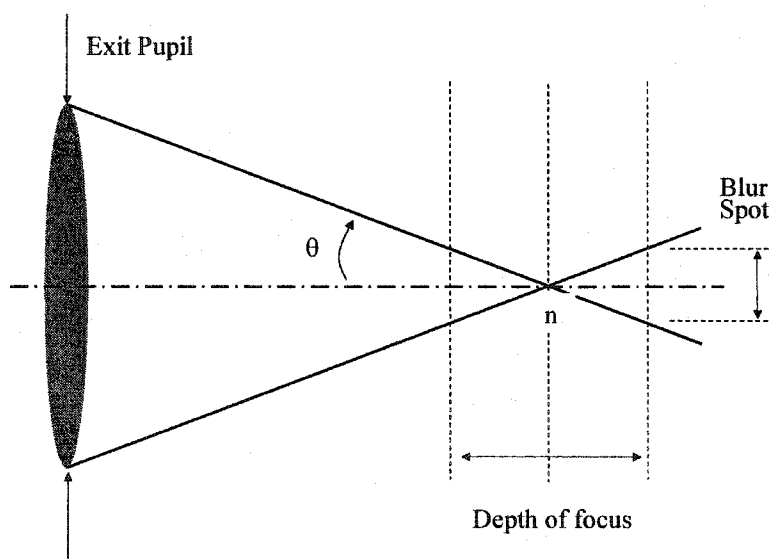


**Figure 3-15: Numerical aperture and depth of focus**

When an optical focusing system is defocused (eg: In the RAFM system, the sample may be shifted longitudinally with respect to the plane of perfect focus.), the illuminated area becomes a blurred spot whose size is determined by the  $NA$  and the length of shift. Assume there exists a blur of small enough size (eg: Rayleigh Criterion or Sparrow's Criterion) such that it will not adversely affect the performance of the system. The depth of focus ( $DOF$ ) is defined as the range of distance along the optical axis in which the

object may be shifted before the acceptable blur size  $B$  is produced. Thus, in using a geometric optics approximation, the value of  $DOF$  is given by

$$DOF = B / \sin\theta. \quad (3.31)$$

### 3.4.2 Diffraction limit of the focus spot size

Figure 3-16 shows a focus spot's transverse intensity distribution, which consists of a bright central spot of light surrounded by concentric rings of rapidly decreasing intensity. This distribution, known as an Airy pattern [72], originates from the diffraction effect of the focusing lens' finite circular aperture when a uniform-amplitude plane wavefront is incident on an aberration-free lens.

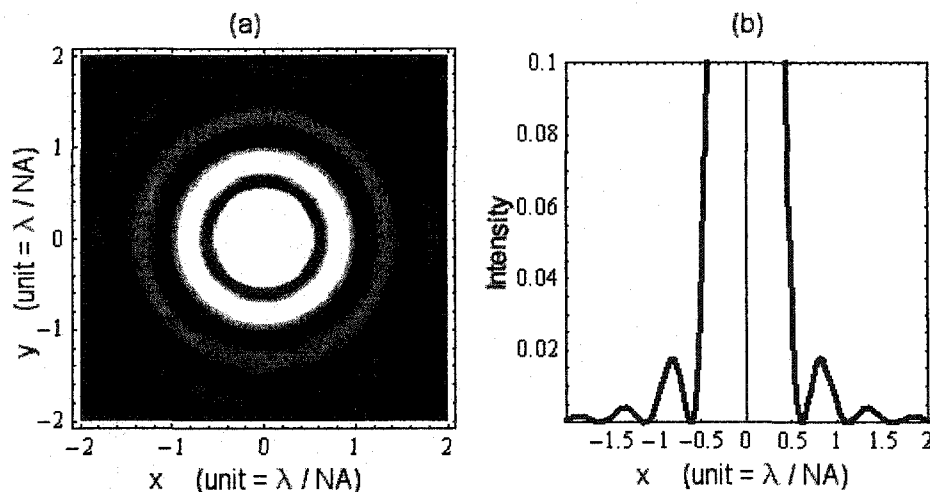


**Figure 3-16: Airy pattern**

84% of the energy is contained in the bright central spot of the pattern, which is called the Airy disk. Its diameter is given by

$$d_{Airy} = 1.22\lambda / NA \quad (3.32)$$

where  $\lambda$  is the wavelength of the light in air, and  $NA$  is the numerical aperture of the focusing lens. The Airy disk diameter played an important role in estimating the diffraction limit of the focus spot size. If it is used as the acceptable blur size while defocusing the optical system, then the depth of focus can be determined by

$$DOF = \frac{1.22\lambda / NA}{NA} = 1.22 \frac{\lambda}{NA^2}. \quad (3.33)$$

Another popular criterion of diffraction limit is defined by the Airy disk's FWHM (known as Sparrow's criterion for resolution of an optical system).

$$d_{FWHM} = 0.51\lambda / NA \quad (3.34)$$

Only 47% of the total energy is contained within the FWHM. Often, a pinhole is used to clean up the dark rings around the Airy disk. Therefore, the intensity distribution of the bright central spot can be approximated as a Gaussian distribution. 77% of the total energy is contained within the full-width at  $1/e^2$  of the maximum

$$d_{1/e^2} = 0.82\lambda / NA \quad (3.35)$$

In many cases, the laser beam to be focused in the RAFM system should be described as a Gaussian beam rather than a uniform-amplitude plane wave [73]. The Gaussian beam has different properties compared to classical light, particularly regarding propagation, focusing and collimation. Detailed discussion of these properties can be found in Appendix A of this dissertation. Here, we only deal with the diffraction limit of the focus spot size and the *DOF*. Since a Gaussian source distribution remains Gaussian at every point along its path of propagation through the optical system, the transverse distribution of the intensity at focus spot can be represented as

$$I[r] = I_0 \cdot \exp\left[-2\frac{r^2}{w_0^2}\right] \quad (3.36)$$

where  $w_0$ , usually called the Gaussian beam radius, is the radius at which the intensity has decreased to  $1/e^2$  of its axial value. This distribution is shown in Fig. 3-17.

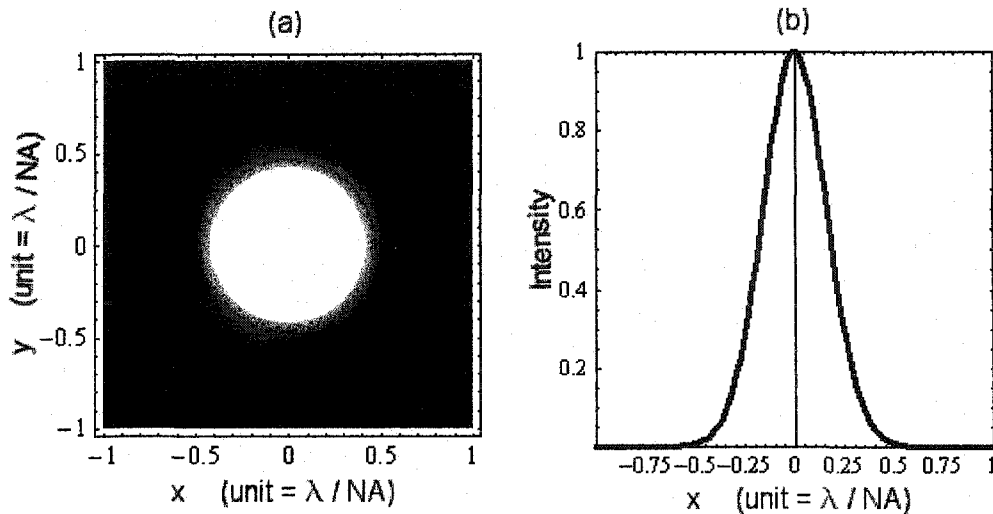


**Figure 3-17: Gaussian beam focus**

86% of the total energy distributed is contained within the Gaussian beam radius.

Thus, the focus spot size can be defined as

$$d_{1/e^2} = 2w_0 = \frac{2}{\pi} \cdot \frac{\lambda}{NA} = 0.64\lambda / NA. \quad (3.37)$$

Another point to note is the FWHM of the Gaussian distribution, which is given by

$$d_{FWHM} = 0.38\lambda / NA. \quad (3.38)$$

50% of the power is contained within the FWHM of focused Gaussian beam.

If  $\sqrt{2} \cdot w_0$  (somewhat arbitrarily) is defined as the acceptable blur size while defocusing, then the *DOF* of the optical system is

$$DOF = \frac{2}{\pi} \cdot \frac{\lambda}{NA^2} \quad (3.39)$$

Using these relations, one can make simple calculations for optical focusing lenses in a RAFM system employing Gaussian beam or uniform-amplitude plane wave as the incident beam. For example, if a  $NA=0.8$  microscope objective lens is used, the parameters of the focus will be

Incident Beam	$\lambda$	$d_{Airy}$	$d_{FWHM}$	$d_{1/e^2}$	$DOF$
Uniform-Intensity Plane Wave	532 nm	811 nm	342 nm	546	1014 nm
	780 nm	1190 nm	501 nm	801	1487 nm
Gaussian Beam	532 nm		250 nm	423 nm	529 nm
	780 nm		367 nm	621 nm	775 nm

**Table 3-1: Parameters of the focus**

### 3.4.3 Collection efficiency

When the excitation laser beam is focused on the sample by a high  $NA$  lens, the distribution of the laser intensity on or through the sample determines which molecules will produce Raman scattered light. In some of the Raman spectroscopy system, the diameter of the excitation laser beam focus spot is comparable to  $t$ , the illuminated thickness of the sample ( $t = DOF \sim \lambda/NA^2$  in case of liquid sample). Therefore, the Raman signal can be considered approximately as radiation from a point source. Since the angular dependence of the Raman scattering intensity is more or less isotropic, the Raman photon collection efficiency of the sample interface can be described by the fraction of the  $4\pi$  steradian solid angle surrounding the sample that is intercepted by the



collection optics. The relationship between the solid angle of collection and the numerical aperture is  $\Omega = 2\pi(1 - \sqrt{1 - NA^2})$ . Thus, the collection efficiency of Raman scattering,  $\eta$  is given by

$$\eta = 0.5(1 - \sqrt{1 - NA^2}). \quad (3.40)$$

In the RAFM system, the Raman signal cannot be considered as emanating from a point source because the thickness of the thin film sample is much smaller than the laser beam focus spot size. However, this thin slab radiation source can be approximated as a Lambertian source. The Raman collection efficiency is determined by the projection of the collection solid angle on the plane of the thin slab, which is given by  $\bar{\Omega} = \pi \cdot NA^2$ . Thus, the Raman collection efficiency for a thin film sample can be represented as

$$\eta = 0.5NA^2. \quad (3.41)$$

The efficiency of both models is plotted in Fig. 3-18. The maximum collection efficiency of the RAFM system is 0.5 since the maximum collection solid angle that one can achieve by using a microscope objective lens is  $2\pi$ . If the thickness of the thin film sample is only slightly smaller than the laser beam focus spot size, the illuminated volume of the sample is neither a point source nor Lambertian and the collection efficiency of the Raman signal will be some value between the two curves in Fig. 3-18.

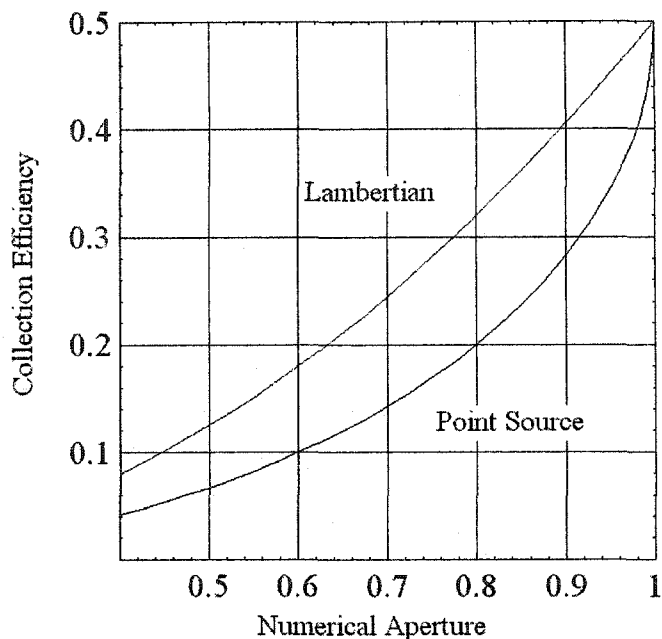


**Figure 3-18: Collection efficiency of Raman photons with NA of the optics**

#### 3.4.4 Solid Immersion Lens (SIL)

From the previous discussion, one can conclude that the contrast of a Raman-AFM system is determined by the numerical aperture of the focusing optics. A high  $NA$  lens must be used while probing nanometer scale material information with the RAFM system. Since  $NA = n \cdot \sin\theta$ , the maximum  $NA$  of a “dry” objective lens is 1.00 in air, corresponding to an ideal 90-degree half angle of the cone of illumination. In practice, the commercially available highest  $NA$  is only 0.95. One method to get a  $NA$  greater than 1.00 is to use an Oil Immersion Lens (OIL), which is designed to operate with an immersion medium between the front lens and the specimen. The  $NA$  of commercially available OILs can be as high as 1.44 using  $n = 1.5$  immersion oil. However, if an OIL were used in the RAFM experiment, the immersion oil could introduce unwanted

fluorescence and Raman scattered light. To avoid the contamination and noise from the OIL, Solid Immersion Lenses (SIL) was employed to improve the laser focus spot size.

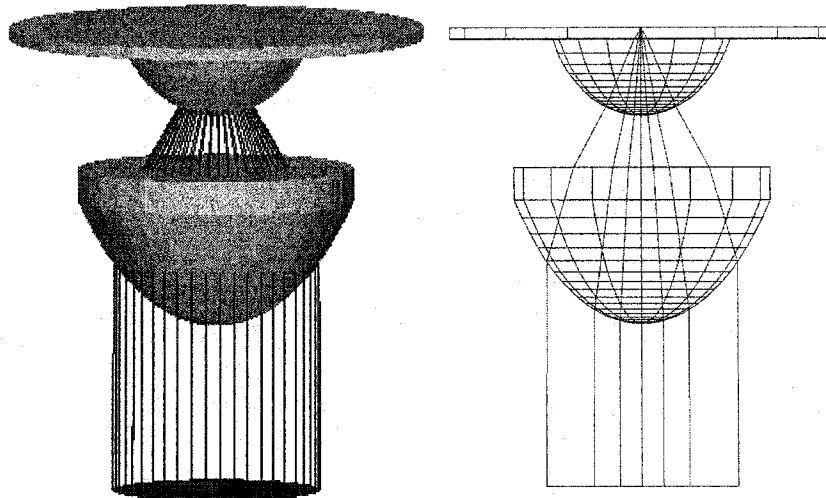


**Figure 3-19: Solid immersion lens system**

The SIL was first proposed in 1990 by Mansfield and Kino for use in high-resolution microscopy [74]. It is a perfect hemisphere made out of high index glass or other materials. The SIL is incorporated with a microscope objective, as shown in Fig. 3-19. By placing the curvature center of the hemisphere exactly at the focus spot of the objective, the rays that focus on the optical axis will pass unrefracted into the lens and continue to focus directly on the flat surface of the SIL. In other words, the converging light rays enter the SIL at normal incidence and is focused inside the SIL without any refraction effect. If the numerical aperture of the objective lens in air is  $NA = \sin\theta$ , the effective numerical aperture with the SIL becomes  $NA = n \cdot \sin\theta$  due to the  $n$ -times shorter wavelength propagating in the high-index SIL material, where  $n$  is the refractive index of

the SIL and  $\theta$  is the marginal ray angle. Therefore, the diffraction-limited focus spot size is reduced by a factor of  $n$  by incorporating the microscope objective with a SIL.

In the RAFM system, the SIL is made out of LASFN-9 glass, having  $n=1.8$  at  $\lambda=532 \text{ nm}$ . The NA of the microscope objective lens (1-UM354, Olympus) is  $\sin\theta=0.8$  in air. Thus, the effective NA with the SIL is given by

$$NA = n \cdot \sin\theta = 1.8 \times 0.8 = 1.44 \quad (3.42)$$

### 3.4.5 Optical field study of the SIL

When the equivalent NA is larger than one, evanescent waves and depolarization effects are involved in the optical focusing process. Diffraction theory based on scalar wave optics may not be appropriate to describe these phenomena. Therefore, the electromagnetic focusing theory of Richards & Wolf was employed to analyze the optical field distribution associated with the SIL [75, 76]. The Point Spread Function (PSF) of an SIL lens illuminated by an  $x$ -polarized beam is given by

$$\begin{pmatrix} E_x(r, \phi, z) \\ E_y(r, \phi, z) \\ E_z(r, \phi, z) \end{pmatrix} = \begin{pmatrix} -i(I_0 + I_2 \cos 2\phi) \\ -iI_2 \sin 2\phi \\ -2I_1 \cos \phi \end{pmatrix} \quad (3.43)$$

where

$$\begin{aligned} I_0(r, z) &= \int_0^\alpha \sqrt{\cos\theta} \cdot \sin\theta \cdot (1 + \cos\theta) \cdot J_0\left(\frac{2\pi}{\lambda} n \cdot r \cdot \sin\theta\right) \cdot e^{i\frac{2\pi}{\lambda} n \cdot z \cdot \cos\theta} d\theta \\ I_1(r, z) &= \int_0^\alpha \sqrt{\cos\theta} \cdot \sin^2\theta \cdot J_1\left(\frac{2\pi}{\lambda} n \cdot r \cdot \sin\theta\right) \cdot e^{i\frac{2\pi}{\lambda} n \cdot z \cdot \cos\theta} d\theta \\ I_2(r, z) &= \int_0^\alpha \sqrt{\cos\theta} \cdot \sin\theta \cdot (1 - \cos\theta) \cdot J_2\left(\frac{2\pi}{\lambda} n \cdot r \cdot \sin\theta\right) \cdot e^{i\frac{2\pi}{\lambda} n \cdot z \cdot \cos\theta} d\theta \end{aligned} \quad (3.44)$$

The optic axis is taken to be along  $z$ ;  $(r, \phi, z)$  are the cylindrical coordinates of the observation point;  $\lambda = 532 \text{ nm}$  is the wavelength of the incident light;  $n = 1.8$  is the refractive index of the SIL medium;  $\alpha$  is the angle that the radius of the input pupil makes with the optic axis as viewed from the focal point;  $\sin\theta = 0.8$ , defined by the  $NA$  of the microscope objective lens (1-UM354, Olympus) that is focusing the light into the SIL;  $J_m$  is the  $m_{th}$ -order Bessel function of the first kind.

The intensity is proportional to the square of the optical field magnitude. The intensity distributions of the field components at the SIL-air interface ( $z = 0$ ) are shown in Figs. 3-20, 3-21, and 3-22.

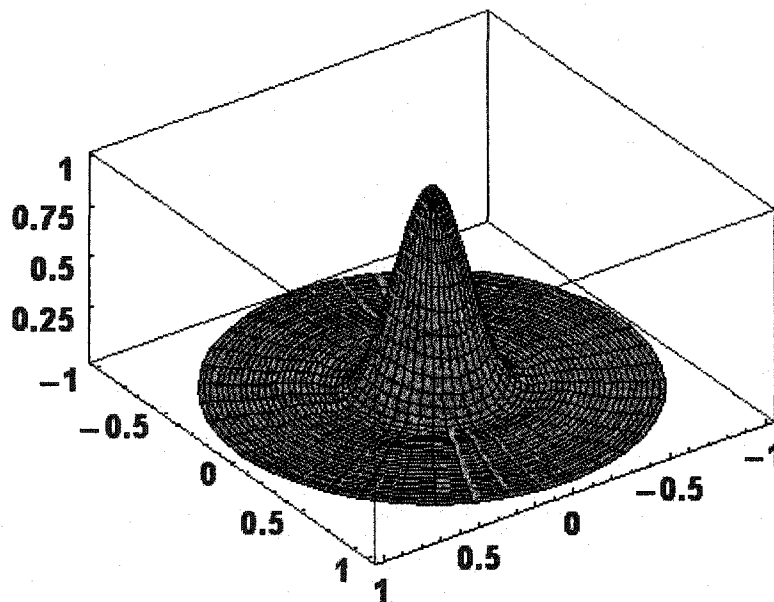


**Figure 3-20: Intensity distribution of the  $x$ -component of the electric field at  $z = 0$**

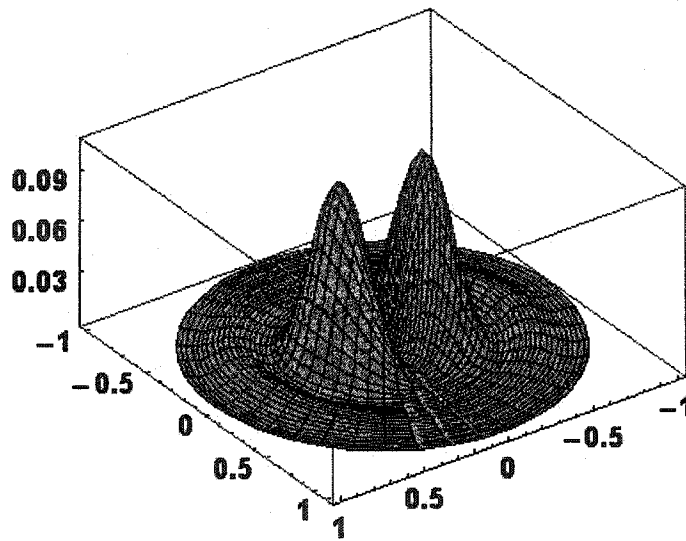


**Figure 3-21: Intensity distribution of the z-component of the electric field at  $z=0$**

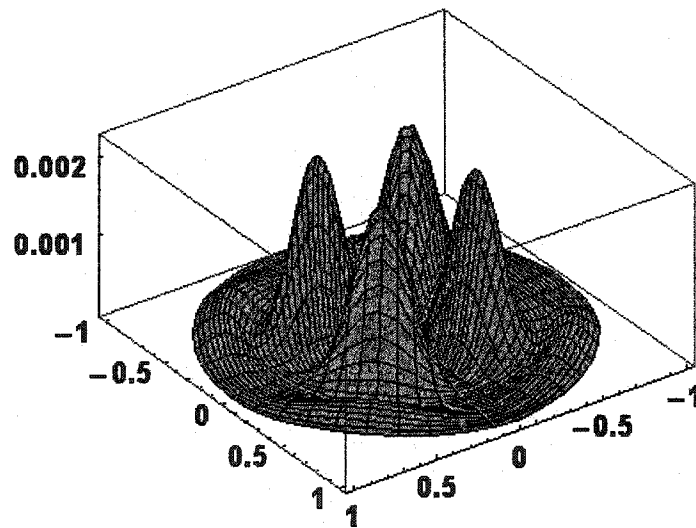


**Figure 3-22: Intensity distribution of the y-component of the electric field at  $z=0$**

Although the  $y$  and the  $z$  components are nonzero, it is evident that the  $x$ -component dominates. The intensity distribution of the  $x$ -component can be approximated by a Gaussian distribution. Most of the energy is contained within the full-width at  $1/e^2$  of the maximum. Using the vector optic theory of Richards & Wolf, the width can be calculated as

$$d_{1/e^2} \sim 0.6\lambda = 320 \text{ nm}. \quad (3.45)$$

One can also use the scalar wave theory to estimate the diffraction limit of the focus spot size when a uniform-amplitude plane wavefront is incident on an aberration-free lens, which is discussed in the previous section (Section 3.4.2). The result is given by

$$d_{1/e^2} = 0.82\lambda / NA = 0.57\lambda = 303 \text{ nm} \quad (3.46)$$

where  $NA = n \cdot \sin\alpha = 1.8 \times 0.8 = 1.44$  is the equivalent numerical aperture of the SIL system. Apparently, the spot sizes calculated from the scalar wave theory and from the vector wave theory are in agreement with each other.

The second largest component is the  $z$ -component, with a peak intensity of 10% of the  $x$ -component. Since most of the Raman enhancement factor is due to surface plasmons generated by the  $z$ -polarized illumination, the  $z$ -component is more interesting to us than in the  $x$ -component. The energy of the  $z$ -component is distributed in two spots, which are confined in a circle with a diameter of  $d_{1/e^2} \sim 0.94\lambda = 500 \text{ nm}$ . The  $y$ -component is much smaller than  $x$  and  $z$  components and is negligible in the experiment.

The previous modeling of the intensity distribution is only correct when the surface of interest is at the SIL-air interface ( $z = 0$ ). In case of  $z > 0$  (the surface of interest is away from the SIL-air interface), one need a further discussion.

Since the equivalent numerical aperture of the SIL is larger than one, both propagating wave and evanescent wave make contributions to the total field in the SIL-air interface. Therefore, a question arises about the decay of the optical intensity and the change of the point spread function when  $z > 0$ . To analyze the optical field distribution in this case, a Fourier optics model developed by Kino *et al.* [77] and Guo *et al.* [76] was employed. This model is based on the use of Richards & Wolf's vector optic theory [75] [76]. The  $z$ -dependence of the Point Spread Function (PSF) has the form:

$$E(r, z) = \frac{w_0^2}{2} \int_0^\infty e^{-w_0^2 k_r^2 / 4} \cdot \frac{2}{1 + \frac{\sqrt{k_2^2 - k_r^2}}{\sqrt{k_1^2 - k_r^2}}} \cdot J_0(k_r r) \cdot e^{i\sqrt{k_2^2 - k_r^2} z} \cdot k_r dk_r \quad (3.47)$$

where  $w_0 = \frac{\lambda}{2NA\sqrt{2\ln 2}}$  is the Gaussian waist when one approximate the  $E_x$  distribution in Fig. 3-20 by a Gaussian distribution with the same FWHM. Here  $k_1 = 2\pi n / \lambda$  and  $k_2 = 2\pi / \lambda$  are the wave numbers in the SIL and air, respectively.

The evolution of the field profile with  $z$  is shown in the Fig. 3-23. The rapid falloff in total field amplitude with distance away from the SIL-air interface is due in part to the rapid decay of the evanescent component as  $z$  increases and in part to the spreading of the profile. When  $z = \lambda/4$ , the peak of the field profile falls 40% and the FWHM increases 40% in comparison to the field profile at  $z = 0$ .



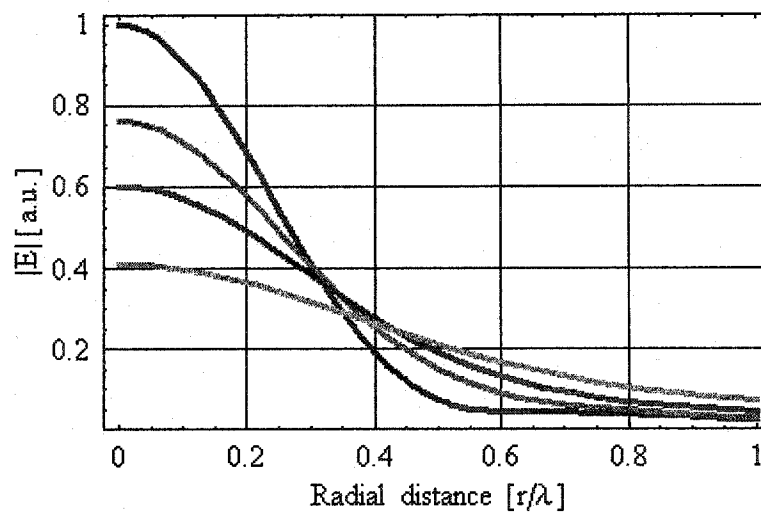


**Figure 3-23: Distribution of the optical field with radius  $r$  at  $z = 0, \lambda/8, \lambda/4,$  and  $\lambda/2$**

In conclusion, for  $\lambda = 532 \text{ nm}$  laser beam incidence, the maximum distance allowed between the surface of interest and the flat surface of SIL must be shorter than  $\lambda/4 \sim 130 \text{ nm}$ . This value can be considered as the depth of focus of the objective-SIL lens group.

#### **3.4.6 A knife-edge test of the focus spot size of the SIL**

To ensure that the SIL system is working properly, the knife-edge test (Foucault test) method was employed to measure the real focus spot size [78]. The sharp tip was broken off from the triangular cantilever of a standard silicon nitride AFM probe and a thin gold film ( $\sim 100 \text{ nm}$ ) was deposited on the tip side of the cantilever to produce a knife-edge with good reflecting surface. After turning off the feedback of the AFM system, the cantilever was mounted on a stand-alone AFM and brought to close contact with the flat surface of the hemispherical lens, as shown in Fig. 3-24.

When a collimated laser beam was focused by the SIL system and the gold-coated cantilever covered the focus spot area, both the propagating light wave and the evanescent light wave would be reflected back and re-collimated by the SIL lens system. A beam splitter was inserted into the optical path and the reflected beam formed a bright spot on the screen. On the other hand, when the cantilever was not covering the focus spot area, most of the propagating wave would transmit through. Only the evanescent wave was reflected, and a relatively dark spot would be formed on the screen.

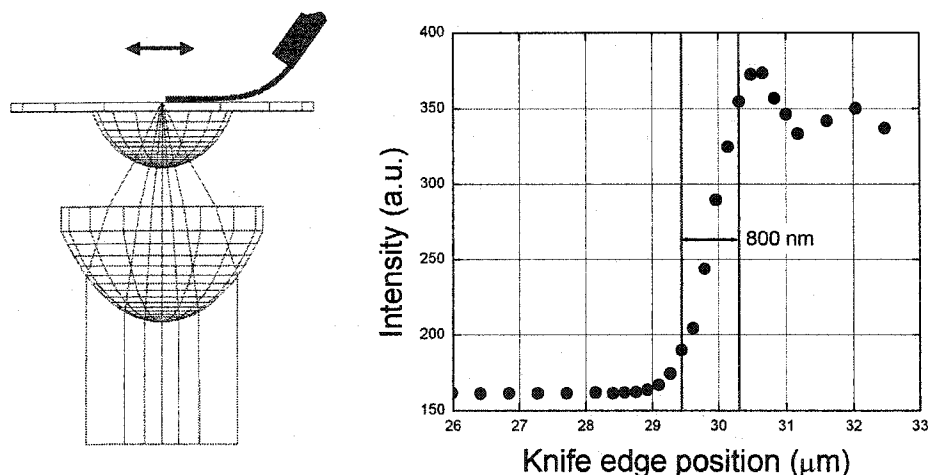


**Figure 3-24: Knife-edge test of the focused field profile**

The rear focal plane of the objective lens was set precisely at the flat surface of the hemispherical SIL lens. When the piezoelectric tube of the AFM scanned the cantilever in one dimension, the cantilever cut the laser focus spot periodically and the reflected beam formed a blinking light spot on the screen. Figure 3-24 shows a transition curve from dark to bright, which is measured while documenting the position of the cantilever. The curve reveals a transition interval of 800 nm. Taking into account the air gap

between the cantilever and the flat surface of the hemispherical SIL lens and the diffraction effect of the knife-edge, the real focus spot size of the SIL system is smaller than 800 nm. This result is in general agreement with the theoretical prediction discussed in Section 3.4.5 (~ 500 nm).

### 3.5 Raman AFM with Nanoscale Resolution

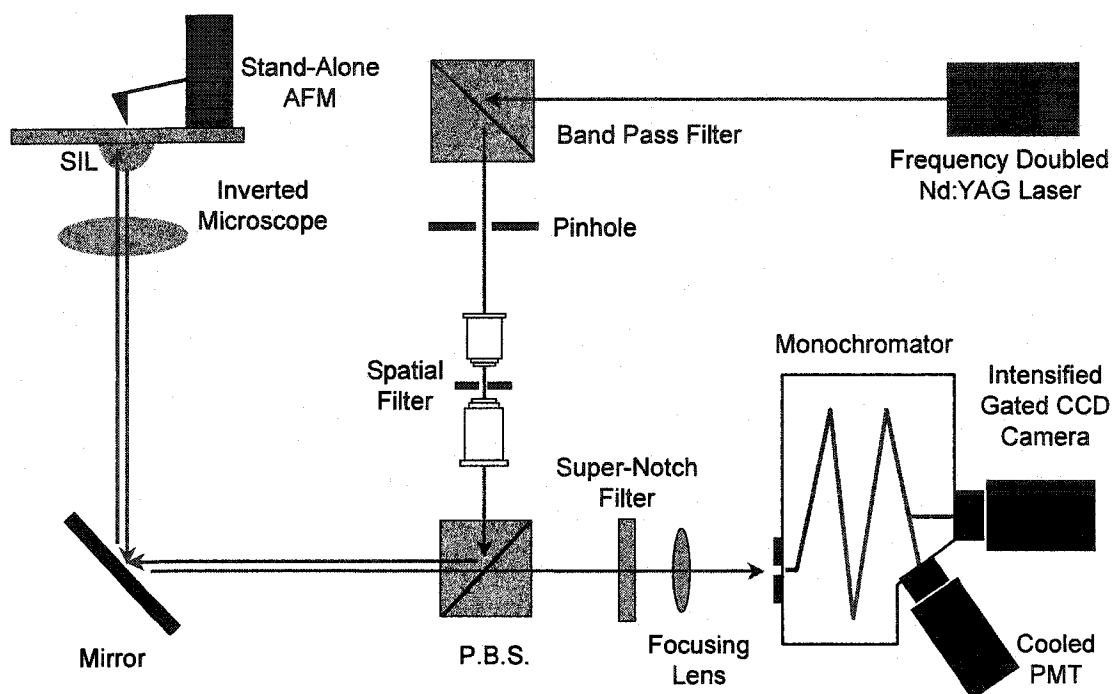


**Figure 3-25: Schematic diagram of a Raman-AFM system**

The Raman Atomic Force Microscope (RAFM) described here is the integration of a Raman spectrometer, an atomic force microscope, and an inverted optical microscopic imaging system, as illustrated in Fig. 3-25.

#### 3.5.1 Raman spectrometer

The Raman spectrometer is a home-built system that essentially consists of a laser, a band-pass filter, a sample compartment, a monochromator, a laser-line rejection filter, and two high-sensitive photon detectors. The spectrometer can be operated at either  $\lambda = 785 \text{ nm}$  or  $\lambda = 532 \text{ nm}$ .

## 1. Lasers

For operation at 532 nm, a frequency doubled CW Nd:YAG laser (GM32-50IH, INTELITE) is used as the light source for the excitation of Raman scattering. This DPSS (Diode Pumped Solid State) laser generates about 50 mW of polarized 532 nm optical power.



**Figure 3-26: Temperature control and mode stabilization stage of the laser diode**

For operation at 785 nm, the excitation light source is changed into an index guided, multi-quantum well GaAlAs laser diode (CircuLaser PS026, BLUE SKY RESEARCH). The integrated internal beam correcting optics of the laser diode provides a 50 mW circular, diverging beam ( $NA \approx 0.11$ ) with diffraction limited wavefronts whose peak-to-valley aberration is equal to or better than  $\lambda/4$ . The laser output is collimated by a laser collimator (GLC002, MELLES GRIOT) and the wavelength is stabilized by a home-built temperature controller and a mode stabilization stage, as shown in Fig. 3-26.

## 2. Bandpass filtering of the laser wavelength

Both the 785 nm diode laser and the 532 nm DPSS laser have some unwanted radiations propagating together with the laser beam, such as spontaneous emission, fluorescence and pump light. In the optical wavelength domain, these unwanted radiations have a bandwidth much broader than the laser line, and are distributed at the same region as the Raman spectrum. Although the unwanted radiations are much less intense than the laser, they could easily overwhelm the detection of the extremely weak Raman signal when collected into the spectrometer. To get rid of these radiations, a band-pass filter (HLBF @ 785 nm or 532 nm, KAISER) is used to clean the excitation wavelength, as illustrated in Fig. 3-27.

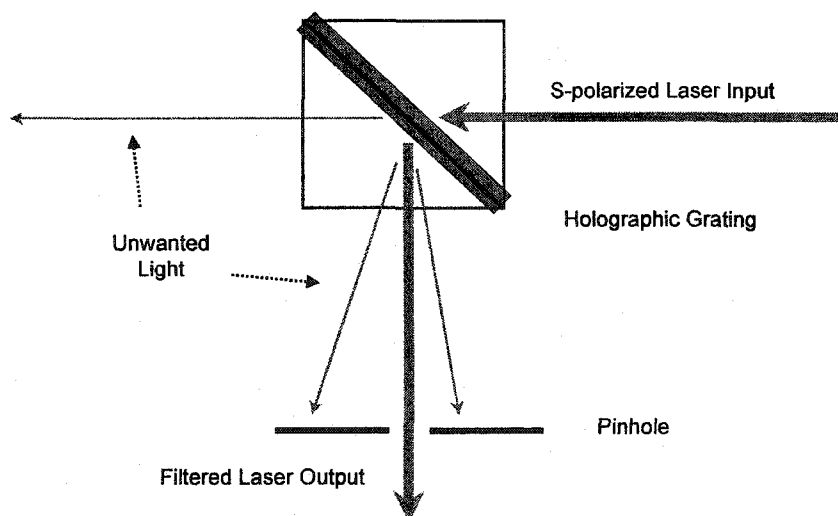


**Figure 3-27: Holographic laser bandpass filter**

The filter consists of a holographic volume transmission grating, which is mounted between two prisms to form a cube. When the s-polarized laser beam is directed perpendicularly into the entrance face of the cube, the grating diffracts the laser

wavelength through an angle of  $90^\circ$  so that the output beam is nominally perpendicular to the exit face of the cube. Most of the unwanted wavelength is not diffracted by the grating and passes through the cube. The unwanted wavelength diffracted by the grating exits at a different angle to the laser wavelength and will be blocked by a spatial filter (pinhole). The transmission of the holographic band-pass filter is greater than 90% for the laser wavelength, and the FWHM of the pass band is narrower than 2nm.

#### 4 Spatial filtering of the laser beam

The laser beam for Raman excitation is not an ideal Gaussian profile. It picks up intensity variations from scattering by defects of optical elements and particles in the air. Furthermore, the collimating and mode stabilizing optics of the diode laser, the holographic bandpass filter, and even air fluctuations introduce aberrations. All these intensity variations and wavefront aberrations contaminate the Gaussian beam with spatial noise. One can view this by expanding the 532 nm DPSS laser beam onto a screen and observing the whorls, holes and rings superimposed on the ideal pattern of uniform laser speckle.

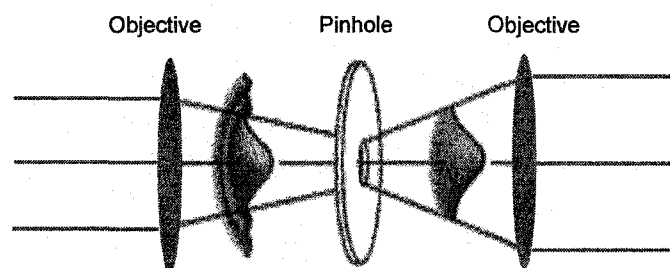


**Figure 3-28: Spatial filtering of the laser beam**

The existence of a large amount of spatial noise makes it impossible to obtain a small laser focus spot size while utilizing RAFM to probe local material information.

Therefore, the laser beam has to be spatially filtered before being focused onto the sample. Figure 3-28 shows a schematic diagram of the spatial filtering. The laser beam is focused by a microscope objective lens with  $NA = 0.2$ . On the focal plane, the ideal Gaussian beam will produce a light spot centered on the optical axis (low spatial frequency). All the spatial noise caused by the imperfections in the optical path will be focused in an annulus about the axis (high spatial frequency). A pinhole centered on the optical axis blocks the unwanted noise annulus while passing the center spot. The optimal pinhole diameter can be calculated by

$$D \sim \lambda / NA = \frac{0.532 \mu m}{0.2} \sim 3 \mu m. \quad (3.48)$$

Passing through the pinhole, the light is re-collimated by the second microscope objective with  $NA = 0.2$ . The output beam can be approximated by an ideal coherent, collimated laser beam behaving as if generated by a distant point source.

#### 4. Monochromator and detectors

After being “cleaned” in both the optical wavelength domain and the spatial frequency domain, the laser beam is sent to the sample through an optical microscopic imaging system incorporated with a SIL lens, which will focus the laser light onto the sample, and will collect and collimate the Raman scattered light. The detail of this optical imaging system will be described later in Section 3.5.2.

An  $f/3.9$  lens coupled the collimated Raman scattering light into the entrance slit (port A) of a quarter-meter monochromator (MS257<sup>TM</sup>, ORIEL INSTRUMENTS). A schematic diagram of MS257 is shown in Fig. 3-29. This monochromator is designed around an asymmetric in-plane Czerny-Turner configuration. The input light from the entrance slit



(port A) is collimated by a toroidal concave mirror and directed to a planar diffraction grating. The grating separates different wavelengths of incident light into different exit angles, and different angles of light are focused onto the different locations on the monochromator's output image plane by a second toroidal concave mirror.

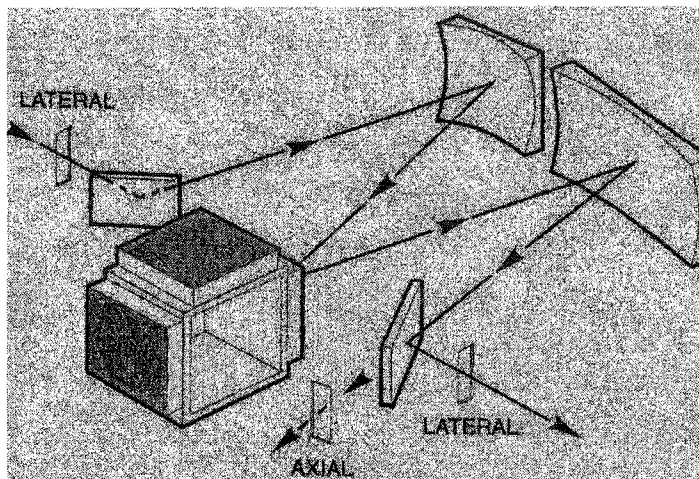


**Figure 3-29: Schematic diagram of a MS257 monochromator**

The MS257 monochromator has two output ports, port B and port C. A motorized flip mirror can regularly switch the output beam between them. At port C, an exit slit is placed on the output image plane to transmit one single wavelength to a detector. Therefore, the needed Raman spectrum can then be obtained by rotating the diffraction gratings and sequentially measuring the optical intensity of different wavelength. The detector is a PhotoMultiplier Tube (PMT, R943-02, HAMAMATSU), which is mounted in a liquid heat-exchanged thermoelectric cooling house. The PMT is sensitive enough to operate in a photon counting mode from 450 nm to 900 nm. The spectral responsivity is determined by the GaAs photocathode. After being cooled down to  $-30^{\circ}\text{C}$ , the anode dark current of PMT can be as small as ten counts per second.

Port B is connected to a gated, intensified CCD camera (PI.MAX: 1024HQ, PRINCETON INSTRUMENTS), which has 256 rows of 1024 pixels, detecting the photons simultaneously. The key part of this CCD camera is a Gen III image intensifier tube with a MicroChannel Plate (MCP). When a Raman photon is incident, a photoelectron is generated on the GaAs photocathode of the intensifier and accelerated across a gap toward the front surface of the MCP. The electron then enters one of the channels and is multiplied by successive collisions with the channel wall. When the electron-packet exits the MCP, it is pulled across another gap and strikes the phosphor screen. The kinetic energy of the electron-packet is converted by the phosphor into visible photons that are then coupled through a fiber-optic bundle to the CCD.

Since the CCD camera has the same GaAs photocathode as the PMT, its range of the spectral response is also from 450 nm to 900 nm. The electronic gain of the image intensifier can be as high as 10,000. This allows the photocurrent to be amplified over the reading noise of the CCD. Therefore, the camera can be operated at photon counting mode after being cooled down to  $-35^{\circ}\text{C}$  by a thermoelectric cooler with water circulation. A Programmable Timing Generator (PTG) could gate the camera down to 5 ns gate-width. Although not used in the RAFM measurement, the gating can provide us with temporal resolution for effective background discrimination and kinetic spectroscopy.

#### 5. Laser-line rejection filter

While measuring the Raman scattering spectrum, there always are photons at the laser frequency being collected into the monochromator. Some of these unwanted photons originate from the Rayleigh scattered laser line. Others are the laser photons reflected

from the sample surface and other surfaces of the optical elements. Note that Raman scattering is a very weak effect. Even strong Raman bands are still  $10^6$  times weaker than the intensity of Rayleigh scattering. The Raman signal from the thin film sample may be more than  $10^{10}$  times weaker than the collected light power at the laser frequency. Although the Raman instrument operates in a spectral region that does not include the laser wavelength, the stray light at the laser wavelength can still reach the detector and overwhelm the weak Raman signal.

Therefore, it is necessary to greatly attenuate the optical power at the laser wavelength, while minimally attenuating light at the Raman wavelengths of interest. To fulfill this goal, a holographic super-notch filter (HSPF @ 785 nm or 532 nm, KAISER) is inserted in front of the monochromator. The filter works at normal incidence (or a incident angle smaller than  $10^\circ$ ) with a transmission less than  $10^{-6}$  at the laser frequency, equivalent to optical density greater than 6.0. The spectral width of the filter's rejection band is only about 10 nm. Thus, the filter's impact on the Raman spectrum is negligible.

### **3.5.2 Optical microscopic imaging system**

In the RAFM system, Raman photons always come from small regions of a thin film sample. Since microscopes are designed specifically for looking at small regions of a material, an inverted optical microscope (Axiovert10, ZEISS) is employed as the sample compartment for the laboratory Raman measurements.

Figure 3-30 shows the setup of Axivert10. The s-polarized laser beam is coupled into the microscope with a Polarized Beam Splitter (PBS) and then directed into an infinity corrected high NA (0.8) 100X microscope objective (1-UM354, Olympus) by a reflecting

mirror. The objective is used in a  $180^\circ$  backscattering geometry as shown in Fig. 3-30, both to focus the excitation laser beam onto the sample, and to collect the Raman scattered light. The collected light is collimated by the objective lens and directed into the P.B.S. Since the Raman photons are approximately unpolarized, 50% of the photons will pass through the P.B.S. and be coupled into the spectrometer.

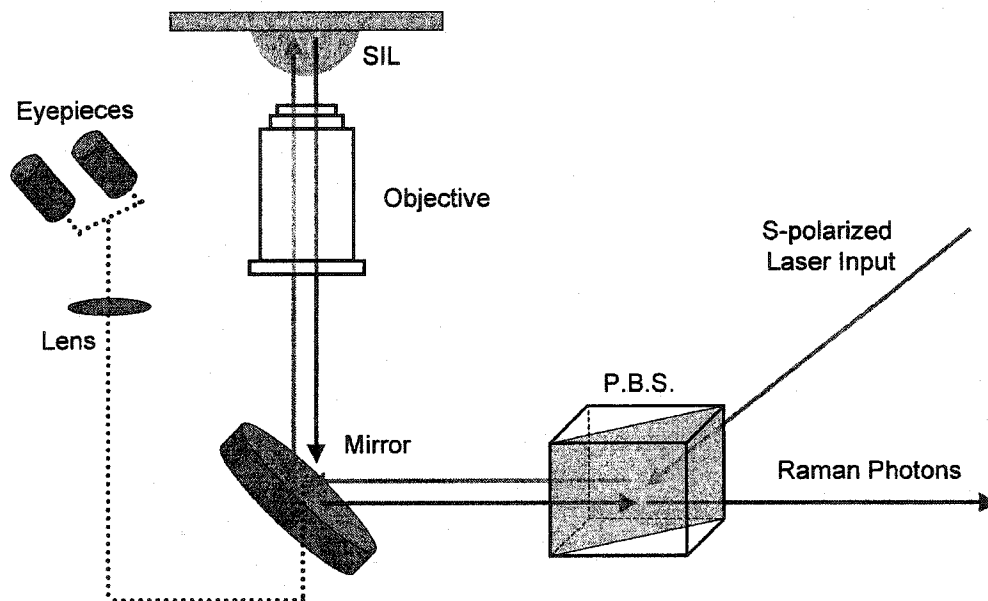


**Figure 3-30: Schematic diagram of the inverted microscope**

The objective lens has a long working distance (3.4 mm) so that it can be incorporated with a hemispherical Solid Immersion Lens (SIL), which is mounted on an  $x$ - $y$  translation stage provided by the microscope frame. The stage gives the hemispherical SIL lens two degrees of freedom relative to the microscope objective and the microscope focusing stage provides one additional degree of freedom in  $z$  dimension. Using these three degrees of freedom, SIL can be aligned so that the center of the hemispherical lens is positioned right at the focus of the microscope objective.

One of the greatest benefits a user gets by using a microscope as the Raman sample compartment is the ability to see a magnified image of the sample. The reflecting mirror inside the Axiovert10 microscope is mounted on a translation stage. It can be shifted off the optical path so that the magnified (100X10) image will be observed through the microscope eyepieces or by using a CCD imaging system. The magnified image can give us some hints about where in the sample the Raman spectrum originates. This makes alignment of the sample quick and easy. It also helps the user establish that the Raman spectrum is really coming from the material of interest, rather than from a contaminant or non-representative part of the sample.

### **3.5.3 Stand-Alone AFM with metallic probe**

The atomic force microscope used in the RAFM system is a commercial stand-alone AFM (SAAFM-1, DIGITAL INSTRUMENTS) with a Digital Instruments (Sanata Barbara Ca) Nanoscope III controller. Description of this AFM system can be found in the literature [1, 28, 79]. The AFM head is attached to the inverted optical microscope with a custom-built tripod stage. This arrangement allows AFM operation on top of the SIL lens incorporated with the microprobe objective.

The conducting tip used in the AFM was a standard silicon nitride probe sputtering coated with a 40 nm-thick silver layer. The metal granulates on the tip excite localized surface plasmons in the vicinity of the tip apex by absorbing the incident laser photons. The evanescent electromagnetic fields due to these surface plasmons gave rise to SERS of sample molecules that were in close proximity to the tip.

### 3.5.4 Experiment result

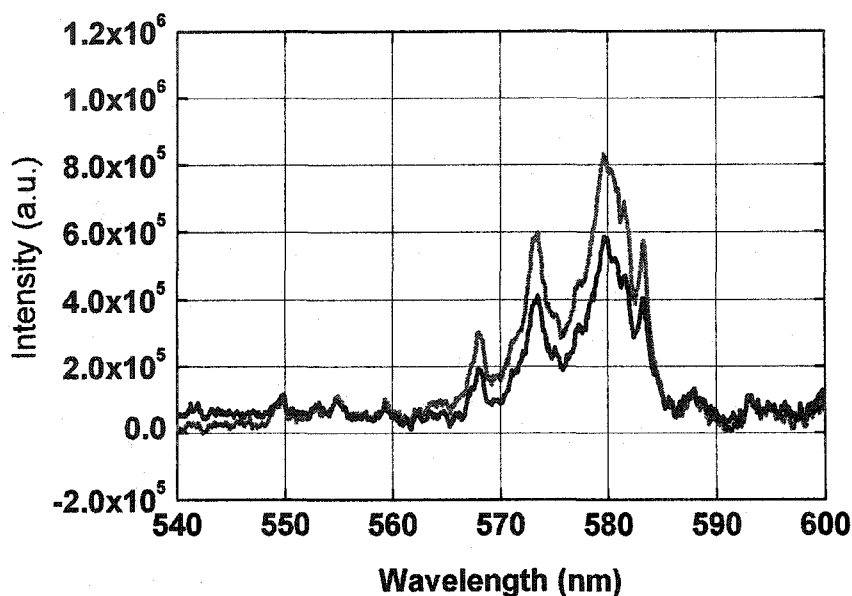


**Figure 3-31: Tip enhanced Raman scattering of Rhodamine 6G sample [56]**

Figure 3-31 shows two spectra obtained with and without the presence of the AFM tip on Rhodamine film, respectively. The sample in this experiment consisted of a 10 nm-thick Rhodamine 6G film spin coated on a glass cover slip covered with an 8 nm-thick silver film to quench the fluorescence of the Rhodamine 6G film.

The weak Raman spectrum (black line) was generated by the Rhodamine film covering the whole area of the optical spot that had a diameter of roughly 1  $\mu\text{m}$ . The strong spectrum (gray line), on the other hand, consisted of the contribution from the whole area of the optical spot plus the contribution from the tip enhanced area with an approximate diameter of 50 nm. Taking into account these two contributions, one can

find that the tip enhancement amounts to roughly five orders of magnitude. This result is in general agreement with those obtained in the literature [37, 80].

Raster scanning the tip across a sample and collecting the SERS signal could provide a 2D image of the chemical identity of the probed film simultaneous with its topography as measured by the AFM with nanometer scale resolution, but no practical scanning Raman microscopy images with a nanometer scale resolution have been achieved yet. Several limitation of the complicate instrumentation of RAFM system accounts for this:

First, it is hard to match the Raman excitation wavelength with the surface plasmon resonance of the rough metallic coating on AFM tip. This is due to the difficulty in preparing a durable and reproducible conducting AFM tip that is active for SERS effect.

Second, the collection exposure time of a Raman spectrometer is usually as long as 30 seconds for each scanning pixel. During this time interval, the conducting AFM tip may drift in a large scale and then the resolution is lost.

Third, tip-sample friction during the scanning can lead to a catastrophic failure of the metal-coated AFM probes. Only after several lines of raster scanning using a contact mode AFM, the tip apex could be worn down and the coating near the apex was peeled away.

The key to solve these problems is to find a way to prepare a rough surface with nanometer grain size on AFM tips to acquire a very large enhancement factor (such as  $10^{10}$ ). Then the exposure time could be shorter and the AFM probe would not be damaged by raster scanning on the sample surface.

## 3.6 Thermometry using Raman Spectroscopy

### 3.6.1 Introduction to Raman thermometry

Typically, the dominant signal observed in Raman spectroscopy is red shifted (known as Stokes shift) with respect to the excitation line. The intensity of this signal is related to the occupancy of the ground state, and as such is relatively independent of temperature. However, there is also a blue-shifted Raman component, known as the anti-Stokes line. The intensity of the anti-Stokes lines is directly related to the excited state occupancy of the material, which is populated according a Boltzmann distribution. From the previous discussion (see Section 3.1) of the classical physics theory of Raman scattering, the ratio between the Stokes and anti-Stokes Raman shift can be obtained, as given by the following equation

$$n = \frac{I_{Stokes}}{I_{AntiStokes}} = \frac{(\nu_0 - \nu_1)^4}{(\nu_0 + \nu_1)^4} e^{\frac{h\nu_1}{kT}} \quad (3.49)$$

Here,  $\nu_0$  is frequency of the excitation laser beam,  $\nu_1$  is the Raman shift,  $e^{\frac{h\nu_1}{kT}}$  is the Boltzmann factor, T is the temperature, and other symbols have their usual values. Taking the ratio, accounting for the energy differences, and inverting, gives a simple equation for deriving the temperature, once the number of Stokes and anti-Stokes photons are known.

$$T = \frac{h\nu_1}{k \cdot \text{Log}\left[n \cdot \frac{(\nu_0 + \nu_1)^4}{(\nu_0 - \nu_1)^4}\right]} \quad (3.50)$$



For a typical excitation at 532 nm, and a Raman shift of  $1000\text{ cm}^{-1}$ , the result is shown in the Fig. 3-32.

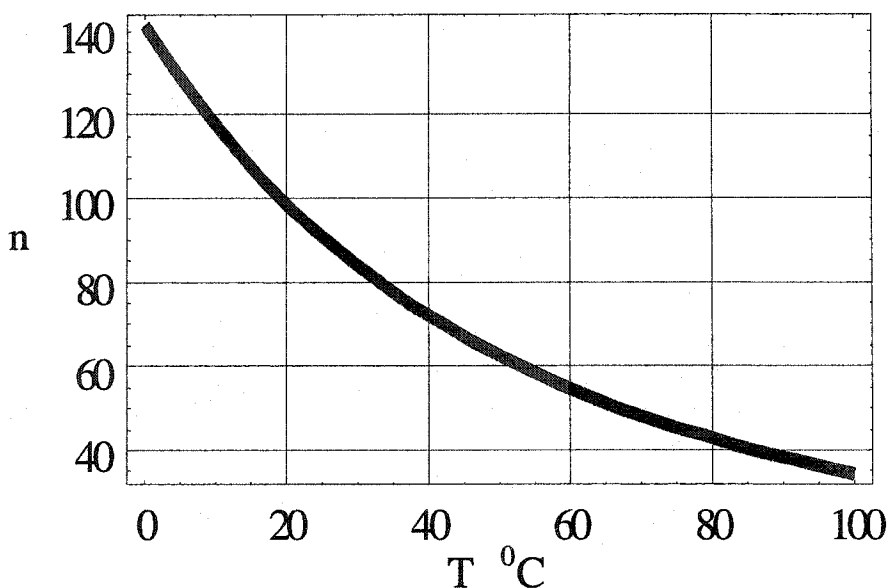


**Figure 3-32: Stokes/anti-Stokes ratio with temperature for a shift of  $1000\text{cm}^{-1}$ .**

Measuring the ratio of the Stokes and anti-Stokes intensities allows the temperature of the scattering material to be determined. There are several advantages to this technique; it is non-contact and instantaneous method of thermometry, and it can be used to obtain an absolute map of the local temperature across the sample with high spatial resolution by utilizing RAFM experimental configuration. The major obstacle in using this technique, however, is that Raman scattering is an extremely weak signal, with a very low cross-section, requiring a long signal integration time.

### 3.6.2 An example experiment of Raman thermometry

As an example, films of  $\beta$ -carotene on a HOPG substrate were examined. Both the anti-Stokes and the Stokes Raman spectrum were collected when the illuminating laser

power was 3mW, 8mW, 12mW, and 17mW. The ratios of the intensities of the Stokes to anti-Stokes spectrum were calculated for each power level, to compensate for the change in the anti-Stokes intensity due to the change in incident power.

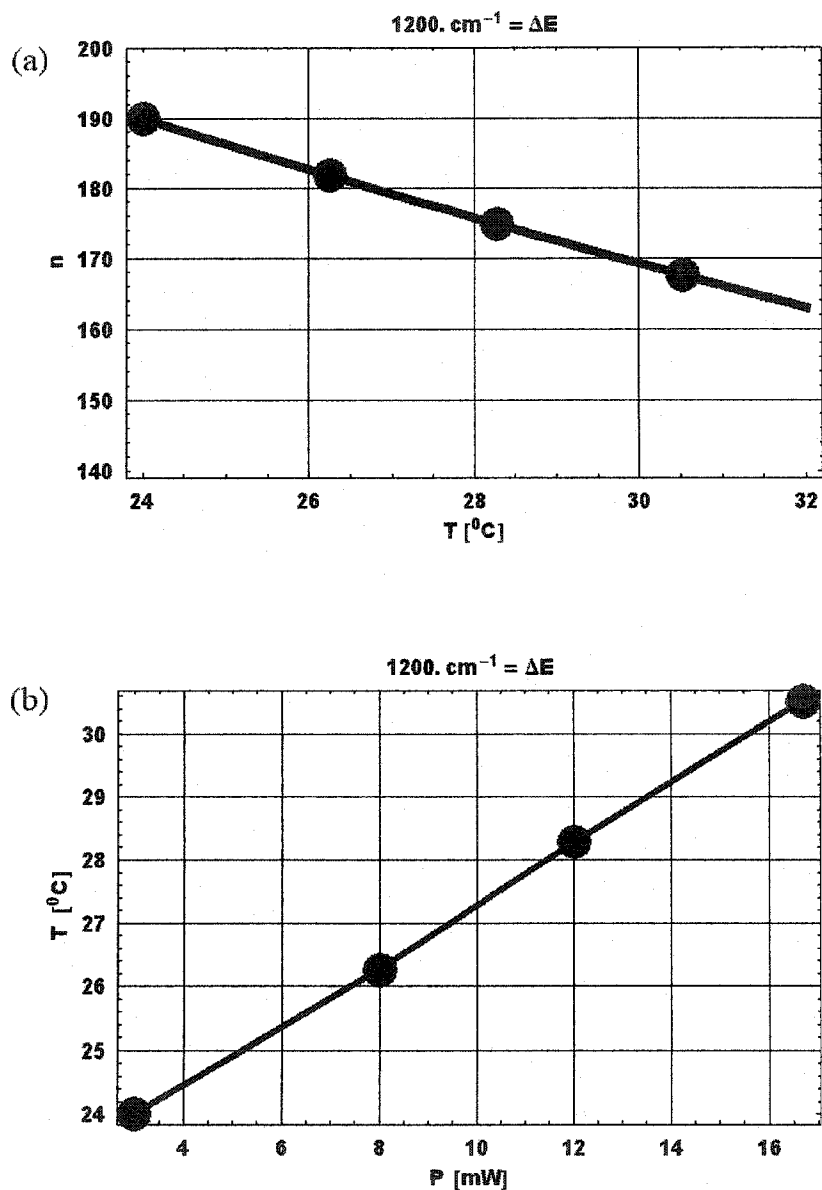


Figure 3-33: Steady state temperature measurements using Raman spectroscopy

From the previous discussion of the Raman thermometry theory, the ratio of Stokes to anti-Stokes for the  $1200 \text{ cm}^{-1}$  Raman shift of  $\beta$ -carotene can be plotted as a function of temperature. This theoretical  $n(T)$  curve is shown in Fig. 3-33 (a). The temperature of the Raman scattering material for each laser power level can then be determined by fitting the measured Stokes to anti-Stokes ratio  $n$  in the theoretical  $n(T)$  curve. Experimental results of the temperature power relation are shown in Fig. 3-33 (b), demonstrating the ability to use Raman spectroscopy as a simple and effective thermometry technique.

### 3.6.3 Theoretical analysis of the evolution of local temperature in space and time

Near-field enhanced Raman can be used for the determination of the evolution of local temperature in both space and time. Consider a laser pulse incident on a metal film [81]. It can be shown [82] that in the simple case of a wide pulse incident on a metal film the temperature as a function of depth into the metal,  $x$ , radius from the center of the pulse,  $r$ , and time,  $t$ , evolves according to the following equation [82-84],

$$T_{FF} = \frac{r_0^2}{r_0^2 + 4\kappa \cdot t} \cdot \text{Exp}\left[-\frac{r^2}{r_0^2 + 4\kappa \cdot t}\right] \times \frac{2\alpha}{\rho \cdot c \sqrt{\pi}} \left( \text{Exp}\left[\frac{t}{\tau_i}\right] \cdot \text{Erfc}\left[\sqrt{\frac{t}{\tau_i}}\right] \sum_{i=1}^{\infty} \left( \gamma^i \left( \text{Exp}\left[2i \cdot \alpha \cdot d + \frac{t}{\tau_i}\right] \cdot \text{Erfc}\left[i \sqrt{\frac{\tau_f}{t}} + \sqrt{\frac{t}{\tau_i}}\right]\right) \right. \right. \right. \quad (3.51)$$

$$\left. \left. \left. + \text{Exp}\left[-2i \cdot \alpha \cdot d + \frac{t}{\tau_i}\right] \cdot \text{Erfc}\left[-i \sqrt{\frac{\tau_f}{t}} + \sqrt{\frac{t}{\tau_i}}\right]\right) \right) \right)$$

Here  $\rho$ ,  $c$  and  $\kappa$  are the material density, specific heat and diffusivity respectively,  $\alpha$  and  $\lambda$  are its optical absorption and conductivity,  $d$  is the thickness of the material,  $r_0$  is the FWHM of the Gaussian pulse, and  $\tau_i$  and  $\tau_f$  are time constants relating to the rate of

heating and cooling, respectively. The first line of Eq. 3.51 determines the lateral diffusion of heat with time, the second and the third line determines the diffusion through the film. Hence this equation is approximate, assuming the convolving of these two components is still valid. The lateral diffusion is approximated by a Gaussian distribution that increases in width and decreases in height with time. The transverse diffusion can be thought of as a highly dissipative wave propagating through the film.

The evolution of local temperature in both space and time domain are depicted in Figs. 3-34, 3-35 and 3-36.

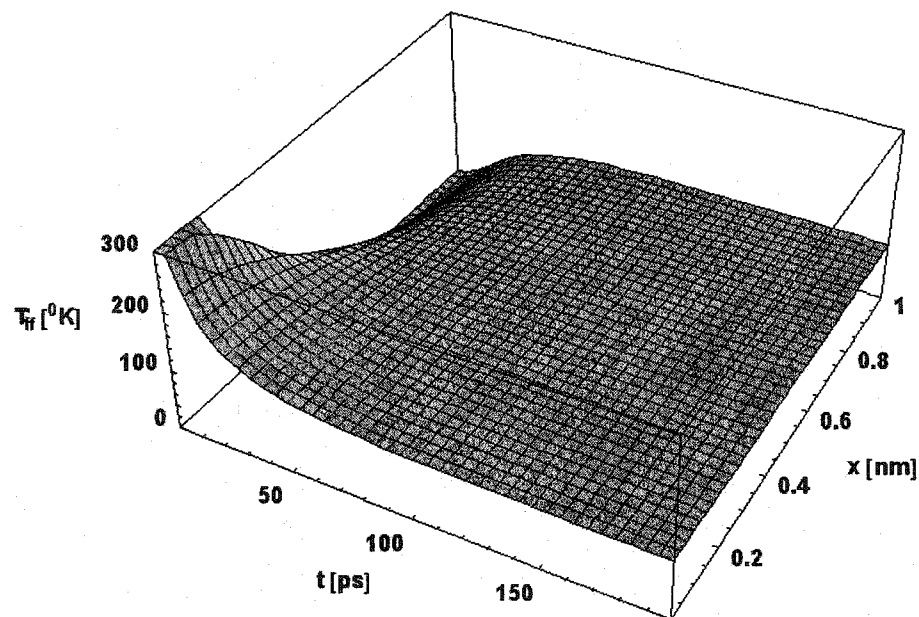


**Figure 3-34: Temperature evolution through the film as a function of time**

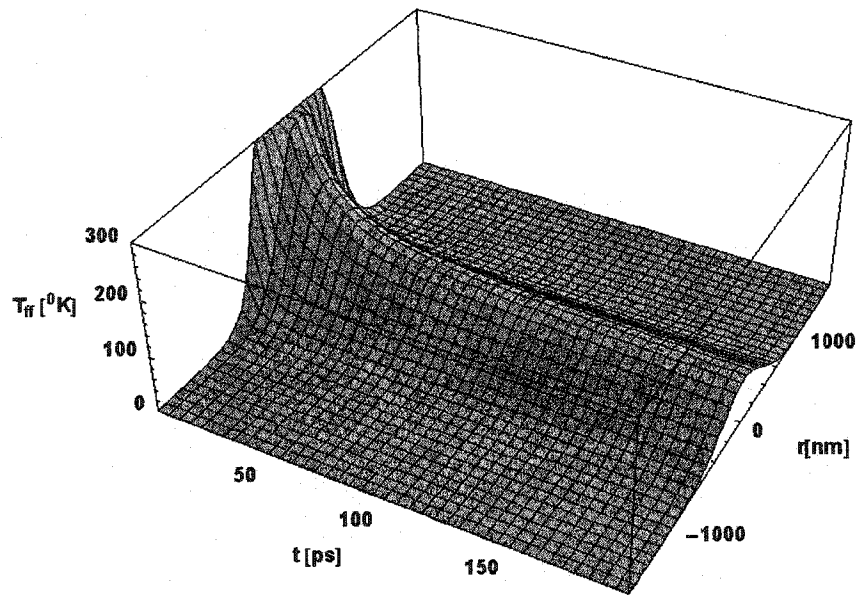


Figure 3-35: Transverse and lateral heat diffusion

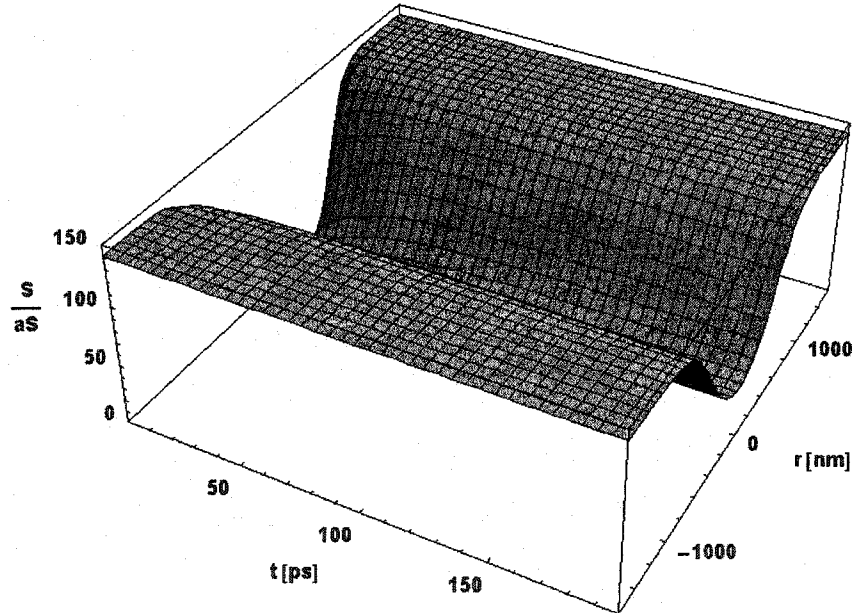


Figure 3-36: Raman Stokes/anti-Stokes ratio against time and horizontal distance

Figure 3-34 shows how the temperature distribution evolves to equilibrium through a thin metal film, where  $x$  is the normalized depth of the film. The parameters for this model use a 10 picosecond, 5 picojoule laser pulse incident on a 100 nm thick Molybdenum film. Figure 3-35 shows the normalized temperature distribution propagating transversely and laterally. The lateral diffusion substantially modifies the effects; the maximum is much less than in the previous case. Using the above equations, the Raman Stokes/anti-Stokes ratio at the surface of the film can be calculated, as in Fig. 3-36.

### 3.7 Conclusion

Raman spectroscopy has an extremely weak cross-section, but is greatly enhanced in the vicinity of noble metal films with a suitable topology. This was demonstrated for two different films, one of self-assembled gold particles, and one of a nanoscale lattice structure. This effect was additionally used to achieve sub-wavelength resolution, by fabricating an AFM tip with a similar metal film. By restricting the enhancement to the proximity of the tip, the Raman spectrum of material in this proximity can be differentiated from the Raman spectrum of the entire material within the optical spot. Thus, a sub-wavelength resolution can be achieved. But no practical scanning Raman microscopy images with a resolution better than confocal Raman microscope have been achieved yet. Several limitation of the complicate instrumentation of RAFM system accounts for this situation.

Furthermore, the potential of Raman spectroscopy to be a non-contact, absolute temperature measurement was demonstrated. By employing tip-enhanced Raman, the temperature distribution can be determined with nanoscale resolution. Further work will combine this method to achieve spatially resolved temperature mapping.

## APPENDIX

### Gaussian Beam Optics

In the direction transverse to propagation, the output beam of most lasers has an approximate Gaussian intensity profile

$$I(r) = I_0 \cdot e^{-2r^2/w^2} \quad (4.1)$$

where  $w$  is the Gaussian beam radius at which the intensity has decreased to  $1/e^2$  of its value on the axis,  $I_0$ . The Gaussian beam has different properties in comparison to classical light, particularly regarding propagation, focusing and collimation.

Note that the Fourier transform of Gaussian distribution is also a Gaussian distribution. If the Fresnel integral itself rather than the Fraunhofer approximation were to be solved, one would find that a Gaussian source distribution remains Gaussian at every point along its path of propagation through the optical system, only the Gaussian beam radius and the radius of curvature of the wavefront change.

Imagine that a Gaussian beam is somehow created with a plane wavefront at a position  $Z=0$ . The beam radius and wavefront curvature at a distance  $Z$  can be described according to

$$\begin{aligned} w(Z) &= w_0 \sqrt{1 + (Z/Z_R)^2} \\ R(Z) &= Z \left[ 1 + (Z_R/Z)^2 \right] \end{aligned} \quad (4.2)$$

where  $w_0$  is the beam radius at  $Z=0$  and  $Z_R = \pi w_0^2 / \lambda$  is the Rayleigh range. The  $Z=0$  position where Gaussian beam has a plane wavefront is called the beam waist



since  $w_0$  is the minimum radius during the propagation of Gaussian beam. For  $Z \gg Z_R$ ,  $w(Z)$  asymptotically approaches the value

$$w(Z) \approx \lambda Z / \pi w_0 \quad (4.3)$$

and the irradiance contours approach a cone of angular radius

$$\theta = \lambda / \pi w_0. \quad (4.4)$$

Therefore, when lenses are used to focus Gaussian beams, the numerical aperture is related to the radius of the beam waist by

$$NA \approx \lambda / \pi w_0. \quad (4.5)$$

The depth of focus can also be derived from the formulas above. If  $\sqrt{2} \cdot w_0$  (somewhat arbitrarily) is defined as the acceptable blur size while defocusing, then the Depth of Focus (*DOF*) of the optical system is twice the Rayleigh Range  $Z_R$  of the focused Gaussian beam.

$$DOF = 2 \cdot Z_R = \frac{2}{\pi} \cdot \frac{\lambda}{NA^2} \quad (4.6)$$

From the previous discussion, one can find that the position of the beam waist and the waist radius completely describe the Gaussian beam in the free space. When a beam passes through a lens, the Gaussian beam radius is unchanged but the wavefront curvature is changed, resulting in new values of waist position and waist radius on the output side of the interface. Therefore, one can derive laws of tracing a Gaussian beam through a lens, which is given by

$$w_{02} = \frac{f \cdot w_{01}}{\sqrt{(Z_1 - f)^2 + Z_{R1}^2}} \quad (4.7)$$

$$Z_2 = f + \frac{(Z_1 - f)f^2}{(Z_1 - f)^2 + Z_{R1}^2}$$

Here, as shown in Fig. A-1,  $w_{01}$  and  $w_{02}$  are the beam waist radii of the incident and output beam.  $Z_1$  and  $Z_2$  represent the beam waist positions relative to the lens.  $Z_{R1} = \pi w_{01}^2 / \lambda$  is the Rayleigh range of the incident beam and  $f$  is the focal length of the lens.

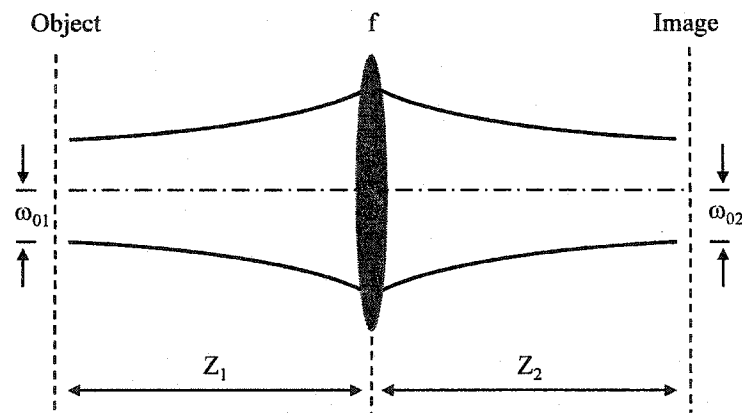


**Figure A-1: Focusing and collimation of the Gaussian beam**

Notice that when  $Z_1 \gg f$ ,  $Z_1 > Z_{R1}$  and  $Z_{R1}$  is larger than or comparable to  $f$ , the radius of the exit beam waist can be approximated to  $w_{02} \sim f \cdot w_{01} / \sqrt{Z_1^2 + Z_{R1}^2}$ , which is much smaller than  $w_{01}$  if not truncated by the lens aperture. The exit beam waist is positioned very near to the back focal point of the lens ( $Z_2 \sim f$ ). This is the situation when a lens is used to focus the Gaussian beam.

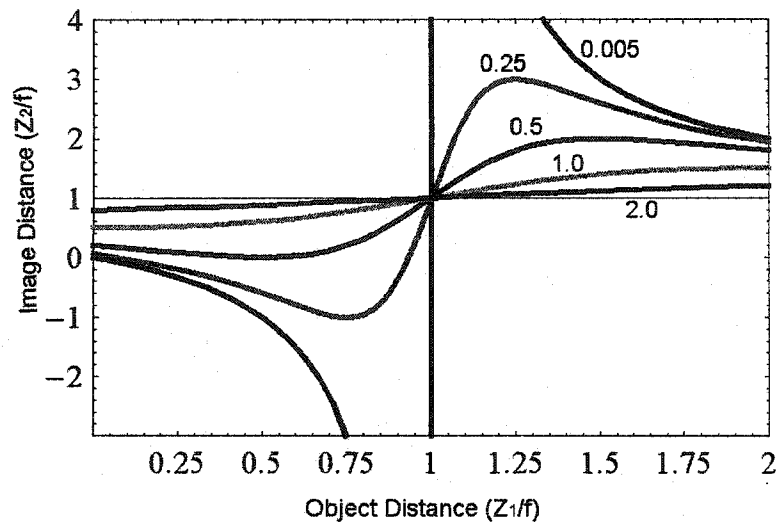


**Figure A-2: Image distance vs. object distance**

The image distance  $Z_2$  is plotted as a function of the object distance  $Z_1$  for various values of  $Z_{R1}/f$  in Fig. A-2. When  $Z_{R1} \ll f$  and the incident beam waist is positioned at the front focal plane of the lens ( $Z_1 = f$ ), the exit beam waist is at the exit pupil of the lens with a beam radius of  $w_{02} \sim w_{01} \cdot f / Z_{R1}$ , which is much larger than  $w_{01}$  if not truncated by the lens aperture. Therefore, the incident beam is essentially collimated by the lens because the exit beam has a very long Rayleigh range,  $Z_{R2} = f^2 / Z_{R1} \gg f$ . From Fig. A-2, one can also find that the output beam waist can be adjusted to any position between infinity and the aperture of the lens by moving the incident beam waist slightly out of the focal plane of the lens.

## REFERENCES

1. D. Sarid, "Exploring scanning probe microscopy with mathematica," (Wiley Interscience, 1997).
2. G. Binnig, *et al.*, "Tunneling through a controllable vacuum gap," *App. Phys. Lett.* **40**, 178 (1982).
3. G. Binnig, C.F. Quate, and C. Gerber, "Atomic force microscope," *Phys. Rev. Lett.* **56**, 930 (1986).
4. H.J. Mamin, *et al.*, "High-density data storage using proximal probe techniques," *IBM Journal of Research and Development* **39**, 681 (1995).
5. A. Born and R. Wiesendanger, "Present and future developments of SPM systems as mass storage devices," *App. Phys. A* **68**, 131 (1999).
6. J.G. Goodberlet, "A very-high-density scintillation-data-storage device," *Microelectronic Engineering* **46**, 145 (1999).
7. P. Vettiger, *et al.*, "Ultrahigh-density, high-data-rate NEMS-based AFM data storage system," *Microelectronic Engineering* **46**, 11 (1999).
8. H.J. Gao, *et al.*, "Reversible, nanometer-scale conductance transitions in an organic complex," *Phys. Rev. Lett.* **84**, 1780 (2000).
9. D.X. Shi, *et al.*, "Direct observation of a local structural transition for molecular recording with scanning tunneling microscopy," *App. Phys. Lett.* **77**, 3203 (2000).
10. Y. Zhao, *et al.*, "Comments on reversible, nanometer-scale transitions in an organic complex," *Phys. Rev. Lett.* **87**, 1797 (2001).
11. Q. Zhong, *et al.*, "Fractured polymer/silica fiber surface studied by tapping mode atomic force microscopy," *Surf. Sci. Lett.* **290**, L688 (1993).
12. M. Stark, *et al.*, "Spectroscopy of anharmonic cantilever oscillations in tapping-mode atomic-force microscopy," *Appl. Phys. Lett.* **77**, 3293 (2000).
13. S.H. Strogatz, "Nonlinear dynamics and chaos," (Addison Wesley, New York, 1994).
14. J. Chen, *et al.*, "Numerical simulations of a scanning force microscope with a large-amplitude vibrating cantilever," *Nanotechnol.* **5**, 199 (1994).

15. S.C. Minne, *et al.*, "Automated parallel high-speed atomic-force microscopy," *Appl. Phys. Lett.* **72**, 2340 (1998).
16. R.C. Thomas, *et al.*, "The mechanical response of gold substrates passivated with self-assembling monolayer films," *Science* **259**, 1883 (1993).
17. J.P. Cleveland, *et al.*, "Energy dissipation in tapping-mode atomic force microscopy," *Appl. Phys. Lett.* **72**, 2613 (1998).
18. J.P. Hunt and D. Sarid, "Kinetics of lossy grazing impact oscillators," *Appl. Phys. Lett.* **72**, 2969 (1998).
19. D. Saluel, *et al.*, "Ultra high density data storage on phase change materials with electrical micro-tips," *J. Mag. and Mag. Mater.* **193**, 488 (1999).
20. E.B. Myers, *et al.*, "Current-induced switching of domains in magnetic multilayer devices," *Science* **285**, 867 (1999).
21. A. Bietsch, *et al.*, "Electrical testing of gold nanostructures by conducting atomic force microscopy," *J. Vac. Sci. Technol. B* **18**, 1160 (2000).
22. D. Sarid, "Tapping-mode scanning force microscopy: Metallic tips and samples," *Comp. Mat. Sci.* **5**, 291 (1996).
23. R. Garcia, M. Calleja, and F. Perez-Murano, "Local oxidation of silicon by dynamic force microscopy: Nanofabrication and water bridge formation," *Appl. Phys. Lett.* **72**, 2295 (1998).
24. R. Garcia, M. Calleja, and H. Rohrer, "Patterning of silicon surfaces with non contact atomic force microscopy: Field induced formation of nanometer-size water bridges," *J. Appl. Phys.* **86**, 1898 (1999).
25. H. Dai, N. Franklin, and J. Han, "Carbon nanotube tips for AFM nanolithography," *Appl. Phys. Lett.* **73**, 1508 (1998).
26. E.S. Snow and P.M. Campbell, "AFM fabrication of sub-10 nm metal-oxide devices with in situ control of electrical properties," *Science* **270**, 1639 (1995).
27. A. Fein, *et al.*, "Individually injected current pulses with conducting-tip, tapping-mode atomic force microscopy," *Appl. Phys. Lett.* **79**, 3935 (2001).
28. "Multimode nanoscope IIIA instruction manual," (Digital Instruments, Santa Barbara, Ca., 2000).

29. C.A. Peterson, *et al.*, "V-shaped metallic-wire cantilevers for combined atomic force microscopy and Fowler-Nordheim imaging," *Nanotechnol.* **9**, 331 (1999).
30. R.E. Thomson and J. Moreland, *J. Vac. Sci. Technol. B* **13**, 1123 (1995).
31. T. Sulchek, *et al.*, "High-speed tapping mode imaging with active Q control for atomic force microscopy," *Appl. Phys. Lett.* **76**, 1473 (2000).
32. I.R. Lewis and H.G.M. Edwards, "Handbook of Raman spectroscopy: From the research laboratory to the process line," (Marcel Dekker, 2001).
33. A.T. Tu, "Raman spectroscopy in biology: Principles and applications," (John Wiley & Sons, 1982).
34. M.J. Pelletier, "Analytical applications of Raman spectroscopy," (Black Science, 1999).
35. E.J. Ayars and H.D. Hallen, "Surface enhancement in near-field Raman spectroscopy," *Appl. Phys. Lett.* **76**, 3911 (2000).
36. L. Maya, C.E. Vallet, and Y.H. Lee, "Sputtered gold films for surface-enhanced Raman scattering," *J. Vac. Sci. Technol. A* **15** (1997).
37. M.S. Anderson, "Locally enhanced Raman spectroscopy with an atomic force microscope," *Appl. Phys. Lett.* **76**, 3130 (2000).
38. K. Kneipp, *et al.*, "Surface-enhanced Raman scattering and biophysics," *J. Phys.: Condens. Matter* **14**, R597 (2002).
39. N. Hayazawa, *et al.*, "Metallized tip amplification of near-field Raman scattering," *Optics Communications* **183**, 333 (2000).
40. S. Nie and S.R. Emory, "Probing single molecules and single nanoparticles by surface-enhanced Raman scattering," *Science* **275**, 1102 (1997).
41. H.W. Lo, "Raman measurements of lattice temperature in Silicon under intense pulsed laser excitation," (Department of Physics, Kansas State University, 1982).
42. T.R. Hart, R.L. Aggarwal, and B. Lax, "Temperature dependence of Raman scattering in Silicon," *Phys. Rev. B* **1**, 638 (1970).
43. M. Fleischmann, P.J. Hendra, and A.J. McQuillan, *Chem. Phys. Lett.* **26** (1974).

44. M.G. Albrecht and J.A. Creighton, "Anomolously intense Raman spectra of pyridine at a silver electrode," *J. Am. Chem. Soc.* **99**, 5215 (1977).
45. D.L. Jeanmaire and R.P.V. Duyne, "Surface Raman spectroscoelectrochemistry, Heterocyclic, aromatic, and aliphatic amines adsorbed to anodized silver electrodes," *J. Electroanal. Chem.* **84**, 1 (1977).
46. K. Kneipp, *et al.*, "Extremely large enhancement factors in surface-enhanced Raman scattering for molecules on colloidal gold clusters," *Appl. Spectr.* **52**, 1493 (1998).
47. S.J. Oldenberg, *et al.*, "Surface enhanced Raman spectroscopy in the near infrared using metal nanoshell substrates," *J. Chem. Phys.* **111**, 4729 (1999).
48. K. Kneipp, *et al.*, "Single molecule detection using surface-enhanced Raman scattering (SERS)," *Phys. Rev. Lett.* **78**, 1667 (1997).
49. K. Kneipp, *et al.*, "Ultrasensitive chemical analysis by Raman spectroscopy," *Chem. Rev.* **99**, 2957 (1999).
50. A. Campion and P. Kambhampati, "Surface-enhanced Raman scattering," *Chemical Society Reviews* **27**, 241 (1998).
51. N. Felidj, *et al.*, "Optimized surface enhanced Raman spectroscopy on gold nanoparticle arrays," *Appl. Phys. Lett.* **82**, 3095 (2003).
52. D. Sarid, "Long-range surface-plasma waves on very thin metal films," *Phys. Rev. Lett.* **47**, 1927 (1981).
53. W.L. Barnes, A. Dereux, and T.W. Ebbesen, "Surface plasmon subwavelength optics," *Nature* **424**, 824 (2003).
54. H.A. Bethe, "Theory of diffraction by small holes," *Phys. Rev.* **66**, 163 (1944).
55. C.J. Bowkamp, "On Bethe's theory of diffraction by small holes," *Philips Res. Rep.* **5**, 321 (1950).
56. Y. Zhao, *et al.*, "Emerging applications of nano-Raman," *Proceedings of SPIE* **5363** (2004).
57. C.L. Haynes, A.J. Haes, and R.P.V. Duyne, "Nanosphere lithography: Synthesis and application of nanoparticles with inherently anisotropic structures and surface chemistry," in *Materials Research Society Fall Meeting*, (2000), Boston, MA.

58. S. Coyle, *et al.*, "Confined plasmons in metallic nanocavities," *Phys. Rev. Lett.* **87**, 176801 (2001).
59. T. Zhu, *et al.*, "Assembling colloidal gold nanoparticles with functionalized self-assembled monolayers," *Thin Solid Films* **327**, 595 (1998).
60. B. Knoll and F. Keilmann, "Near-field probing of vibrational absorption for chemical microscopy," *Nature* **399**, 134 (1999).
61. W.E. Moerner and M. Orritt, "Illuminating single molecules in condensed matter," *Science* **283**, 1670 (1997).
62. B.C. Stipe, M.A. Rezaei, and W. Ho, "Single-molecule vibrational spectroscopy and microscopy," *Science* **280**, 1732 (1999).
63. F. Zenhausern, Y. Martin, and H.K. Wickramasinghe, "Scanning interferometric apertureless microscopy-optical imaging at 10 Angstrom resolution," *Science* **269**, 1083 (1995).
64. E. Betzig and R.J. Chichester, "Single molecules observed by near-field scanning optical microscopy," *Science* **262**, 1422 (1993).
65. X.S. Xie and R.C. Dunn, "Probing single molecule dynamics," *Science* **265**, 361 (1994).
66. W.P. Ambrose, *et al.*, "Alterations of single molecule fluorescence lifetimes in near-field optical microscopy," *Science* **265**, 364 (1994).
67. M.S. Anderson, "Infrared spectroscopy with an atomic force microscope," *Appl. Spectr.* **54**, 349 (2000).
68. M.S. Anderson and W.T. Pike, "A Raman-atomic force microscope for apertureless-near-field spectroscopy and optical trapping," *Rev. Sci. Inst.* **73**, 1198 (2002).
69. K. Dickmann, J. Jersch, and F. Demming, "Focusing of laser radiation in the near-field of a tip (FOLANT) for applications in nanostructuring," *Surface and Interface Analysis* **25**, 500 (1997).
70. F. Demming, *et al.*, "Calculation of the field enhancement on laser-illuminated scanning probe tips by the boundary element method," *Appl. Phys. B* **66**, 593 (1998).
71. W.J. Smith, "Modern optical engineering, 3rd edition," (McGraw-Hill, 2000).



72. J. Gaskill, "Linear systems, Fourier transforms, and optics," (Wiley, New York, 1978).
73. "Gaussian beam optics," (Newport Online Tutorial, 2004).
74. S.M. Mansfield and G.S. Kino, "Solid immersion microscope," *App. Phys. Lett.* **57**, 2615 (1990).
75. B. Richards and E. Wolf, "Electromagnetic diffraction in optical systems II: Structure of the image field in an aplanatic system," *Proc. R. Soc. London Se. A* **253**, 358 (1959).
76. F. Guo, T.E. Schlesinger, and D.D. Stancil, "Optical field study of near-field optical recording with solid immersion lens," *Appl. Optics* **39**, 324 (2000).
77. G.S. Kino, "Fields associated with the solid immersion lens," *Proc. SPIE* **3467**, 128 (1998).
78. D. Malacara, "Optical shop testing," (John Wiley & Sons, 1992).
79. V.B. Elings, J.A. Gurley, and D. Sarid, "Improved compact scanning force microscope," United States Patent 5,189,906 (1993).
80. R.M. Stockle, *et al.*, "Nanoscale chemical analysis by tip-enhanced Raman spectroscopy," *Chem. Phys. Lett.* **318**, 131 (2000).
81. D.Y. Tzou, "Macro to microscale heat transfer; the lagging behavior," (Taylor & Francis, 1997).
82. N. Taketoshi, T. Baba, and A. Ono, "Development of a thermal diffusivity measurement system for metal thin films using a picosecond thermoreflectance technique," *Measurement Science and Technology* **12**, 2064 (2001).
83. N. Taketoshi, T. Baba, and A. Ono, "Thermal diffusivity measurement of a thin metal film with a picosecond thermoreflectance technique," *High Temperature High Pressure* **34**, 19 (2002).
84. W.S. Capinski, *et al.*, "Thermal conductivity of GaAs/AlAs superlattices using a picosecond optical pump-probe technique," *Phys. Rev. B* **59**, 8105 (1999).